Immuno Magnetic Thermosensitive Liposomes For Cancer Therapy

Dissertation

zur

Erlangung des Doktorgrades

Der Naturwissenschaften

(Dr. rer. nat.)

dem

Fachbereich Pharmazie der

Philipps-Universität Marburg

vorgelegt von

Mohamad Alawak

aus **Deirazzor, Syrien**

Marburg/Lahn **Jahr 2019**

Erstgutachter:	**Prof. Dr. Udo Bakowsky**
Zweitgutachter:	**Prof. Dr. Frank Runkel**
Eingereicht am	**22.11.2019**
Tag der mündlichen Prüfung am	**21.01.2020**
Hochschulkennziffer:	1180

Immuno Magnetic Thermosensitive Liposomes For Cancer Therapy

Thesis

Submitted in the fulfillment of the requirements of degree of

Doctor of Natural Sciences (Dr.rer.nat.)

equivalent to

Doctor of Philosophy (Ph.D.)

To

The Faculty of Pharmacy

University of Marburg

by

Mohamad Alawak

from **Deirazzor, Syria**

Marburg/Lahn **Jahr 2019**

First supervisor: **Prof. Dr. Udo.Bakowsky**

Second supervisor: **Prof. Dr. Frank Runkel**

Date of submission: **22.11.2019**

Defense date: **21.01.2020**

Hochschulkennziffer: 1180

E I D E S S T A T T L I C H E E R K L Ä R U N G

Ich versichere, dass ich meine Dissertation

„Immuno Magnetic Thermosensitive Liposomes For Cancer Therapy“

selbständig ohne unerlaubte Hilfe angefertigt und mich dabei keiner anderen als der von mir ausdrücklich bezeichneten Quellen bedient habe. Alle vollständig oder sinngemäß übernommenen Zitate sind als solche gekennzeichnet.

Die Dissertation wurde in der jetzigen oder einer ähnlichen Form noch bei keiner anderen Hochschule eingereicht und hat noch keinen sonstigen Prüfungszwecken gedient.

Marburg, den 22.11.2019

.....

Mohamad Alawak

A U T H O R'S D E C L A R A T I O N

I declare that this thesis titled

"Immuno Magnetic Thermosensitive Liposomes For Cancer Therapy"

has been written entirely by myself and is a record of work performed by myself.

The research was carried out under the supervision of Professor. Dr. Udo Bakowsky

The dissertation has not yet been submitted to any other university in the current or any similar form and has not yet served any other purpose

Marburg, 22.11.2019

.....

Mohamad Alawak

Die vorliegende Arbeit entstand auf Anregung und unter Leitung von

Herrn Prof. Dr. Udo Bakowsky

am Institut für Pharmazeutische Technologie und Biopharmazie

der Philipps-Universität Marburg

A C K N O W L E D G E M E N T S

First of all, I would like to thank my supervisor Prof. Dr. Udo Bakowsky for his support during my Ph.D research work, who has provided ideas, advice, knowledge and motivation.

I would also like to thank my group leader Dr. Jana Brüßler for keeping her office open for me whenever I needed help, for providing scientific discussions and guidance during my research work.

I would like to acknowledge the help of Mrs. Eva Maria Mohr for her motivations and support throughout my research work. Special thanks to Julia Michaelis for her patience and help.
I would like to thank Dr. Irina Levacheva, Dr. Gihan Mahmoud, Dr. Jens Schäfer, Dr. Shashank Reddy Pinnapireddy, and Dr. Jarmila Jedelská for their support.

Sincere thanks to my past and present colleagues at the research group Bakowsky especially Alice Abu Dayyih, Dr. Konrad Engelhardt, Dr. Muhammad Yasir Ali, Dr. Imran Tariq, Muhammad Umair Amin, Sajid Ali, Dr. Lili Duse, Tan Shi, Nathalie Goergen, Jennifer Lehmann, Jan Schulze, Hirva Shah, Hendrik Vögeling, Dr. Michael Agel, Michael Raschpichler, Eduard Preis, Dr. Nikola Plenagel, Boris Strehlow and Dr. Eric Sasko.

I would also like to thank Prof. Dr. Cornelia M. Keck and her research group.

I would like to sincerely thank my ultimate supporters, my parents and siblings. They have always provided me with their ever-present support. Heartfelt appreciation for my nephews and nieces, for their endless love.

Table of contents

List of figures

List of tables

List of abbreviations

ADAMs	A disintegrin and metalloproteinase family
AFM	Atomic force microscopy
AMF	Alternating magnetic field
AMPK	AMP-activated protein kinase
aPTT	Activated partial thromboplastin time
B_0	Static magnetic field
CAM	Chorioallantoic membrane
Chelator	2-[2-[2-[bis(carboxymethyl)amino]ethyl-[2-(dioctadecylamino)-2-oxoethyl]amino]ethyl-(carboxymethyl)amino] acetic acid
Chol	Cholesterol
CLSM	Confocal laser scanning microscope
CME	Clathrin-mediated endocytosis
DAPI	4',6-diamidino-2-phenylindole
DDS	Drug delivery system
DLS	Dynamic light scattering
DMEM	Dulbecco's modified eagle medium
DMSO	Dimethylsulphoxide
DOX	Doxorubicin
DPPC	1,2-dipalmitoyl-sn-glycero-3-phosphocholine
DSC	Differential scanning calorimetry
DSPC	1,2-distearoyl-sn-glycero-3-phosphocholine
DSPE-mPEG-2000	1,2- distearoyl-sn-glycerol-3-phosphoethanolamine-N-[methoxy (polyethylene glycol)- 2000] (ammonium salt)
DTPA	Diethylenetriaminepentaacetic acid
DW-MRI	Diffusion-weighted magnetic resonance imaging
EE	Encapsulation efficiency
EGFR	Epidermal growth factor receptor
EPR	Enhanced permeability and retention effect
ER	Estrogen
FDA	Food and drug administration
Gd	Gadolinium

GI	Gastrointestinal tract
HEPES	4-(2-hydroxyethyl)-1-piperazineethanesulfonicacid
HER-2	Human epidermal growth factor receptor
HIFU	High intensity focused ultrasound
IR	Infrared
LD	Lethal dose
LDV	Laser Doppler velocimetry
Lip_{TS}	Thermosensitive liposomes
$Lip_{TS\text{-}GD}$	Magnetic thermosensitive liposomes
$Lip_{TS\text{-}GD\text{-}CY}$	Magnetic thermosensitive liposomes with cyanur
$Lip_{TS\text{-}GD\text{-}CY\text{-}MA}$	Immuno magnetic thermosensitive liposomes with cyanur
LUVs	Large unilamellar vesicles
MAbs	Monoclonal antibodies
MDA-MB-231- rna	Epithelial human breast cancer (ADAM8 knockdown) cell line
MDA-MB-231-ctrl	Epithelial human breast cancer (positive ADAM8 overexpression) cell line
MDR	Multi-drug resistance
MLVs	Multilamellar vesicles
MRI	Magnetic resonance imaging
MTT	3-(4,5-dimethylthiazol-2-yl)-2,5-diphenyltetrazolium bromide
MWCO	Molecular weight cut-off
NBD-PE	1,2-dipalmitoyl-sn-glycero-3-phosphoethanolamine-N-(7-nitro-2-1,3-benzoxadiazol-4-yl) (ammonium salt)
NMR	Nuclear magnetic resonance
NSF	Nephrogenic systemic fibrosis
PAI	Pharmaceutically active ingredients
PBS	Phosphate buffered saline
PDI	Polydispersity index
PEG	Polyethyleneglycol
PET	Positron emission tomography
R1	Longitudinal relaxation rate
r1	Longitudinal relaxivity

R2	Transverse relaxation rate
r2	Transverse relaxivity
RF	Radiofrequency
ROS	Reactive oxygen species
SD	Standard deviation
SEC	Size exclusion chromatography
SUVs	Small unilamellar vesicles
T	Temperature
T	Tesla
T1	Longitudinal relaxation time
T2	Transvers relaxation time
TEM	Transmission electron microscope
T_m	Phase transition temperature
TNBC	Triple-negative breast cancer
UHF	Ultra high magnetic field
UHF-MRI	Ultra high field magnetic resonance imaging
ΔG	Gibbs free energy equation
ΔH	Enthalpy change
ΔS	Entropy change

1. Introduction

1.1. Triple-Negative Breast Cancer

Cancer is an umbrella term for a wide range of diseases, which results from abnormal growth and division of the cells. In cancer: cells divide uncontrollably, can be invasive and metastasize into adjoining or distant organs [1]. Cancer is the second leading cause of death worldwide [2]. Cancer epidemiology varies between sexes and ages. Men are more likely to encounter lung, colon, urinary, and obviously prostate cancer. Whereas women are more likely to encounter thyroid, breast and lung cancer [3].

Breast cancer is the most frequent cancer among women, 2.1 million women are impacted each year, and also causes the highest number of cancer-related deaths among women [4]. Breast cancer is divided into different sub-groups according to the genes that are expressed by the specific cancer cells. The subgroups mainly reflect estrogen (ER) and ER regulatory genes expressed by the normal luminal epithelial cells. They can either be human epidermal growth factor receptor 2 (HER-2) positive, which displays ErbB2 / HER-2 expression and amplification or basal that display ER, Progesterone and HER-2 negative expression. Basal breast cancers are known to be more aggressive and highly invasive [5].

One of the major basal-like breast cancer is triple-negative breast cancer (TNBC), which is defined by the lack of expression of estrogen, progesterone and HER-2 receptors. TNBC represents a percentage of 10 -15 % of all diagnosed breast cancer patients [6].

The main concern regarding TNBC aggressiveness is its high capability of metastasis. The development and progression of the metastasis in TNBC is quite a complex and poorly understood process, which includes multiple steps; angiogenesis, genetic and epigenetic alterations, tumor-stroma interactions, the cells ability to survive in circulation, the extravasation into distant organs, e.g. lungs, bones, and brain, and finally the intravasation through the basement membrane [7].

Patients diagnosed with TNBC have a relatively poor prognosis and outcomes because they cannot be treated with conventional therapies targeted to HER-2 or endocrine therapies. As a consequent, this type of cancer requires special and innovative treatment approaches. Moreover, the overexpression of EGFR protein in TNBC usually increases its resistance to conventional therapies [8].

1.2. Doxorubicin for cancer therapy

The frontline drug doxorubicin (DOX) has been available in the market for treating cancer for over 30 years. While providing a wide cure range in multiple cases, DOX causes toxicity to most major organs, importantly the life-threatening cardiotoxicity [9]. Cardiotoxicity forces the treatment with DOX to be dose limited.

DOX belongs to nonselective class I anthracycline antibiotics, which is derived from the actinobacteria *Streptomyces peucetius var. caesius* [10]. DOX, a hydroxylated daunorubicin derivative, is available in the market under the name adriamycin, possessing sugar and aglyconic groups (Figure 1).

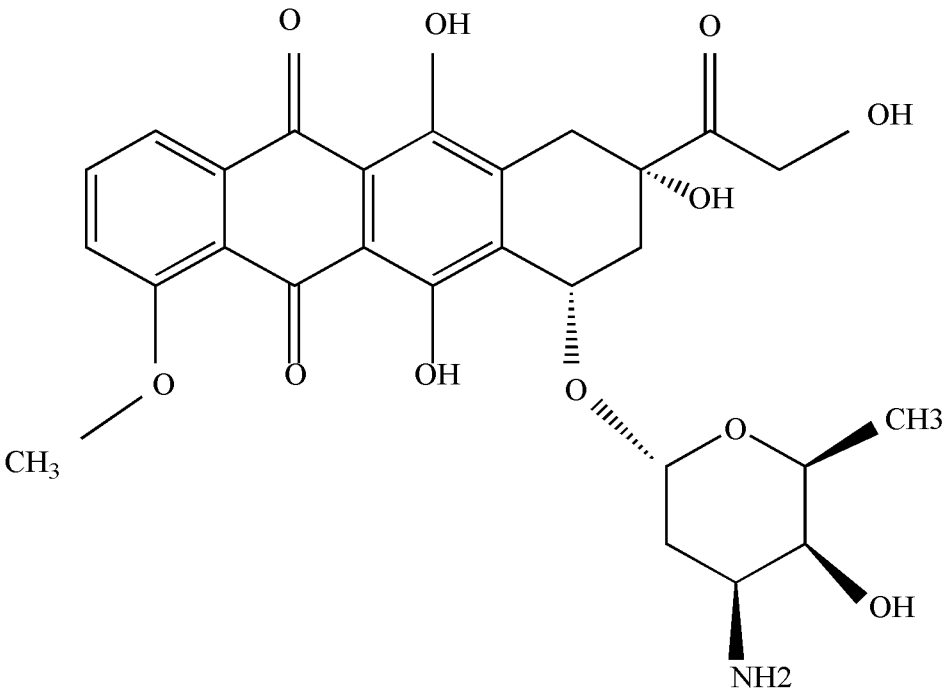

Figure 1*: Chemical structure of Doxorubicin (DOX), DOX is a nonselective anthracycline. DOX is composed of two main parts aglycone part and a sugar part also known as daunosamine, and it is attached to the glycone part by a glycosidic bond* [11].

The ability of DOX to combat rapidly dividing cells and slow cancer progression has provided it as one of the most potent Food and Drug Administration (FDA) approved chemotherapeutic agents [12]. DOX binds to DNA-associated enzymes, targets several molecular targets for cytotoxicity, disrupts the topoisomerase-II-mediated DNA repair and can as well intercalate with DNA base pairs [11]. DOX exacerbates the apoptosis pathway by activation of several

molecular signals from AMPK (AMP-activated protein kinase) to enhancing the Bcl-2/Bax apoptosis pathway [13]. DOX does not selectively affect cancerous tissues, it induces apoptosis in various healthy tissues (lung, liver, brain, kidneys, and heart). Therefore, many studies have been conducted over the years to incorporate DOX into various drug delivery systems (DDS) including liposomes, nanoparticles and hydrogels.

Apoptosis occurs when DOX enters the cell through diffusion as in its free form, or other endocytotic pathways in its nanoscale carriers form. Firstly, DOX binds to the cytoplasm´s proteasome afterward DOX-proteasome complex is formed and translocated through the nuclear pore into the nucleus. DOX has a higher affinity towards nuclear DNA than to the proteasome, therefore, it dissociates from the proteasome to bind to nuclear DNA [11]. Additionally, DOX generates free radicals causing further DNA damage, DNA separation and increasing alkylation and inhibition of macromolecules production [14]. Furthermore, DOX can bind to plasma proteins causing enzymatic electron reduction of DOX thus affecting the cell membrane directly. The oxidized form of DOX, semiquinone- an unstable metabolite- is converted back to DOX in a process that releases reactive oxygen species (ROS), which promote a cascade of free radicals formation that leads to lipid peroxidation, membrane damage, DNA damage, and eventually triggers apoptotic pathways of cellular damage. This effect can cause the formation of greatly reactive free radicles. The formation of the highly reactive free radicles is responsible for cytotoxicity elicited by the use of DOX, though these same mechanisms of action make DOX an efficient anticancer agent against various types of cancer [15].

The specific pathway of cell death caused by the administration of DOX varies depending on: a) concentration of DOX, b) treatment duration, c) a specific form of cancer and the multidrug resistance-associated with that specific cancer type.

Moreover, the main drawback of DOX administration is DOX- associated cardiotoxicity mainly due to cardiomyopathy caused by prolonged exposure to the formed free radicals. To overcome this toxicity, DOX was encapsulated into the first FDA-approved PEGylated liposomes called Doxil® / Caelyx ®, the liposomal formulation has decreased the toxicity associated with DOX treatment [16].

1.3. Targeting

The concept of drug targeting was firstly introduced in the early twentieth century by Paul Ehrlich under the name “magic bullet”, in which an increased accumulation of pharmaceutically active ingredients (PAI) is accumulated in the required tissue or organ in the body. However, this concept was not fully applicable to most of PAI in the market as the drug accumulation in the diseased organ is highly dependent on the pathological processes or on biological pathways. The concept of drug targeting re-emerged with the investigation of the cancer tumor nature and the utility of nanocarriers for cancer treatment.

1.3.1. Passive targeting

The tumor endothelial lining of the blood vessel walls is more permeable than in the normal blood vessels (Figure 2). This is a confirmed phenomenon and is clearly demonstrated and reported in many tumors [17,18]. As a result of this phenomenon, in the tumor areas, nanoscale carriers can accumulate into the interstitial space. The nanoscaled carriers are loaded with PAI, where they bring these active agents to the area with thining vessels and increased permeability and subsequently, the active pharmaceutical agent is released from the nanoscale carrier into the interstitium. Moreover, because the cut-off size of the permeabilized vessels differs from one tumor to another [17,18], the size of the nanocarrier may play a crucial role in the efficacy of such unforced “passive” DDS. The effect in which these nanoscaled carriers of a specific size are permeabilized into the vessels and are accumulated in the tumors is referred to as Enhanced Permeability and Retention effect (EPR) (Figure 2)[19]. The EPR effect requires long circulation nanocarriers thus the incorporation of polyethylene glycol (PEG) grafted to the surface of these nanocarriers and prevented their rapid clearance by the reticuloendothelial system [20]. The prolonged circulation of the nanocarriers is advantageous due to the possibility of maintaining the required concentration of PAI after a single dose only, as well as the possibility to enhance the targeting into the tumor interstitium with limited blood supply.

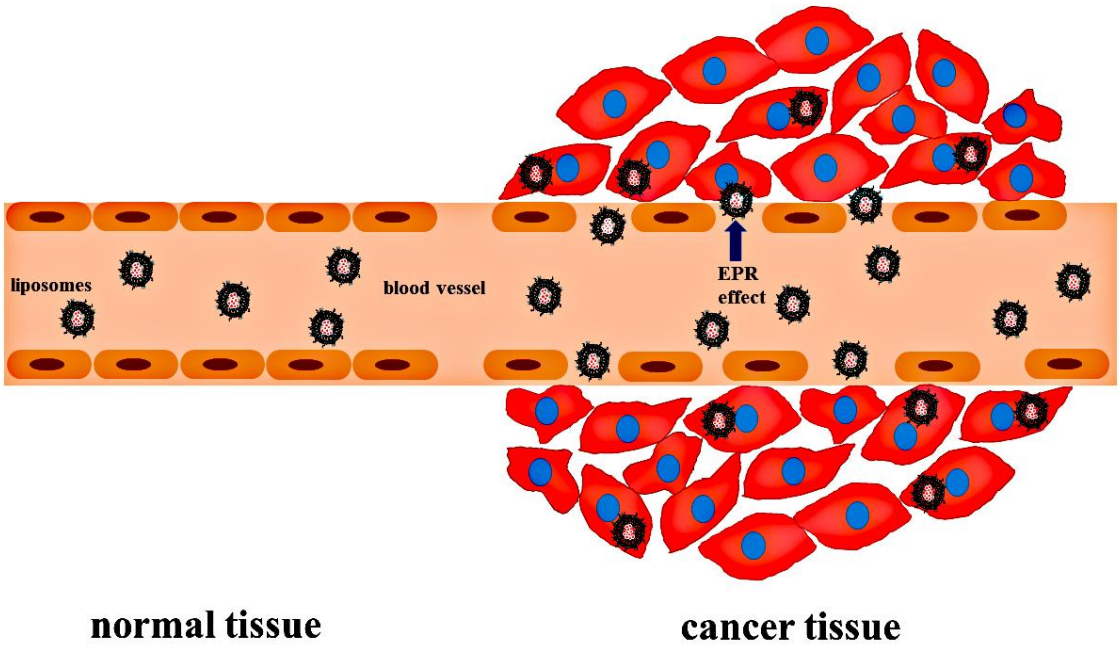

Figure 2: *Schematic representation of the EPR effect (passive targeting in cancer tissue).*

1.3.2. Active targeting

Since the EPR is dependent on the poor integrity of vascular endothelium, it is hampered, where the vasculature integrity remains unaffected. There are many approaches for drug targeting including the utilization of temperature, pH, or magnetic targeting. However, these are not universal. In some tumors, the affected area does not differ from the normal tissue regarding vascular permeability, local pH or temperature. Magnetic drug targeting is often restricted by the efficient blood flow rate in the targeted area. Thus decreasing the efficiency of passive targeting. Therefore, active targeting comes as an urgent need as the most universal and natural way for a nano specific drug affinity. Active drug targeting requires the surface modification of the nanocarrier (e.g., liposomes) with a targeting moiety that is capable of specific and selective recognition and binding to the targeted site (Figure 3). This mechanism depends on the interaction between tumor ligands conjugated to the surface of nanocarriers and cell-surface receptors or antigens on cancer cell surfaces. Targeting moieties can differ between antibodies or antibodies-fragments, proteins, lipoproteins, hormones, aptamers, mono-, oligo-, and polysaccharides, hormones, lectins, and some other ligands, e.g. folate [21]. A number of

nanocarriers formulations have been developed for the active targeting purpose to improve anticancer efficacy and to reduce side effects.

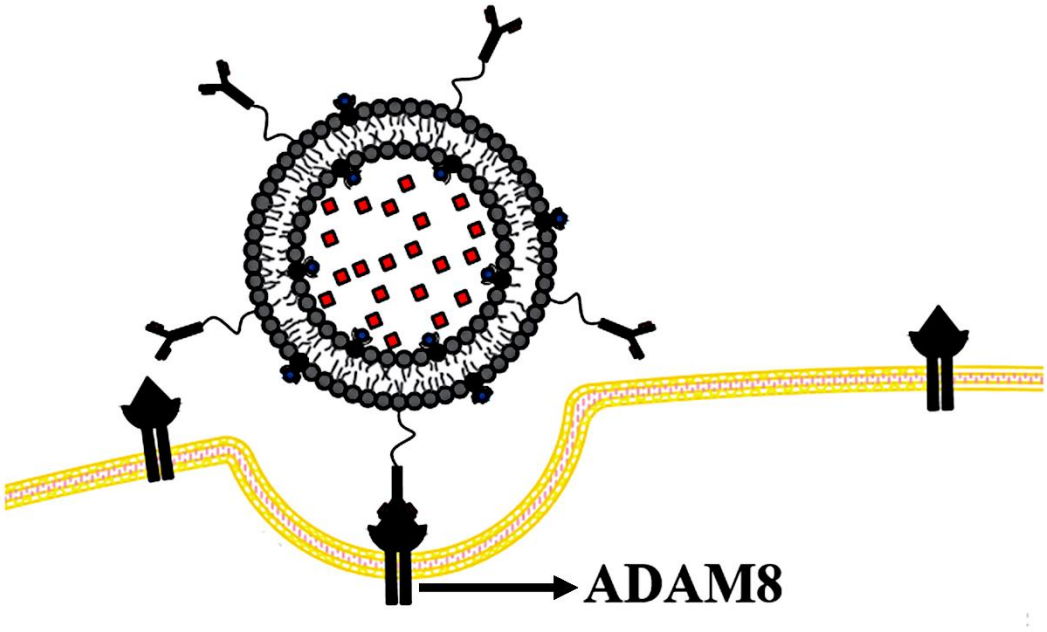

***Figure 3**: Schematic presentation of active targeting. With anti-ADAM8 antibody MAB 1031-modified liposomes bind to the overexpressed ADAM8 antigen on the cellular surface.*

1.4. Liposomes

The discovery of liposomes in the mid-1960s [22] and their similarity to cell membranes introduced cell biologists with a convenient tool to study cell membrane functions. However, the actual consideration of liposomes as a candidate for drug delivery of PAIs was not until several years later in the 1970s [23,24]. Liposomes are vesicles that vary in size between 25 nm to 2500 nm [25]. Several factors define liposomes properties: i) lipid composition, normally liposomes are composed of phospholipids, and they may include other lipids. The membrane encloses an aqueous core that can be used to encapsulate hydrophilic drugs, whereas lipophilic drugs can be incorporated into the liposomal membrane [26]. ii) The number of the lipid bilayer; either unilamellar (consisting of a singular phospholipid bilayer) or multilamellar (consisting of two or more separated by water) [27]. iii) Size, surface charge, and the method of preparation are as well crucial factors affecting the liposomal vesicles half-life as well as the quantity of the active ingredient being encapsulated [25].

Recent advances in biomedical and pharmacological sciences facilitate the design and synthesis of a wide range of new agents with potential activity against a high number of therapeutic targets in vitro, especially cancer treatment. Many cytotoxic agents were quite successful *in vitro*, however, the clinical translation of these agents failed for numerous bioavailability related reasons: a) the inability to reach therapeutic concentrations in the active site, b) the nonspecific cytotoxicity affecting bone marrow, GI, renal and cardiac tissues (e.g. dose-related cardiac toxicity associated with DOX treatment), or problems related to the drug itself, i.e. problems related with the stability, solubility or other formulation related problems [28]. To overcome these drawbacks, cytotoxic agents can be encapsulated into liposomes, to minimize the side effects and enhance their therapeutic index without compromising the antitumor efficacy [29]. Liposomes allow the transportation of cytotoxic agents and protect them from degradation [30]. They pertain distinctive features that make them suitable for drug delivery: they are biodegradable, non-toxic, biologically inert, stable within biological environments, show controllable release behaviors i.e. triggered release by temperature, pH or others and are biocompatible. The possibility of coating their outer membrane with long polymer chains such as polyethylene glycol (PEG) that make them stealthier and prolong their circulation time [25,31].

1.4.1. Preparation of liposomes and DOX remote loading

The method of liposomes preparation affects its size, lamellarity, shape, and encapsulation efficiency of the loaded drug. Therefore, addressing the preparation method in advance is essential to reach the desired liposomal properties.

Conventional methods for preparing small and large unilamellar vesicles (SUVs and LUVs) are:

A) Injection of organic solvent with dissolved phospholipids into an aqueous phase [32,33]
B) Reverse phase evaporation [34]
C) Detergent dialysis [35,36].

Conventional methods for preparing multilamellar vesicles (MLVs) are categorized into these main methods:

A) Hydration of a phospholipid film under hydrodynamic flow [37]
B) Solvent spherule method [38]

C) Hydration of stable, dry, free-flowing granular composites containing a phospholipid and a carrier/drug (Proliposmes) [39]
D) Thin-film hydration, his method involves obtaining a thin lipid film in a round-bottom flask by the removal of organic solvent, usually in a vacuum evaporator. Upon the addition and agitation of the dispersion aqueous medium, heterogeneous liposomes are formed [40].

The formation of MLVs is easily achieved spontaneously, various techniques such as sonication, homogenization and membrane extrusion are often used to convert the MLVs into SUVs and LUVs.

One of the major hurdles in the pharmaceutical application of liposomes is their efficient and stable loading with the pharmaceutically active ingredients. This is of special importance when liposomes are of small size [41]. DOX is preferentially delivered to the tumor site using liposomal-DOX, it has been previously reported that liposomal associated DOX drug delivery systems improve the therapeutic index by increasing the cumulative dose of DOX treatment with reduced cardiac toxicity [42,43]. Therefore, obtaining a method able to load a higher amount of DOX with the associated liposomal DOX decreased toxicity is highly desirable. There are four reported strategies for efficient drug loading, which are driven by the use of pH-, sulfate-, manganese- or citrate-gradient. Bahrenholz and his working group were the first to achieve a method for efficient DOX loading using ammonium sulfate [44]. The method was fast, resulted in stable liposomal vesicles when stored up to two years. Effective and applicable for liposomes prepared by different preparation methods, not affected by the liposomal lipid composition as well as applicable for various drugs with the same physiochemical properties (amphipathic weak bases) [44]. Mainly all drug loading techniques follow the same principle, i.e., the free DOX amphipathic base diffuses into the liposomal payload using a specific gradient. This modification of DOX occurs due to the salt present in the payload which prevents the membrane permeation, results in the accumulation of a sufficient amount of DOX inside the liposomes. Figure 4 represents the intraliposomal remote loading of DOX by mean of an ammonium sulfate gradient between the intraliposomal aqueous payload and the external medium.

Ammonia efflux is the main driving force for the influx of the amphipathic base (DOX), it produces a $[H^+]$ gradient, where $[H^+]$ in liposomes > $[H^+]$ in the medium. Unprotonated DOX-NH complex crosses the liposomal membrane and therefore is then protonated [45]. In the

presence of SO_4^{-2} a gel-like precipitate is formed [46], thus entrapping the DOX in the aqueous phase of the liposomes without re-permeation to the surrounding medium.

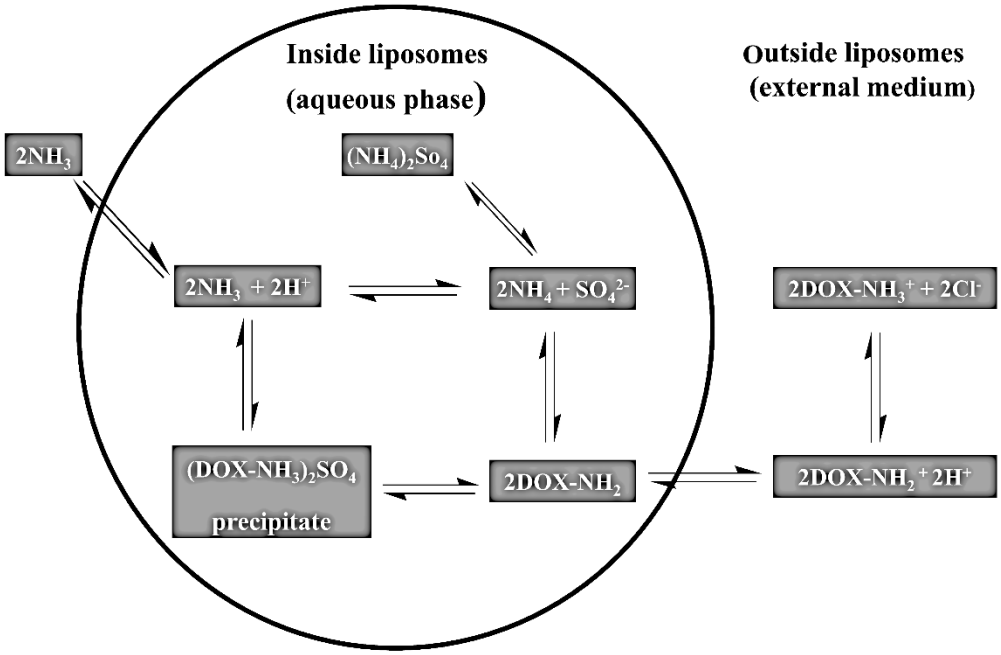

***Figure 4**: Remote loading of DOX into liposomes via ammonium sulfate gradient method.*

1.4.2. Thermosensitive liposomes and DOX triggered release

The majority of the liposomal drugs are formulated in an intention to remain permanently entrapped in the liposomal carrier upon systematic administration and following circulation. 98 % of reported DOX PEGylated liposomes remained entrapped during the circulation up to 7 days [47,48]. This contributes to the observed desirable pharmacokinetics of DOX PEGylated liposomal formulations as most, if not all liposomal drug will remain restricted to the blood circulation, which will cause a low volume of distribution in comparison to the free drug. On one hand, a stable DOX entrapment prevents major cytotoxicity, i.e., cardiotoxicity. On the other hand, this feature regarding DOX PEGylated liposomes circulation has turned out to be a major drawback after arriving at the tumor, where supposedly DOX become bioavailable to the tumor cells highly stable DOX formulations, this feature is severely hampered.

Moreover, the efficiency of DOX treatment is directly related to its cumulative dose within the tumor. The conventional nanocarriers based DDSs aim to release the encapsulated DOX as soon as the nanocarrier reaches the tumor [49]. Where the tumor is exposed to inadequate concentrations of DOX over a long period of time, thus increasing the probability of tumor developing multi-drug resistance (MDR) [50]. Long story short, as a result of slow accumulation of the liposomal DOX in the tumor in combination with the instant release, the concentration of the existing concentration of DOX in the tumor will increase gradually proportional to the liposomes concentration. Therefore, the tumor is exposed to DOX concentration in the sub-lethal concentrations < LD_{50} throughout the accumulation time *in vivo* (24 h) [51], and this will increase the likelihood of developing MDR.

Moreover, to overcome the abovementioned drawbacks regarding DOX release, Yatvin *et al.* introduced the first thermosensitive liposomes, that remain intact in the physiological temperature and prevent premature leaking and subsequently release the encapsulated drug upon triggered release caused by external hyperthermia [52]. Gaber *et al.* introduced the first thermosensitive DOX liposomes, thus allowing the concentration of DOX to reach higher concentrations the sub-lethal dose > LD_{50} [53]. Yatvin *et al*. introduced pH-sensitive liposomes to elevate DOX release using the advantageous acidic surroundings in the solid tumor [54]. However, these liposomes were shortly introduced with a major drawback regarding DOX encapsulation due to their low pH payload which prevented adequate DOX loading using pH gradients. Thereafter, the best approach for the delivery of an adequate concentration of liposomal DOX is the utilizing of thermosensitive liposomes.

DPPC (1,2-dipalmitoyl-sn-glycero-3-phosphocholine) is the most reasonable lipid that is used in thermosensitive liposomes since it is has a phase transition temperature of T_m = 41 °C. Phase transition temperature represents the temperature required to transfer from liquid condensed to the liquid expanded phase of the lipid mixture of the liposomes. By incorporating DSPC (1,2-distearoyl-sn-glycero-3-phosphocholine, T_m = 56 °C) with various proportions, one can obtain any phase transition temperature between 41 – 56 °C. Both lipids are quite miscible and after differential scanning calorimetry analysis only single-phase transition temperature is observed [52]. Moreover, DPPC is adopted as the main lipid of all reported thermosensitive liposomes [53,55-57]. Gaber *et al*. reported stealth DOX thermosensitive liposomes containing DSPE-PEG as well as cholesterol beside DPPC and DSPC with 50 % of DOX released after 30 min of heating at 42 °C [53]. Although they have obtained very promising results *in vitro*, no *in vivo* translation was additionally investigated.

Furthermore, recently thermosensitive DOX liposomes importance has risen in the nanocarrier research field with the new developed most studied thermosensitive liposomes (ThermaDOX®). The intravascular release refers to an approach in which the main site of the DOX release takes place within the blood vessels of the tumor [58]. Prior to the treatment, the tumor site is ensured to reach physiological temperature or in some cases, it is heated to an appointed temperature, once thermal equilibrium is established, DOX liposomal formulation is injected. The DOX formulation aims to destroy the endothelial vasculature of the tumor that is located in the previously heated sites. Some of the most used methods for heating are water bath heating, where this method offers a higher accumulation in tumor vasculature [57] and the released DOX at the heated area is able to damage the vessels that nourish the tumor [58]. The heating using a water bath showed successful results *in vitro*, which offer higher initial plasma vesicle DOX concentrations and higher vascular permeability. However, heating by water bath is inapplicable *in vivo*, the utility of clinically available methods for heating, i.e. radiofrequency (RF), high intensity focused ultrasound (HIFU), have been heavily studied and investigated due to fulfill the urgent need.

1.4.3. Phase transition temperature of liposomes

The fundamental principle behind drug release from thermosensitive liposomes is the transition from liquid condensed phase to liquid expanded phase at the subtle blend of phospholipid's specific temperature (Figure 5). The transition between these phases is driven mainly by the gain of configurational entropy of the thermodynamic system; mainly the entropy of the acyl chain of the phospholipid.

It can be measured by different techniques, fluorescence spectroscopy, infrared spectroscopy, nuclear magnetic resonance (NMR), and differential scanning calorimetry (DSC) [59]. DSC is the main method used to measure endothermic and exothermic responses within a material, here phospholipids, at a designated temperature. There are three main parameters in the DSC thermogram i) the pretransition temperature, which represents the temperature between liquid condensed and liquid expanded phase of the phospholipids. ii) the maximum phase transition temperature (T_m), in this phase the major transition occurs, where it is dependent on the conformational alignments of the acyl chains in the tail group of the phospholipids allowing maximal van der Waals interactions between molecules. iii) the area under the curve is a

proportional relation to transition enthalpy (*ΔH*), which represents the energy required to melt the acyl bonds in the tails of the phospholipids [60,61].

The thermodynamic driving force that determines the phase transition temperature is illustrated by the Gibbs free energy equation *(ΔG):*

$$\Delta G = \Delta H - T_{\mathrm{m}}\,\Delta S \qquad \textit{Equation 1}$$

Where *ΔH* = enthalpy change, T_m = phase transition temperature, *ΔS* = entropy change.

At an equilibrium phase *ΔG* = 0, thus the enthalpy change is given by

$$\Delta H = T_{\mathrm{m}}\,\Delta S \qquad \textit{Equation 2}$$

T_m is measured by:

$$T_{\mathrm{m}} = \frac{\Delta H}{\Delta S} \qquad \textit{Equation 3}$$

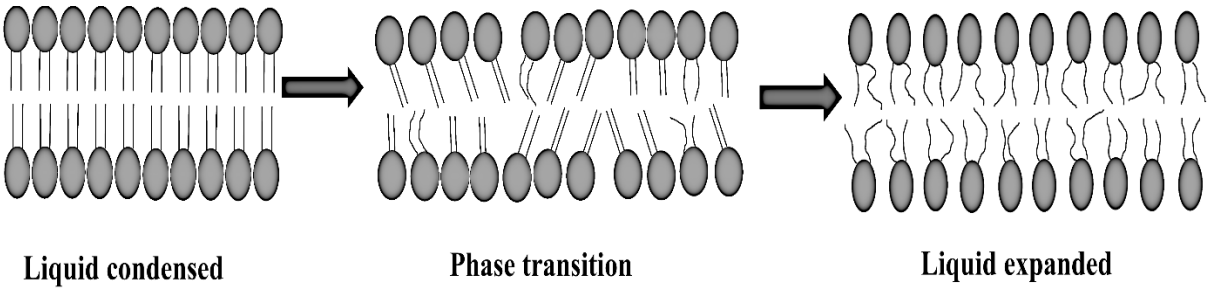

Figure 5*: Phospholipid bilayer membrane phase stages upon heating. The phospholipid bilayer is in the liquid condensed phase ($T < T_m$), it changes to liquid expended phase after the melting of head and chain groups at ($T > T_m$). During the phase transition, the membrane shows a high permeability.*

1.4.4. Paramagnetic thermosensitive liposomes

Thermosensitive liposomes, which are mainly composed of DPPC enhance the payload release near the phase transition temperature of the liposomes. There are numerous attempts to develop new thermosensitive liposomes to improve their thermosensitivity and thermal response. The incorporation of a heat-responsive substance such as polymers [62] or heat-inducing material that generates heat as a response to an external source such as laser [63], ultrasound [64] or magnetic field [65] can elevate the temperature allowing the triggered release of thermosensitive liposomes cargo.

One of the recent updates of the innovative thermosensitive liposomes formulations is including HIFU, RF and alternating magnetic field (AMF).

Of most concern to use here are paramagnetic liposomes as MRI contrast agents developed for both imaging-guided DDS and the hyperthermia to open the thermosensitive liposomes and released of the drug (Figure 6). Assessed triggered release from the thermosensitive liposomes is to be discussed later. The paramagnetic liposomes could be developed by the incorporation of Gadolinium- chelate (Gd-chelate) in the liposomes [66,67].

The encapsulation of paramagnetic compounds, especially Gd-chelate, usually results in an evident reduction in relaxivity (*r1*) as the magnetic interaction with the surrounding water protons becomes limited by the restricted permeability of the water protons through the lipid bilayer of the liposomes [68]. Hence, the increase of R1serves as an indication of the successful release of the encapsulated cargo.

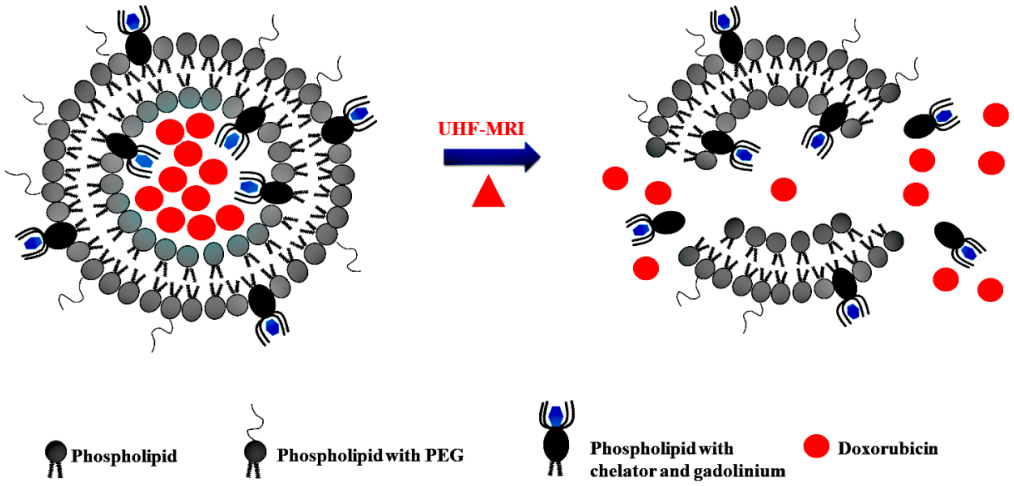

***Figure 6**: Schematic presentation of DOX release from the magnetic thermosensitive liposomes upon hyperthermia under UHF-MRI exposure.*

1.4.5. Immunoliposomes

The concept of targeted DDS has long teased scientists in many fields, perhaps in most cancer treatment fields. Immunoliposomes represents a logical strategy to achieve targeted DDS in cancer treatment. However, despite decades of preclinical investigation, immunoliposomes have yet to appear more promising to be evaluated in clinical trials. Currently, 15 immunoliposomes formulations are approved in clinical oncology [69]. Early attempts to develop immunoliposomes as a targeted DDS faced several obstacles involving the immunoliposomes constructions: identifying the target antigen, antibody, antibody-liposomes linkage, liposomes composition, structure and functionality and the drug encapsulated.

Furthermore, immunoliposomes represent an advanced strategy to enhance liposomal DDS, by linking liposomes to monoclonal antibodies (MAbs), which are directed against tumor antigens. Most tumor-chosen antigens are overexpressed on tumor cells contrary to normal cells. However, the overexpression of the tumor antigen does not occur homogeneously in all the cancer cells, thus giving an obstacle for the immunoliposomes to target the required antigen [70]. Additionally, the site-specific targeting offered by immunoliposomes can increase the therapeutic efficacy and decrease the cytotoxicity. In order to obtain a liposomal targeting system, an antibody has to be conjugated to the surface of the liposome [71]. Several methods for the antibody conjugation were reported, mostly differing in their chemical basis [72-74]. However, these liposomes were of a limited benefit due to their rapid circulation clearance, the introduction of PEG prolonged the liposomes circulation and helped to enhance targeting.

For the targeting experiments, it is essential to obtain a successful surface modification of the liposomes. A suitable anchor is an essential factor in the modification process. A method of rapid and simple coupling is of great importance in our research. Furthermore, a rapid method of coupling of the antibody at the end-group of a derivatized PEG with cyanuric chloride was firstly introduced by Bendes *et.al* and his working group and is currently commercially available [69,75]. This method needs only a few preparative steps and is feasible without prior manufacturing processes. The cyanuric group enables antibodies conjugation without any prior derivatization [75]. A great advantage of this form of binding is its simplicity. Additionally being very cost-effective especially when using sensitive and expensive targeting moieties such as antibodies.

1.5. Ultra high field magnetic resonance imaging

Ultra high field magnetic resonance imaging (UHF-MRI) is a non-invasive imaging technique that produces three-dimensional anatomical images. It is a powerful technique in diagnostics, disease detection as well as treatment monitoring. MRI was firstly introduced by Paul C. Lauterbur in 1973 when he has published images represent the Nuclear Magnetic Resonance (NMR) response of the hydrogen nuclei in a pair of water glass capillaries [76]. Only 1-D projections could be obtained while applying a magnetic field in various directions. Soon after, Peter Mansfield introduced a method to acquire efficient images, including slice selection [77]. Afterward, fast acquisition schemes were developed, where entire 2-D images could be acquired within a few tens of milliseconds [78].

MRI was restricted to laboratory use in its first years of discovery and its application flourished into the market after a postdoctoral fellow implemented Fourier (spin-wrap) imaging and could acquire the first clinically useful image of a human subject [79]. Over the last few decades, MRI tests and images have become widely used as a routine diagnostic procedure. It is estimated that the number of scans performed every year exceeds 100 million [80]. MRI technology is moving towards a large installed base of 7 T (Tesla) systems. New MRI scanners are equipped with ultra high magnetic fields (UHF) $\geq$ 7 T. There are some other trends regarding MRI application, such as the combination of Positron emission tomography (PET) and MRI and the integration of soft tissue imaging of MRI with other noninvasive procedures, i.e. MR-guided focused ultrasound.

MRI employs a powerful magnetic field that forces protons in the body to align with the given field. It is based on a sophisticated technology that excites and detects the change in the direction of the proton´s rotational axis of those protons found in water that makes up the tissues.

MRI is considered the most complex imaging technology in the market. Whereas most imaging techniques portray differences in one, or sometimes two, tissue characteristics, MR depicts five tissue variables; i) spin density, ii) T1 and iii) T2 relaxation times, iv) flow and v) spectral shifts. These variables can be combined in several ways through selecting puls sequence and puls time [81]. The most interesting characteristics in DDS research are T1 and T2 relaxation times.

Relaxation defined as the process in which spins release the energy received from a radiofrequency pulse. T1 relaxation time, also known as spin-lattice or longitudinal relaxation time, is a measure of how quickly the net magnetization vector recovers to its ground state in

the direction of the offset frequency (static magnetic field) B_0 [82]. The recovery of the excited nuclei from the high energy state to the low energy state is associated with loss of energy to the surrounding nuclei. NMR was used originally to examine solids in the form of a lattice, hence the term " spin-lattice" relaxation [83].

T2 relaxation, also known as spin-spin or transverse relaxation time, represents the progressive dephasing of the spinning dipoles after the 90 ° pulse as illustrated in a spin-echo sequence due to tissue-specific characteristics, especially those that affect the rate of proton´s movement, most of which are found in water molecules [84]. Another term that is common when describing relaxation is the relaxation rate (R), which refers to the reciprocal of the T1 or T2 time 1/T1 (R1) or 1/T2 (R2). T1 relaxation is the fastest when the rotation and translation of the nucleus match that of Larmor frequency (Larmor frequency represents a phenomenon when a magnetic moment is placed in a magnetic field it will tend to align with the field). Subsequently, T1 relaxation is dependent on the magnetic strength of Larmor frequency. Therefore, a higher magnetic field means higher T1 relaxation times [85].

R1 and R2 of the nuclei of liquids characterize the rapidity with which a thermodynamic group of similar nuclei achieves thermal equilibrium. For partially deuterated water, i.e., every proton must be coupled to a thermal background, "the lattice" mentioned earlier, through a noisy interaction that is modulated by Brownian thermal motion, which transfers the lattice temperature to the nuclear ensemble. Moreover, the motional narrowing described by Bloembergen [86] and Solomon [87] dominates the relaxation. Briefly, a given water molecule senses the local dipolar magnetic field that is generated by a nearby water proton and a rapid rotation and translation of water molecules occur.

1.5.1. Contrast agents

Contrast agents are widely used in MRI. The most dominant contrast agent in clinical applications of MRI is gadolinium-based (Gd) T1 contrast agents, which strongly increase signal intensity on T1-weighted images, shorten images acquisition time, and thereafter improve diagnostic confidence. Contrast agents are mainly characterized by their relaxivity (*r1* and *r2*), which as abovementioned is defined as the change of relaxation rate of solvent water protons upon the addition of contrast agents. Another clinically used T1 contrast agent is manganese, however, is it not as commonly used as Gd-based T1 contrast agents as the research on this agent is still at an early stage [88]. Iron oxide [89] and iron platinum [90] are T2 contrast

agents, which enhance the T2-weighted images. However, these two agents were withdrawn from the market on the basis of safety issues [91].

Gd(III) is a lanthanide metal that occurs usually in a water-soluble salt that is very toxic to mammalians, one of the well-known factors related to Gd^{3+} toxicity is its similar size and competition with Ca^{2+} in cellular processes. Gd^{3+} is capable of inhibiting voltage-gated and stretch-activated calcium channels. Thereafter, Gd^{3+} can cause inhibition of crucially vital physiological processes associated with muscle tissue functionality and neurons. Gd^{3+} can as well block Ca^{2+} dependent enzymes [92,93].

Chelation has been used in medicine to treat acute metal poisoning or chronic metal exposure. Chelation is defined as a chemical procedure in which a chemical chelating agent is utilized to bind metal ions, resulting in the formation of metal chelates that are easily eliminated from the body. To overcome free Gd^{3+} toxicity and to benefit from its feasibility as a contrast agent, free Gd^{3+} is chelated with multiple chelating agents. The most common chelating agents for Gd^{3+} are either macrocyclic chelating agents, e.g. tetraazacyclododecane tetraacetic acid (DOTA), or linear chelating agents, e.g. diethylenetriaminepentaacetic acid (DTPA). Gd-DTPA is commercially available as the widely used Gd-chelate contrast agent Magnivest®. While free Gd^{3+} is highly toxic, Gd-chelate contrast agents have been listed as nontoxic according to FDA (FDA 3/16/2018). However, some reports have linked a rare medical event with Gd-chelate. Gd-chelates were mentioned as the cause of Nephrogenic Systemic Fibrosis (NSF), which is a potentially fatal medical case that causes the hardening of the skin and internal body organs [94]. Moreover, Gd-chelate is excreted by the kidneys, individuals with underlying kidney problems should obtain extra care. New reports have suggested that Gd-chelate may cause nephrotoxicity. Thereby, excessive hemodialysis after exposure to Gd-chelate is advised in individuals with endangered renal profile [95].

Furthermore, T1 relaxation of tissue and blood increases with the increasing magnetic field. For a contrast agent with equal *r1* at two fields, the T1 change would be higher at the greater field because of the inherent tissue R1 is slower at higher field. This is true for commercial extracellular agents like widely used Gd-DTPA, where its relaxivity is fairly independent of the magnetic field [96].

1.5.2. Image-guided drug delivery system

Imaging plays a crucial role in the preclinical evaluation of nanomedicine based DDS. It has laid out important insight into their mechanism of action, pharmacokinetics and biodistribution destiny, provided a deeper understanding of their therapeutic effect, and their accumulation at the target site and *in vivo* drug release characteristics. Its main role is to support the clinical development of nanomedicine DDS and utilize them for the market.

Recently, image-guided DDS, which supports clinical imaging modalities for guidance and regulation of DDS, have heavily emerged as a feasible strategy for enhancement of targeting and personalized DDS therapy [97]. In the DDS paradigm, imaging mediated DDS may be used to identify targeted and non-targeted anatomies by the used nanocarrier, which may as well help with monitoring, planning, and postprocedural assessment of the target as well as provide a deeper understanding of the treatment outcome.

At the preclinical level, image-guided DDS is mainly used for noninvasive visualization and quantification of the behavior of nanocarriers upon administration. MRI is particularly used for such purpose because of its ability to obtain images and quantitative measurements of a high spatiotemporal resolution during therapy. Diffusion-weighted magnetic resonance imaging sequence (DW-MRI) is applied to generate high-quality images. The DW-MRI is mainly identified as the use of specific MRI sequences that facilitate the generation of images, which uses the diffusion of water molecules [98]. This enables the longitudinal assessment of the nanocarrier accumulation at the pathological sites, i.e., tumors, metastases, and inflammatory lesions. Additionally, endangered off-target cells and tissues can be visualized. By the incorporation of imaging in DDS, more meaningful information can be obtained. Imaging enables the direct comparison of several materials within a single preclinical subject. This characteristic minimizes the variability in the target site as a result of preclinical subjects differences in e.g. tumor size, immune response, tumor vascularization. This allows insight for personalized medicine and personalized comprehensive understanding of DDS behavior subject's body in the era of personalized medicine [99].

1.5.3. Hyperthermia-mediated drug delivery

Hyperthermia in DDS refers to the application of heat from various sources resulting in heat temperature higher than normal physiological temperature. Hyperthermia in DDS is generally divided into two main categories, mild (~ 40 – 45 °C) or ablative (50 – 100 °C) [97]. It is usually obtained from radiofrequency [100], microwaves [101], or laser [102]. Ablative hyperthermia is used to destroy the tumor and reduce its growth in regions of sublethal margins. Mild hyperthermia is used mainly to trigger the release of the drug from a thermosensitive carrier.

Moreover, RF is applied in MRI measurements, wherein this technique has been under investigation to evaluate its safety to the normal tissues. After the introduction of ultra high field MRI, this topic has reemerged and gained higher importance in the research. Increasing the magnetic field strength changes the interaction between the applied RF field and the tissue. The higher frequency applied due to a higher field shortens the wavelength, thus leads to more noticeable local interactions [103]. Moreover, this pronounced interaction between the RF and the tissue is translated into thermal energy, reports have observed an increase of about 1-2 °C [104-106]. Consequently, the increased temperature during MRI measurements was utilized to induce mild hyperthermia to our DDS.

1.6. ADAM8 targeting with modified liposomes

1.6.1. Disintegrin and metalloproteinase domain 8 (ADAM8)

ADAM8 is a transmembrane protein belongs to a disintegrin and metalloproteinase family (ADAMs), which obtains a domain-containing protein 8, ADAM8 was firstly identified by Yamamoto´s group in Japan. It was described as cDNA cloned from mouse monocytes cell lineages [107]. It is a protein that is composed of 824 amino acids, 637 amino acids from the extracellular matrix, 16 amino acids form signal peptide, 25 amino acids build the transmembrane region, and 146 amino acids that are in the cytoplasmic region, which are of great importance because have the Src homology 3(SH3) binding domain. ADAM8 and its corresponding family (ADAMs) mediate cell adhesion, proteolysis of various substrates, i.e., cytokine receptors, cell adhesion molecules and extracellular matrix components, as well as

promote cell migration [108]. ADAM8 can either dimerize or multimerize and autocatalytically hook off its domain, resulting in an active membrane-anchored metalloprotease.

ADAM8 is activated by autocatalysis in the trans-Golgi stack [109]. The activated ADAM8 can additionally be processed by the release of the metalloprotease domain into the extracellular matrix leaving residues from within the membrane (Figure 7). Both active and residual forms of ADAM8 mediate cell adhesion throughout their disintegrin/cysteine-rich/EGF-like domains [109], mainly by direct binding to integrins [110].

Active ADAM8 has no essential role under normal physiological conditions [111,112], despite its expression in multiple immune cells. ADAM8 is detected under multiple pathological conditions, including inflammatory diseases and cancer [108]. Wang *et.al* have found that ADAM8 is overexpressed in aggressive forms of breast cancer, including TNBCs, and is correlated with poor prognosis and very poor patients outcomes. In their research, ADAM8 was found to promote TNBCs metastases, in which ADAM8 promotes tumor growth and angiogenesis and the spreading of circulating tumor cells. Therefore, ADAM8 is a promising target for the treatment of TNBCs up to the metastatic cells [113].

Moreover, using an antibody-based carrier to target ADAM8 is counted as an effective therapeutic intervention for the identification, targeting, and treatment of TNBC [114].

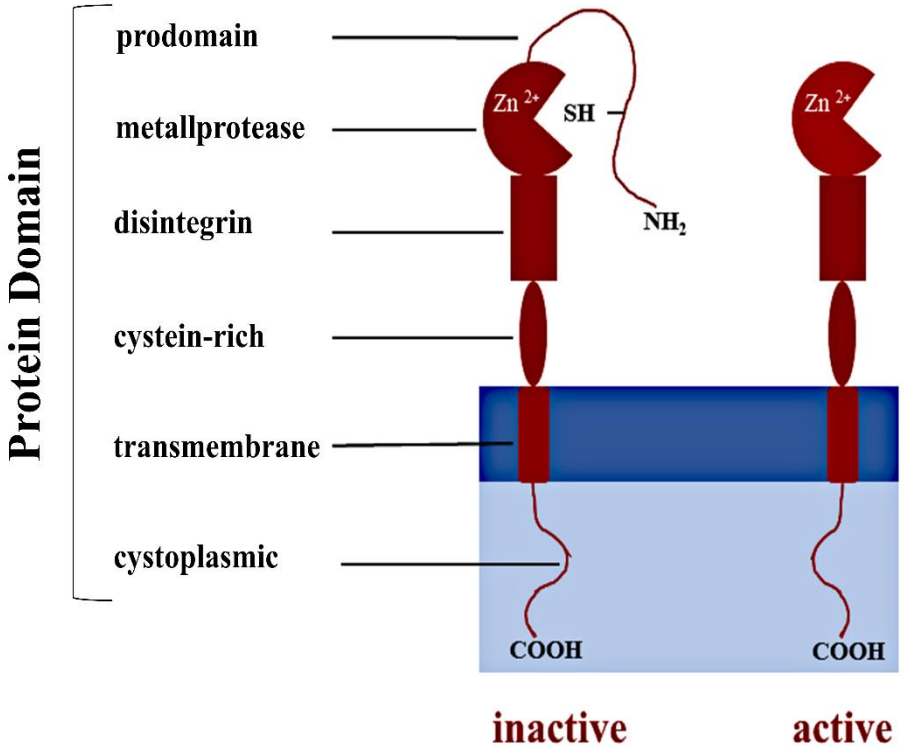

***Figure 7**: Schematic representation of ADAM8, the disintegrin domain is required for autolysis. The majority of ADAM8 proteins are processed in the cell membrane. This suggests that the extracellular shedding of other membrane proteins occurs mainly on the cell surface, thereafter, proteases release into the extracellular compartment resulting in extracellular matrix remodeling* [115].

1.6.2. MAB 1031 antibody modified liposomes for ADAM8 targeting

The targeting of surface structures on tumor cells with actively addressed liposomes is a very promising method for both diagnostic and therapeutic strategies. As abovementioned, ADAM8 is a promising novel target for the diagnosis and treatment of several tumors including TNBC. ADAM8 is an extracellular shedding metalloprotease making it a promising target for antibody modified liposomes. One of the reported strategies to actively target ADAM8 is by MAB 1031 antibody [116] (Figure 8), which is a monoclonal mouse IgG_{2B} clone [117]. MAB 1031 antibody can directly detect ADAM8 and suppress its catalytic activation, thus inhibiting the metastatic cascade corresponding with ADAM8 overexpression. MAB 1031 mainly detects an

epitope within a specific domain (aa 201-487) (metalloprotease and disintegrin domain) of the recombinant human ADAM8. As mentioned earlier, MAB 1031 requires an anchor for the successful binding to the liposomal cell surface.

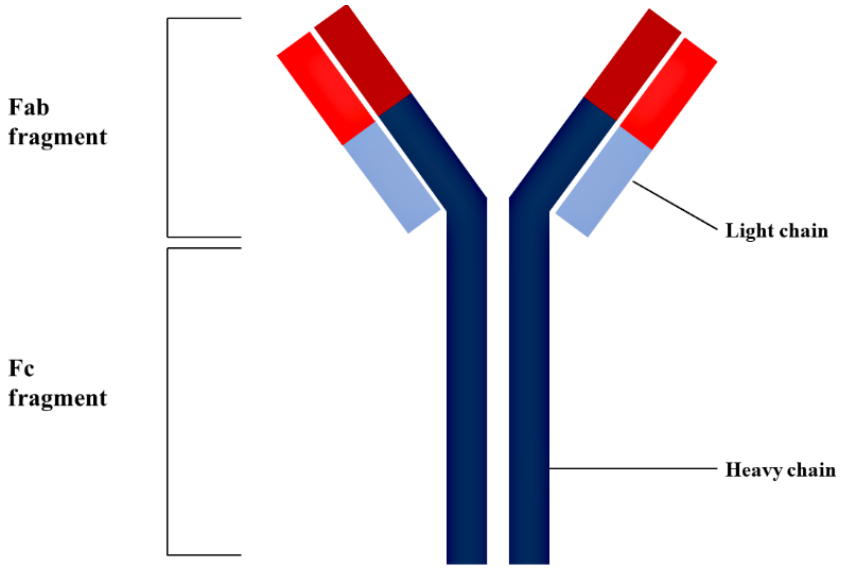

***Figure 8**: Schematic representation of MAB 1031 antibody (anti-ADAM8 antigen). MAB 1031 detects an epitope within a specific domain (aa 201-487) (metalloprotease and disintegrin domain) of ADAM8.*

1.6.3. Aim and objectives

The work presented in this thesis aimed to develop a suitable liposomal nanocarrier for DOX, that obtains thermosenitive characteristics that would allow the release of the loaded cargo DOX by hyperthermia triggered release. Moreover, the heat required for the triggered release of DOX from the liposomes is acquired from RF during UHF-MRI. Gadolinium chelate was incorporated into the liposomes to achieve both an imaging mediated drug delivery system as well as provide diagnosis of the tumor cells in their solid tumor form as well as their circulating form. Therefore, liposomes were surface modified with anti ADAM8 antibody, i.e. MAB 1031, Gd-chelate, and actively loaded with DOX. To actively target (ADAM8 antibody), image (Gd-chelate) and treat (DOX) the triple-negative breast cancer cells.

The main aspects that were achieved in this project are:

- Development of thermosensitive liposomes. Characterization of the thermosensitive capabilities using DLS, DSC, AFM and TEM.
- Active remote loading of DOX into thermosensitive liposomes using ammonium sulfate gradient. Characterization of the durg loading efficiency and drug release profile.
- Development of image guide drug delivery system by incorporation of Gd-chelate for imaging under UHF-MRI. Characterization of liposomes was achieved with DLS, AFM and TEM images provided an insight into the Gd-chelate deposition, the contrast of the Gd-containing liposomes provided an insight into the use of the liposomes for imaging under UHF-MRI. Quantification of relaxation rate after heating of the liposomes provided a proof for the heat-responsive properties of liposomes, as well as cytotoxicity assay of the liposomes under different temperatures and time intervals
- The conjugation of MAB 1031 antibody to the liposomes resulting in immunoliposomes. MAB 1031 conjugate-immnoliposomes target TNBC cells, that show overexpression of ADAM8 receptors on their cell membranes. The characterization of immunoliposomes using DLS, AFM and TEM. Additionally, the characterization of targetability and binding capabilities of immunoliposomes against TNBC cells.
- Finally, the establishment of a combined nanocarrier that utilizes thermosensitive properties, image-guided drug delivery system, triggered release, and active targeting of specific receptors.

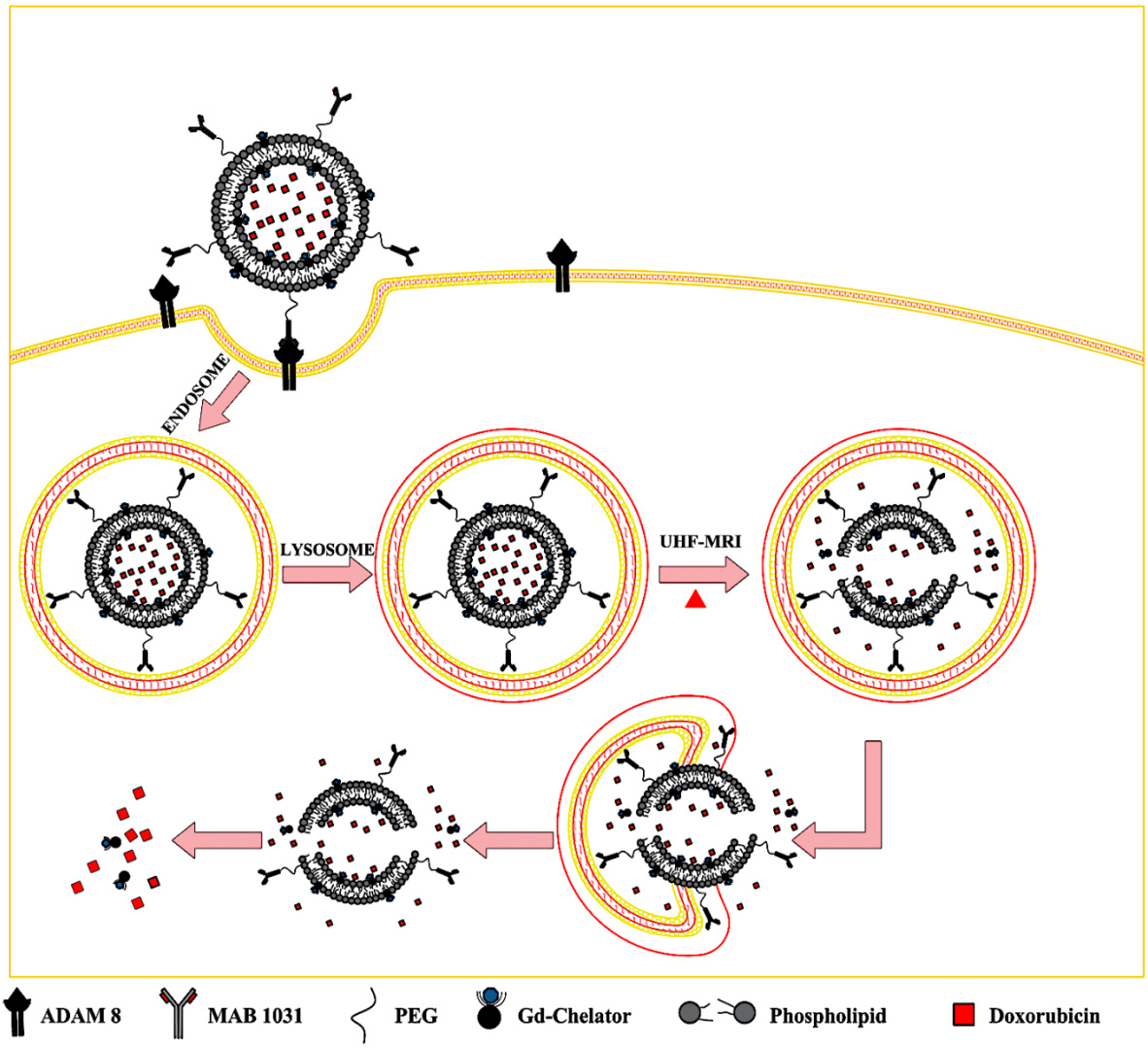

Figure 9: *Graphical abstract of the use of nanoscale carrier*

2. Materials and Methods

2.1. Material

2.1.1. List of Materials

Materials / Substances	**Source**
HEPES ≥ 99 %	VWR International GmbH, Darmstadt, Germany
0.2 µm PES syringe filters	Whatman plc, Buckinghamshire, UK
12-well plates; Nunclon Delta	Nunc GmbH & Co. KG., Wiesbaden, Germany
5 ml glass vials	Schott AG Müllheim, Germany
96-well plates	NUNC, Thermo Scientific™, Germany
Atomic force microscope; Nanowizard® 1	JPK Instruments AG, Berlin, Germany
Autoclave, Tuttnauer 3850 ELC	Tuttnauer GmbH, Linden, Germany
Ammonium sulfate	Sigma Aldrich Chemie GmbH, Taufkirchen, Germany
Cell culture lysis reagent	Promega GmbH, Mannheim, Germany
chamber slides	NUNC, Lab-Tek, Germany
Chloroform	Merck, Darmstadt, Germany
Chlorpromazine	Alfa Aesar GmbH & Co. KG., Karlsruhe, Germany
CO_2 incubator, HeraCell	Heraus GmbH & Co. KG., Hanau, Germany
Coagulation analyzer; Coatron M1	Teco GmbH, Neufahrn, Germany
Copper grids	Plano, Wetzlar, Germany
DAPI	Sigma Aldrich Chemie GmbH, Taufkirchen, Germany
Dialysis bag (MWCO = 6,000-8,000)	Repling europ B.V, Brend Netherland

Disposable folded capillary cell; DTS1060	Malvern Instruments Ltd, Malvern, UK
DMEM	Biochrom GmbH, Berlin, Germany
DMSO; ≥ 99 %	Acros Organics B.V.B.A., Geel, Belgium
DODA-DTPA	PD. Dr. U. Rothe, MLU Halle, Germany
Doxorubicin hydrochloride	OAO ONOPB, Moscow, Russia
DPPC	Lipoid GmbH, Ludwigshafen, Germany
DSC-7	Perkin Elmer, Rodgau, Germany
DSPC	Lipoid GmbH, Ludwigshafen, Germany
DSPE-mPEG-2000	Lipoid GmbH, Ludwigshafen, Germany
DSPE-PEG2000-Cyanur	Avanti Polar Lipids Inc., Alabaster, USA
Egg puncher	Schuett biotech, Göttingen, Germany
Eppendorf pipette	Eppendorf, Hamburg, Deutschland
Ethanol	Carl Roth GmbH + Co. KG., Karlsruhe, Germany
Ethidium bromide	Sigma Aldrich Chemie GmbH, Taufkirchen, Germany
Extruder; Avanti Mini	Avanti Polar Lipids Inc., Alabaster, USA
Fertilized eggs	Mastkükenbrüterei Bormann, Rheda-Wiedenbrück, Germany
Fetal calf serum	PAA, Cölbe, Germany
Filipin III	Sigma Aldrich Chemie GmbH, Taufkirchen, Germany
Fluorescence microscope	CKX-53 Olympus, USA
FluorSave™	Calbiochem, San Diego, USA
Formaldehyde	Alfa Aesar GmbH & Co. KG., Karlsruhe, Germany
Gadolinium trichloride	Sigma-Aldrich, Taufkirchen, Germany

Glass slides	Zeiss Axiovert 100M, Carl Zeiss Microscopy, Jena, Germany
HEPES	Carl Roth, Karlsruhe, Deutschland
Infrared thermometer Scantemp 385	Carl Roth, Karlsruhe, Germany
Isotonic NaCl	B.Braun Melsungen AG, Melsungen, Germany
Laminar flow hood; Labgard Class II	NuAire Inc., Plymouth, USA
Confocal laser scanning microscope	Carl Zeiss Microscopy GmbH, Jena, Germany
Luminometer; FLUOstar® Optima	BMG Labtech, Ortenberg, Germany
Lyso Tracker® red DND-99	Thermo Fischer Scientific, Dreieich, Germany
MAB-1031	R&D Systems, Inc.,Minneapolis, USA
Magnetic stirrer; MCS 66	CAT Scientific, Paso Robles, USA
MDA-MB-231-ctrl cell	ATCC (American Type Cell Culture, Manassas, USA
MDA-MB-231-rna cell	Prof Jörg. W. Bartsch. Department of Neurosurgery, Philipps University Marburg, University Hospital Marburg, Germany
Methanol	Merck, Darmstadt, Germany
MicroCal VP-DSC	Microcal, Northampton, MA, USA
Microscopy slides	Gerhard Menzel B.V. & Co. KG., Braunschweig, Germany
MilliQ® water	Millipore Corporation, Billerica, USA
Mounting medium; FluorSave™	Calbiochem Corporation, San Diego, USA
MTT reagent	Sigma Aldrich Chemie GmbH, Taufkirchen, Germany
NBD-PE	Avanti Polar Lipids Inc., Alabaster, USA

Ø 15 mm over slips	Gerhard Menzel B.V. & Co. KG., Braunschweig, Germany
Opaque 96-well plates	Brand GmbH + Co. KG., Wertheim, Germany
Peristaltic pump	PD5001, Heidolph Instruments, Schwabach, Germany
Petri dishes	Sarstedt AG & Co., Nümbrecht, Germany
Polycarbonate membranes	Whatman plc, Buckinghamshire, UK
Rotary evaporator; Laborota 4000	Heidolph Instruments GmbH & Co. KG., Schwabach, Germany
Sephadex-G50	Pharmacie Fine Chemicals, Sweden
Sepharose CL-4B	Sigma Aldrich Chemie GmbH, Taufkirchen, Germany
Shaker KS4000 IC	IKA Werke, Staufen, Germany
TEClot aPTT-S Kit	Teco GmbH, Neufahrn, Germany
Transmission electron microscope; JEM-3010	JEOL Ltd., Tokyo, Japan
Triton™ X-100	Sigma Aldrich Chemie GmbH, Taufkirchen, Germany
Trypsin-EDTA, (0.5 %) in DPBS (10x)	Capricorn Scientific GmbH Ebsdorfergrund, Germany
UHF-MRI (7T), Clinscan	Bruker BioSpin GmbH, Rheinstetten, Germany
Ultrasound bath sonicator	(Bandelin Sonorex RK 100H, Bandelin Electronic, Berlin, Germany
Uranyl acetate	Sigma Aldrich Chemie GmbH, Taufkirchen, Germany
UV mini 1240	Shimadzu, Suzhou, China
Vacuum pump; SC 920	KNF Neuberger GmbH, Freiburg, Germany

Water bath	Bruker Biospin MRI GmbH, Ettlingen, Germany
Zetasizer Nano ZS	Malvern Instruments Ltd, Malvern, UK

2.1.2. DPPC

DPPC is a phospholipid, contains a head group (polar phosphate) and a nonpolar fatty acid chain. DPPC is an amphipathic lipid with a molecular weight of 734.039 g/mol. It is the most reasonable lipid that is used in thermosensitive liposomes since it is has a phase transition temperature of T_m = 41 °C. DPPC has the ability to arrange itself in polar and non-polar interactions to form spherical vesicles [118]. Usually, it is used with cholesterol which plays a role as a membrane stabilizer. The DPPC used for this work had a purity of ≥ 99 %. It was dissolved in 2:1 (v/v) chloroform: methanol mixture at a concentration of 10 mg/ml and stored in glass vials at -20 °C until use.

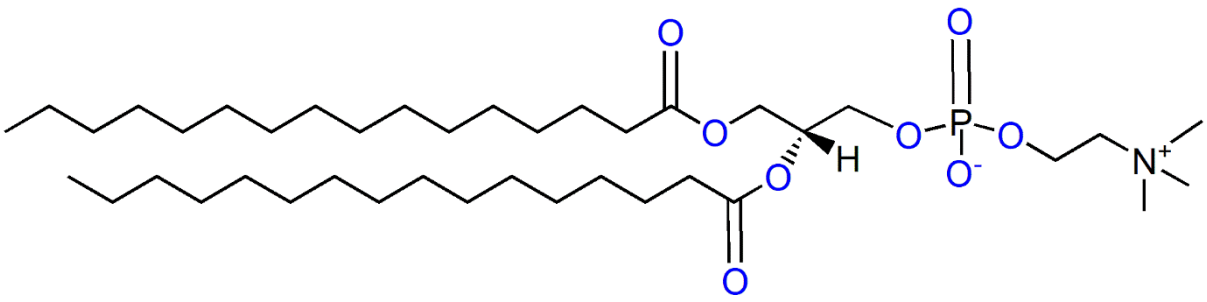

DPPC

2.1.3. DSPC

DSPC is a phosphatidylcholine with alkyl chains comprising 18 carbons [119]. DSPC is an amphipathic lipid with a molecular weight of 790.145 g/mol and it is used in several liposomal formulations. It is as well used in thermosensitive liposomes, as the unwanted drug leakage at body temperature can be reduced by mixing DPPC with small amounts of DSPC awing that its phase transition temperature is T_m =55 °C [53,120,121]. The DSPC used for this work had a

purity of ≥ 99 %. It was dissolved in 2:1 (v/v) chloroform: methanol mixture at a concentration of 10 mg/ml and stored in glass vials at -20 °C until use.

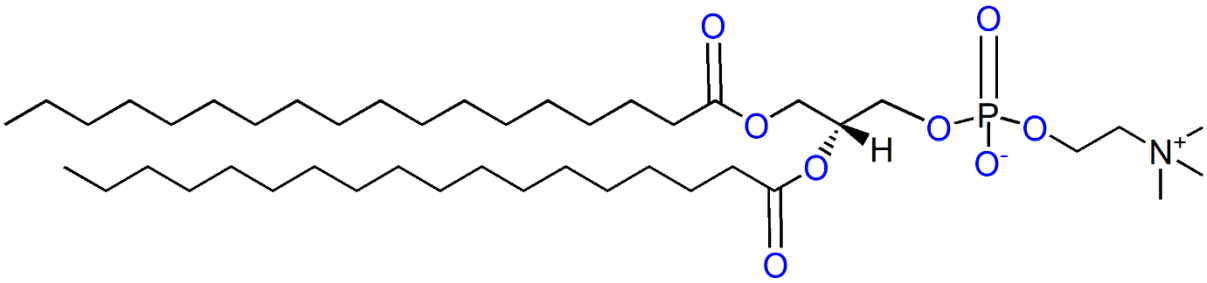

DSPC

2.1.4. DSPE-mPEG-2000

DSPE-mPEG2000 (1,2-distearoyl-sn-glycerol-3-phosphoethanolamine-N-[methoxy (polyethyleneglycol)-2000] ammonium salt) is a modified lipid that is normally added to phospholipids vesicles to provide a steric coating on the surface of the vesicles membrane making them stealthier and provide prolonged circulation plasma half-life of the nanocarrier. Its molecular weight is 2805.497 g/mol. It is used for this work with a purity of ≥ 99 %. It was dissolved in 2:1 (v/v) chloroform: methanol mixture at a concentration of 10 mg/ml and stored in glass vials at -20 °C until use.

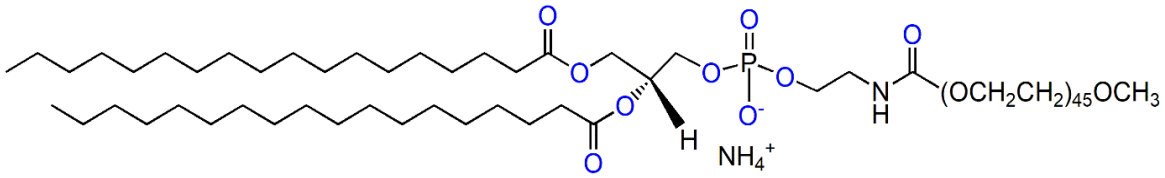

DSPE-mPEG-2000

2.1.5. Cholesterol

Cholesterol is a hydrophobic steroid molecule that exists in the serum, it is a lipophilic molecule with a single polar hydroxyl group. Its molecular weight is 386.65 g/mol. Cholesterol is incorporated into the liposomal lipid bilayer to stabilize the membrane. It prevents vesicle aggregation [122], it does as well affect the phase transition temperature of the liposomes [123]. Cholesterol was dissolved in 2:1 (v/v) chloroform: methanol mixture at a concentration of 10 mg/ml and stored in glass vials at -20 °C.

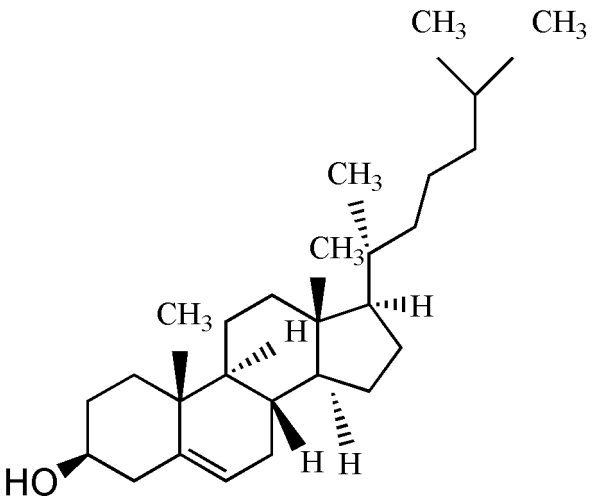

Cholesterol

2.1.6. NBD-PE

NBD-PE (1,2-dipalmitoyl-sn-glycero-3-phosphoethanolamine-N-(7-nitro-2-1,3benzoxadiazol-4-yl) (ammonium salt) is a phospholipid with fluorescent labelled headgroup. L-α-Phosphatidylethanolamine (PE) is the most copious phospholipid in bacteria and the second most copious in animals, plants, and yeast [124]. It is mostly used for fluorescence-labeled experiments. NBD-PE was dissolved in 2:1 (v/v) chloroform: methanol mixture at a concentration of 1 mg/ml and stored in glass vials at -20 °C.

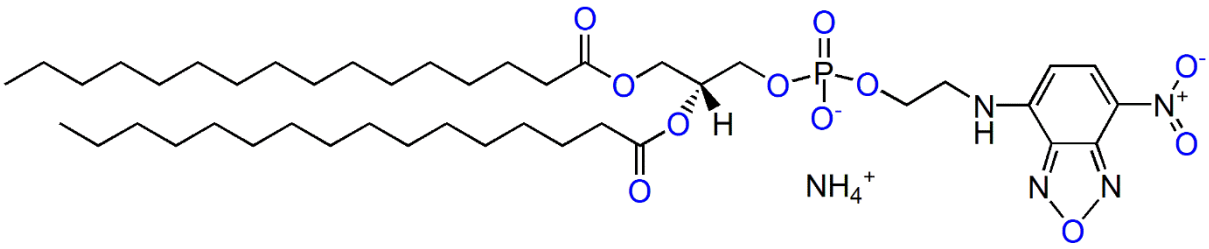

NBD-PE

2.1.7. DSPE-PEG2000-cyanur

Cyanuric PEG-PE is an end group functionalized PEG-lipid conjugate used for attachment of peptides, antibodies, etc., under mild basic conditions. Cyanuric chloride is one heterocyclic, nitrogen-containing compound with three chlorine atoms, which group links the antibodies to the PEG terminus via a nucleophilic substitution at a basic pH (8.8) with either primary and secondary amine. A big advantage of using cyanuric PEG-PE is that the proteins can be coupled to this membrane anchor without the need for any previous derivatization [75]. DSPE-PEG2000-cyanur was dissolved in 2:1 (v/v) chloroform: methanol mixture at a concentration of 1 mg/ml and stored in glass vials at -20 °C.

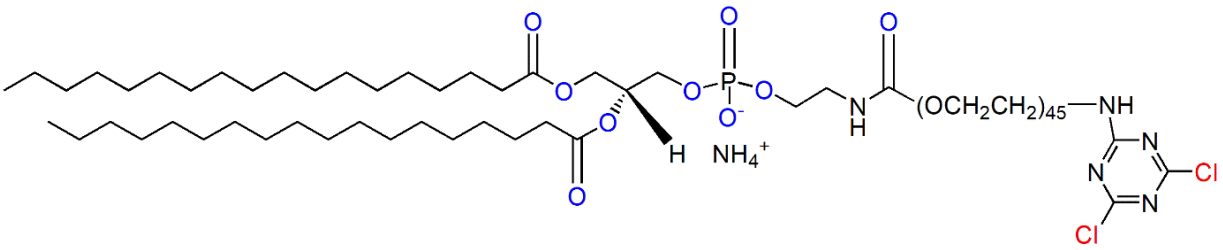

DSPE-PEG2000-cyanur

2.1.8. Chelator

2-[2-[2-[bis(carboxymethyl)amino]ethyl-[2-(dioctadecylamino)-2-oxoethyl]amino]ethyl-(carboxymethyl)amino] acetic acid is a chelator that has diethylenetriaminepentaacetic acid (DTPA) backbone that is modified with the addition of dioctadecylamine (DODA).

DTPA is a diethylenetriamine backbone with five carboxymethyl groups, while DODA is secondary amine, which is a fatty amine derivative. One of the OH groups in DTPA is substituted with a secondary amine. DODA has been utilized in the formulation of liposomes, polymeric conjugates, and others [125].

In the complex of Gd^{3+} and DODA-DTPA the Gd^{3+} ion is 9 coordinate, surrounded by the 3 nitrogen atoms and 5 oxygen atoms from the carboxylate groups (Figure 10) [126]. Notably, the 9th coordination site is occupied by a water molecule (H_2O). Thus allowing the water molecule to rapidly exchange other water molecules in the immediate vicinity of the Gd complex [127]. Hence, allowing the protonation and relaxation of water molecules under MRI [128].

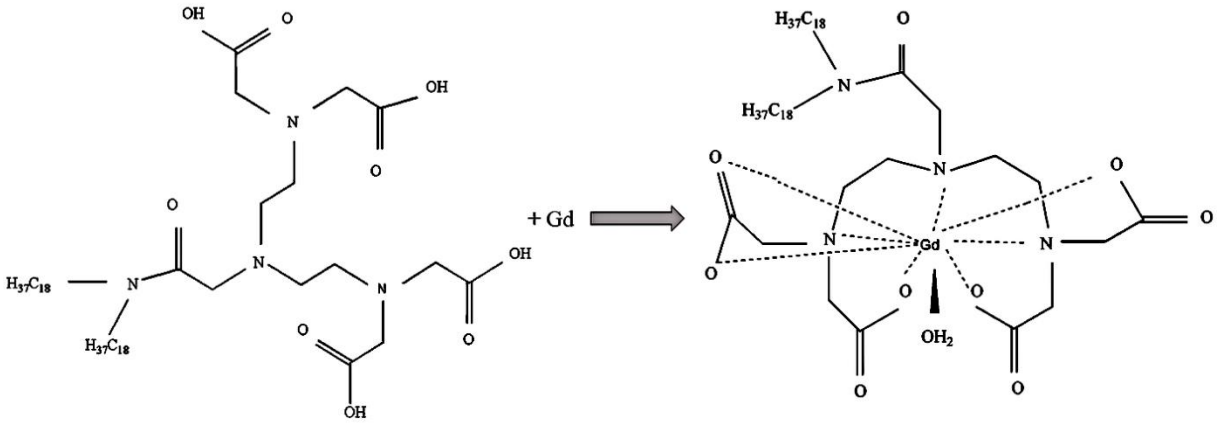

***Figure 10**: Chelating of gadolinium by DODA-DTPA.*

2.2. Methods

2.2.1. Preparation of liposomes

Three different thermosensitive liposomal formulations were prepared. Appropriate mole fraction combination of different lipids (DPPC:DSPC:Chol:DSPE-mPEG2000) at molar ratios of 89:8.8:2:0.2 was used to prepare thermosensitive liposomes (Lip_{TS}). The magnetic contrasting agent gadolinium trichloride was incorporated into thermosensitive liposomes of the previously mentioned composition adding a chelator at molar ratios of 85:7.8:2:0.2:5

(DPPC:DSPC:Chol:DSPE-mPEG2000:Chelator) leading to Lip_{TS-GD}. Magnetic thermosensitive liposomes with cyanur ($Lip_{TS-GD-CY}$) were prepared based on DPPC:DSPC:Chol:DSPE-PEG2000-cyanur:Chelator at 80:8:5:2:5 molar ratio. For fluorescence detection, 1 mol % NBD-PE was incorporated into the liposomal preparations. All liposomes were prepared using thin-film hydration techniques as previously reported [129]. Briefly, the appropriate amounts of lipids or lipids and chelator were diluted in a mixture of chloroform : methanol (2:1 v/v). The organic solvent was subsequently evaporated under an escalating vacuum using the rotary evaporator Heidolph Laborota 4000 efficient (Heidolph Instruments, Schwabach, Germany). The temperature was held slightly above the phase transition temperature of the dominant lipid in the mixture at 56 ºC until a thin film was deposited. Crude multi-lamellar vesicles (MLV) were formed after the addition of 250 mM ammonium sulfate solution, including 0.5 mM gadolinium in case of Lip_{TS-GD} and $Lip_{TS-GD-CY}$ [130]. The colloidal solution was sonicated at 56 °C for 20 min using ultrasound bath sonicator (Bandelin Sonorex RK 100H, Bandelin Electronic, Berlin, Germany) at maximal energy. The sonicated liposomes were subjected to extrusion using mini-extruder (Avanti Polar Lipids, Alabaster, USA) equipped with polycarbonate membranes (200 nm and 100 nm) for 21 times at 56 °C. The small unilamellar vesicles (SUV) were then used to encapsulate Doxorubicin (DOX). SUV liposomes were 20-fold diluted in HEPES buffer at pH 8.4 and the loading of DOX has achieved at DOX: total lipids molar ratio of 0.2:1 using ammonium sulfate gradient technology [131,132]. The final theoretical load of DOX was $[C]_{DOX}$ = 1 mg/ml in $[C]_{lipids}$ = 5 mg/ml lipids. Purification of free DOX and Gd-chelate from the prepared liposomes was done using size exclusion chromatography (SEC) utilizing Sephadex-G50 column [133]. Prepared liposomes were kept in dark at +4 °C until use. Liposomes were filtered through a 0.2 µm syringe filter before using.

2.2.1.1. Conjugation of antibody to the liposomes

Immuno magnetic thermosensitive liposomes with cyanur ($Lip_{TS-GD-CY-MAB}$) were prepared by coupling MAB 1031 antibody to the surface of $Lip_{TS-GD-CY}$, an initial phospholipid / MAB 1031 molar ratio of 1000:1 was chosen, as previously optimized [134]. Liposomes containing DSPE-PEG2000-cyanur were prepared in HEPES buffer at pH 8.4. The indicated amount of MAB 1031 was dissolved in borate buffer to adjust pH at 8.8 and incubated with the grafted liposomes

at DSPE-PEG2000-cyanur : MAB 1031 molar ratio of 50:1 at room temperature for 20 h, then for 4 h under shaking at 100 rpm. The primary chlorine atom of cyanuric chloride is very reactive, which can react after minutes with the antibody. The second chlorine atom may take up to 24 hours at room temperature to form a stable bond. Whereas, the third chlorine group needs drastic reaction conditions to obtain any form of binding. The coupling step with an antibody requires the presence of proton acceptor (Figure 11). The MAB 1031 surface-modified liposomes were separated from unbound MAB 1031 bypassing the liposomes over Sepharose CL-4B and eluting with PBS pH 7.4 [75].

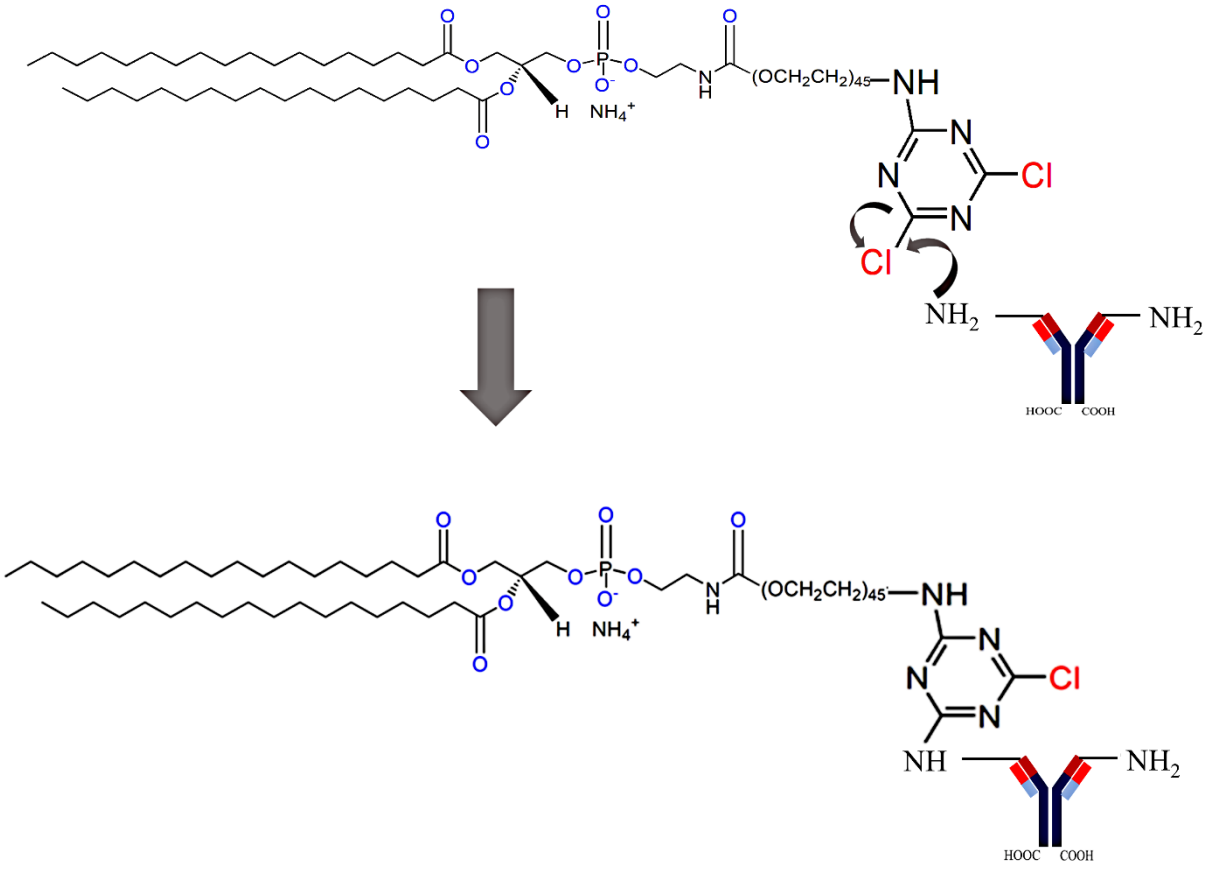

***Figure 11**: Binding of MAB-1031 antibody to DSPE-PEG2000-cyanur in the lipid bilayer of the liposome.*

Antibodies in the PEGylated or non-PEGylated liposomes can either conjugate directly to the liposomes shell or by the help provided by the PEGylation (Figure 12). One possibility to achieve conjugation of the antibody is the use of an anchor that paves the conjugation to the antibody. Here, cyanuric chloride is used and could obtain the conjugation via nucleophilic

substitution at pH 8.8. Moreover, the PEG facilitated conjugation is advantageous for anchoring the antibody to interact with different cellular receptors.

Moreover, by the use of DOX loaded immunoliposomes one can achieve an active targeting to the TNBC cells, thus offering the desired therapeutic effects of delivering DOX selectively to the tumor site with the required cumulative dose as well as minimizing its dose-related toxicity.

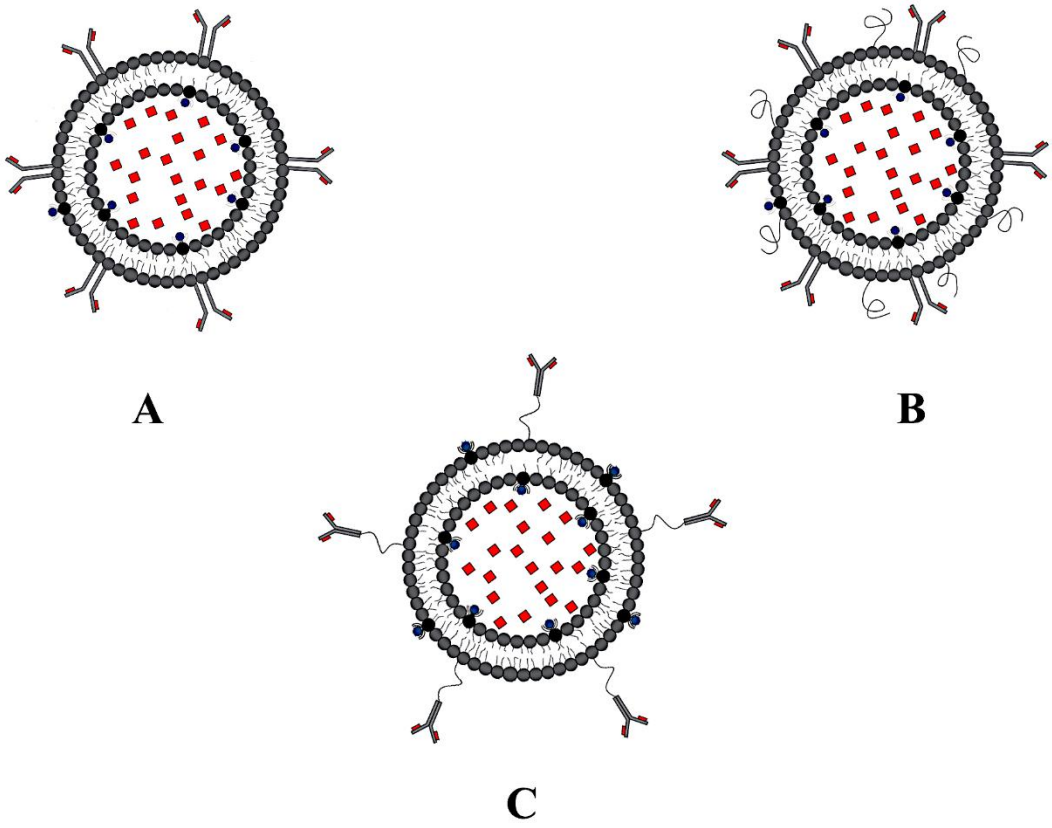

***Figure 12**: Schematic representation for the possibility of antibodies binding to the liposome. Directly on the surface of non-PEGylated liposomes (A), Directly on the surface of PEGylated liposomes (B) and antibody bound to the end of the PEG chains, by the use of PEGylated lipids with anchor molecule, e.g. DSPE-PEG2000-cyanuric (C).*

2.2.2. Dynamic light scattering

Hydrodynamic diameters of the prepared liposomes were analyzed by Dynamic Light Scattering (DLS) (Zetasizer Nano ZS, Malvern Panalytical, Herrenberg, Germany) in a clear disposable folded capillary cell (DTS1060; Malvern Instruments). DLS is equipped with a 10 mW HeNe

laser at a wavelength of 633 nm at 25 °C. The scattered light was detected at an angle of 173º. The obtained results were presented as an average value ± standard deviation of three independent preparations with three replicate measurements of each preparation for at least 10 runs. The refractive index (1.33) and viscosity (0.88 mPa.s) of water at 25 ºC were considered for analysis of the data [135].

2.2.3. Laser Doppler velocimetry

Zeta potential of the liposomes was measured by Doppler velocimetry (LDV) using the Zetasizer Nano ZS in a clear disposable folded capillary cell (DTS1060; Malvern Instruments). The scattered light is collected at an angle of 17º. Prior to the measurement, liposomes were diluted with Milli-Q water 1:100. Laser attenuation and position were automatically adjusted by the instrument depending upon the sample. The obtained results were presented as an average value ± standard deviation of three independent with three replicate measurements of each preparation for at least 10 runs.

2.2.4. DOX entrapment efficiency

Size exclusion chromatography (SEC) is utilized to separate the free DOX from the DOX-encapsulated liposomes. Prior to adding DOX-liposomes, the Sephadex-G50 column was saturated with empty liposomes of the measured formulation to prevent any remarkable loss of lipid material. The concentration of DOX in the liposomes obtained after SEC was measured using UV/Vis spectrophotometry (UV mini 1240, Shimadzu, Suzhou, China). The amount of encapsulated DOX was calculated according to equation (4) using a calibration curve of DOX in HEPES buffer [136].

$$EE\ \% = \frac{DOX\ amount\ encapsulted}{Initial\ amount\ of DOX}\ x\ 100\% \qquad \textit{Equation 4}$$

2.2.5. Atomic force microscopy

The morphology and surface structure of the liposome were visualized using atomic force microscope NanoWizard® 3 NanoScience provided by JPK Instruments (Berlin, Germany). AFM was in a soundproofed chamber during the measurements. The measurements were achieved at room temperature.

Twenty microliters of diluted liposomes in Milli-Q water (1:1000) were pipetted onto a microscope slide. Liposomes were left for 5 min to sediment and the excess liquid was aspirated leaving a thin film of aligned vesicles on the microscope slide. Commercial 1-lever tips (NSC 14 Al/BS) on a cantilever with a length of 125 µm and a resonance frequency of 140 Hz and a force constant of 5 N/m were applied. All acquisitions were performed in intermittent contact mode. Scan speed was adjusted between 0.5 and 1.5 Hz. Raw images were processed using JPKSPM software [137].

2.2.6. Transmission electronic microscopy

Surface structure and morphology of the prepared liposomes were investigated using the transmission electron microscope (TEM) JEM-3010 (JEOL, Japan) with a retractable high-resolution slow-scan CCD-Camera (Gatan MegaScan 794). The liposomes were heated at 37 °C or UHF- MRI for one hour before they were subjected to TEM visualization at 80kV. Liposomes were diluted 1:10 with 10 mM HEPES buffer (pH 7.4) before staining with uranyl acetate (2 %) for 30 minutes. Liposomes were pipetted onto 300 mesh formvar coated S160-3 copper grids (Plano GmbH Wetzlar, Germany). Equal parts of the sample and uranyl acetate were mixed together and the grid was incubated for 5 min in this solution. The mixture was examined at an accelerating voltage of 300 kV and 110 µA emission current with current densities between 50-60 pA/cm^2.

2.2.7. Differential scanning calorimetry

Differential scanning calorimetry (DSC) measures the heat capacity depending on the temperature. DSC measurements were performed to determine the phase transition transforming

from the liquid condensed to liquid expanded phase of phospholipid mixtures of the prepared liposomes.

The DSC measurements for the $Lip_{TS\text{-}GD}$ were performed on MicroCal VP-DSC. MicrocalInc., Northampton, MA, USA, scanned temperature range was 20 and 60 °C, the heating rate was 60 °C per hour. The reference cells were filled with buffer, and the buffer-buffer baseline was deducted from the thermograms of the liposomes. MicroCal Origin 8.0 software was utilized to analyze the DSC scans, the peak maximum was set as the transition temperature (T_m) [138]. The DSC measurements for $Lip_{TS\text{-}GD\text{-}CY\text{-}MAB}$ were performed on DSC-7 (Perkin Elmer, Rodgau, Germany). The scanned temperature range was between 35 to 50 °C, the heating rate was 6 °C per hour. The reference cells were filled with HEPES buffer, and the buffer-buffer baseline was subtracted from the thermograms of the liposomes. DSC scans were analyzed using Pyris software, peak maximum was set as the transition temperature (T_m).

2.2.8. Drug release

To determine DOX release from the nanocarrier system, cumulative release of DOX from the $Lip_{TS\text{-}GD}$ / $Lip_{TS\text{-}GD\text{-}CY\text{-}MAB}$ were performed at 37, 38, 39 and 40 °C at different time intervals (up to 60 min). 2 ml of DOX-$Lip_{TS\text{-}GD}$ / DOX-$Lip_{TS\text{-}GD\ CY\text{-}MAB}$ were suspended in 1 ml HEPES (pH = 7.4), transferred into a dialysis bag (MWCO = 6,000-8,000) and incubated in 20 ml of HEPES pre-heated to the aforementioned temperatures with stirring speed of 100 rpm. 1 ml from the outer HEPES buffer was collected at selected time points and replaced with 1 ml of fresh HEPES. To determine the amount of DOX released at different time points, collected samples were analyzed by UV/Vis spectrophotometry (UV mini 1240, Shimadzu, Suzhou, China). The amount of DOX released was calculated according to equation 5 using a calibration curve of DOX in HEPES buffer.

$$Cumulative\ DOX\ release\ \% = \frac{DOX\ released}{Initial\ amount\ of DOX}\ x\ 100\% \qquad \textit{Equation 5}$$

2.2.9. Ultra high field magnetic resonance imaging

The ultra high field magnetic resonance imaging (UHF-MRI) (Figure 13) measurements were performed on a 7 Tesla UHF-MRI (Bruker BioSpin GmbH, Rheinstetten, Germany) with a birdcage coil by applying a diffusion sequence for all images and measurements. The quantification of the T1 times was performed with an inversion recovery sequence (TR: 7000 ms, TE: 7.9 ms) and different TI (500, 1000, 1500, 2000, 25000) ms. Syngo's Dynamic Analysis application created T1 maps before and after warming by a water bath (Bruker Biospin MRI GmbH, Circulating Thermostat C-10-P5/U230/50-60) from the acquired images. The change in temperature after UHF-MRI treatment was monitored by infrared thermometer (IR) Scantemp 385 (Carl Roth, Karlsruhe, Germany).

***Figure 13**: Ultra high field-magnetic resonance imaging (UHF-MRI); 7 Tesla.*

(https://www.uni-marburg.de/de/fb20/forschung/corefacilities/7t-kleintier-mrt)

2.2.10. Cell conditions

Two cell lines were utilized in this project. Both cells are Triple-negative breast cancer cells i) MDA-MB-231-ctrl with high endogenous ADAM8 expression and ii) MDA-MB-231-rna with ADAM8 knockdown. MDA-MB-231-ctrl cells were obtained from ATCC (American Type

Cell Culture, Manassas, USA). MDA-MB-231-rna (ADAM8 knockdown) cells were obtained from Prof. Dr. Jörg-Walter Bartsch (Neurosurgery, University Hospital Marburg) [139]. Both cells were cultivated in Dulbecco's Modified Eagle Medium (DMEM) (Biochrom, Berlin, Germany) at 37 ºC and 7 % CO_2 under humid conditions. The media were boosted with 10 % fetal calf serum (PAA, Cölbe, Germany).

2.2.11. Cytotoxicity studies upon hyperthermia

MDA-MB-231-ctrl cells were passaged when they reach about 95 % confluency. The cells are adherent cells, from these adherent cells the old medium was removed carefully, then 1ml Trypsin/EDTA was added, followed by incubation for 5 min. Trypsin was neutralized after adding 10 ml medium. The suspended cells were filled in a 15 ml sterile tube and centrifuged at 9000 g for 5 min. The medium was aspirated and replaced with 1 ml fresh medium. Cells with the 1 ml fresh medium were transferred to a sterile petri dish with 9 ml fresh medium. At the time of passage, MDA-MB-231-ctrl cells were seeded into 96-well plates (NUNC, Thermo ScientificTM, Germany) at a cell density of 10,000 cells/cm^2.

2.2.11.1. Thermal therapy in the incubator

MDA-MB-231-ctrl cells were seeded into 96-well plates (NUNC, Thermo Scientific^{TM}, Dreieich, Germany) at a cell density of 10,000 cells/well and kept at 37 °C for 24 h. After 24 h, the cells were incubated with DOX-liposomes for 3 or 3.5 hours at 37 °C, followed by thermal treatment either at 38 or 39 or 40 ºC. Different thermal therapy times of 30 and 60 min for each temperature were applied in the case of $Lip_{TS\text{-}GD}$.

In the case of $Lip_{TS\text{-}GD\text{-}CY}$ and $Lip_{TS\text{-}GD\text{-}CY\text{-}MAB,}$ cells were incubated with DOX-liposomes (DOX concentration = 100 µg/ml) for 3 hours at 37 °C, followed by thermal treatment either at 38 or 39 or 40 ºC for 60 min. The medium was replaced with fresh medium and cells were further incubated for 24 h. Control untreated cells were similarly incubated at the same temperatures and incubation times.

2.2.11.2. Thermal therapy under magnetic field

MDA-MB-231-ctrl cells were seeded in 2 well-Chamber slides at a cellular density of 20,000 cells/well. $Lip_{TS\text{-}GD}$ liposomes were incubated with the cells for 3 or 3.5 hours at 37 °C followed by cellular exposure to UHF-MRI field for 60 or 30 minutes, respectively.
In the case of $Lip_{TS\text{-}GD\text{-}CY}$ and $Lip_{TS\text{-}GD\text{-}CY\text{-}MAB}$, liposomes were incubated for 3 hours with DOX final concentration of 100 µg/ml at 37 °C followed by cellular exposure to UHF-MRI field for 60 min [56,140]. The cells were further incubated for 24 hours. Control untreated cells were similarly incubated at the same temperatures, incubation times and UHF-MRI conditions.
To simulate physiological temperature and prevent hypothermia due to room temperature during UHF-MRI exposure, chamber slides were kept on temperature pads, that were contacted with heated water tubes to keep 37 °C as an initial point (Figure 14).

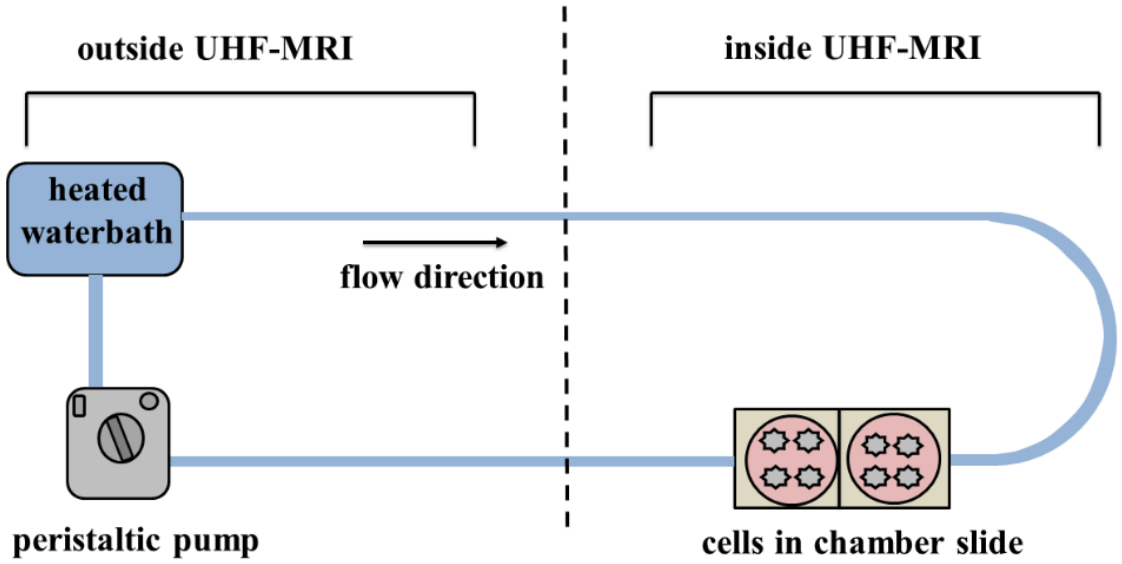

***Figure 14**: Schematic representation of an adjusted water bath system to keep 37 °C as an initial temperature inside UHF-MRI to prevent hypothermia.*

2.2.11.3. MTT cell viability assay

Cytotoxicity after thermal therapy was determined by measurement of cell viability based on the cellular redox potential as previously reported [141]. Briefly, the medium was aspirated and 3-(4,5-dimethylthiazol-2-yl)-2,5-diphenyltetrazolium bromide (MTT) reagent was subsequently added. Cells were further incubated for 4 h in the dark. Actively respiring cells

convert the water-soluble MTT to an insoluble purple formazan. The formazan was then solubilized in DMSO and its concentration was determined at 570 nm using a plate reader (FLUOstar, BMG, Germany). Untreated cells were used as a control representing 100 % viability [142,143]. Results were expressed as mean ± standard deviation (SD).
MDA-MB-231-rna cells were non-stable against the temperature, that's why no viability assay was determined on MDA-MB-231-rna cells.

2.2.12. Cellular uptake evaluation

At the time of passage, MDA-MB-231-ctrl cells were grown at a cell density of $1x10^5$ cells/cm^2 on 18 x 18 mm sterile cover glasses at 37 °C for 18 h. The cells were incubated with $Lip_{TS\text{-}GD}$ liposomes for 3 h at 37 °C followed by thermal therapy at 40 °C or cellular exposure to UHF-MRI field for 60 min. In another set of experiments, cells were incubated with $Lip_{TS\text{-}GD}$ liposomes for 4 h at 37 °C without exposure to UHF-MRI field. The medium was then aspirated and cells were washed with Ca^{2+} and Mg^{2+} containing PBS buffer. The cells were fixed with 4 % paraformaldehyde for 10 min at room temperature. The cell nuclei were stained by addition of 4',6-diamidino-2-phenylindole (DAPI) at 3.63 mM for 2 min [144]. The cells were washed again with the buffer, and the cover glass was transferred onto glass slides for imaging with a confocal laser scanning microscope (Carl Zeiss Microscopy GmbH, Jena, Germany).

2.2.13. Pathway studies

MDA-MB-231-ctrl cells were seeded into 96-well plates (NUNC, Thermo Scientific™, Dreieich, Germany) at a cell density of 10,000 cells/well and kept at 37 °C for 24 h. Cells were incubated with Filipin III or Chlorpromazine (10 µg/ml) for 1 h, then treated with DOX-$Lip_{TS\text{-}GD\text{-}CY}$ or DOX-$Lip_{TS\text{-}GD\text{-}CY\text{-}MAB}$ for 3 h at 37 °C followed by UHF-MRI for 1 h using the same protocol explained earlier (2.2.11.2). The medium was replaced by fresh medium and the cells were incubated for 24 h, MTT assay was used to determine the cell viability. As a blank, cells were treated with DOX-$Lip_{TS\text{-}GD}$ or DOX-$Lip_{TS\text{-}GD\text{-}MAB}$ at 37 °C for 4 h without inhibition.

2.2.14. Mechanism of endosomal escape by fluorescence microscopy

To evaluate the endosomal escape of the nanocarrier system into the cells. MDA-MB-231 cells (ctrl / rna) were seeded at the seeding density of 1 x 10^5 cells per well in a 12-well cell culture plate on glass coverslips. After overnight incubation, the medium was replaced with fresh medium and incubated with the NBD labeled liposomes ($Lip_{TS\text{-}GD\text{-}CY}$ or $Lip_{TS\text{-}GD\text{–}CY\text{-}MAB}$). After 4 h of cell incubation, 100 nM of Lyso Tracker® red DND-99 was added to the cells and further incubated for 30 min at 37 °C under humid conditions. Thereafter, DAPI staining was performed as described earlier (2.2.12). The coverslips were placed on a clear glass slide containing a drop of mounting medium (FluorSave™, Calbiochem, San Diego, USA) before being analyzed under a fluorescence microscope (CKX-53 Olympus, USA). Equipped with fluorescence detection filters for LysoTracker® red (ex. 577 nm - em.590 nm) and DAPI (ex.385 nm - em.470 nm).

2.2.15. In vitro evaluation of ADAM8 targeting by immunoliposomes

To evaluate the targeting effect of immuno/non-immuno liposomes, MDA-MB-231 cells (ctrl / rna) cells were used. We used a monoclonal mouse antibody (MAB 1031) (R & D Systems, Minneapolis, MN, USA) that detects the aa 201 - 497 epitope of the human ADAM8 ectodomain, i.e. the section of the protein-membrane that protrudes away from the cell wall into the extracellular space.

2.2.15.1. Washing method

MDA-MB-231 (ctrl / rna) were seeded at a density of 1x10^5 cells/cm^2. After overnight incubation cells were incubated for 2 h with NBD liposomes at +4 °C to avoid any endocytotic events [75]. Afterward, the medium containing liposomes was aspirated and cells were washed with activity buffer (20 mM Tris-Cl pH 8, 10 mM $CaCl_2$, 1 µM $ZnCl_2$, 0.0006 % Brij®) for 5 times, then the activity buffer was aspirated and cells were washed with PBS buffer containing Ca^{2+} and Mg^{2+}. The cells were fixed with 4 % paraformaldehyde for 10 min, and DAPI staining was performed as described earlier (2.2.12) following by washing with PBS buffer.

The cover glass was transferred onto glass slides for imaging with a confocal laser scanning microscope (Carl Zeiss Microscopy, GmbH, Jena, Germany) or fluorescence microscope (CKX-53 Olympus, USA) using GFP filters (ex.505 nm - and em.530 nm). $Lip_{TS\text{-}GD\text{-}CY\text{-}MAB}$ binding ability to MD-MB-231-ctrl cells was compared to $Lip_{TS\text{-}GD\text{-}CY}$.
Additionally, UHF-MRI images were acquired after washing with both $Lip_{TS\text{-}GD\text{-}CY}$ and $Lip_{TS\text{-}GD\text{-}CY\text{-}MAB}$, to confirm UHF-MRI activity of the liposomes after cell binding and mean gray value was measured.

2.2.15.2. Circulation method

To portray *in vivo* like conditions, a model circulation system was established (Figure 15), using a pulsed peristaltic pump (PD5001, Heidolph Instruments, Schwabach, Germany). Sterilized silicone tubes with a diameter of 4.0 mm were used (similar to the size of a middle-sized vein) and their ends were attached to a well-designed chamber that can accommodate three cover glasses at the same time. Briefly, MDA-MB-231 (ctrl / rna) cells were seeded at the seeding density of 1×10^5 cells per well in a 12-well cell culture plate containing glass coverslips. After overnight incubation, coverslips were placed in the chamber and NBD labeled liposomes ($Lip_{TS\text{-}GD\text{-}CY}$ or $Lip_{TS\text{-}GD\text{-}CY\text{-}MAB}$) were allowed to circulate for 30 min. The velocity of circulation was set at 2 cm/s to avoid the risk of washing off the cells from the coverslips. The binding efficiency of NBD labeled liposomes with the cell membrane was analyzed using a fluorescence microscope (CKX-53 Olympus, USA) using GFP filters (ex.505 nm - and em.530 nm) and for the quantitative determination the coverslips were dipped in 1 % Triton-X-100® and fluorescence was measured using a microplate reader FluorStar Optima (BMG Labtech, Ortenberg, Germany) at excitation and emission wavelength of 408 nm and 640 nm, respectively.

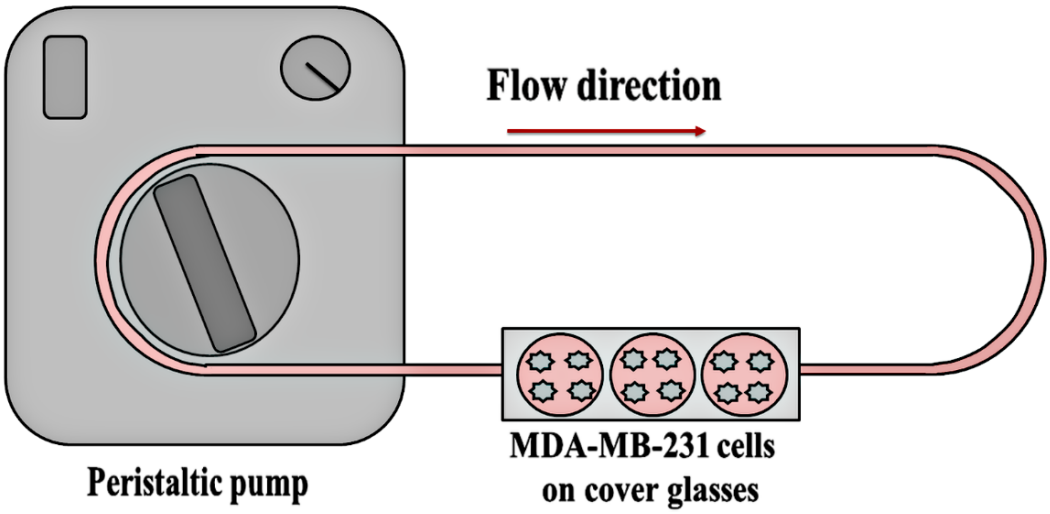

***Figure 15**: Schematic representation of the binding circulation model.*

2.2.16. Hemocompatibility studies

2.2.16.1. Activated partial thromboplastin time

Activated partial thromboplastin time (aPTT) was used to determine the effect of the prepared liposomes on the coagulation time. Fresh whole blood samples were taken into citrate tubes. In order to separate the plasma fraction, the blood samples were subjected to centrifugation at 1500 g for 10 min. Activated partial thromboplastin time (aPTT) was determined using a Coatron M1 coagulation analyzer (Teco, Neufahrn, Germany) using aPTT-S Kit (TEClot) according to the manufacturer's instructions as previously mentioned with some modifications [143]. Briefly, 25 µL of plasma was mixed with 25 µL of the sample preparation. 50 µL of aPTT reagent was mixed with the sample to activate coagulation factors followed by the addition of 50 µl previously warmed calcium chloride solution (0.025 M). Coagulation was confirmed spectrophotometrically and the time was recorded in seconds.

2.2.16.2. Ex vivo Hemolysis Assay

Erythrocytes isolated from fresh human blood were used to determine the hemolytic potential of the prepared liposomes on blood [145]. Freshly isolated human erythrocytes were obtained

as previously described [143]. Briefly, fresh whole blood was withdrawn into EDTA containing tubes followed by centrifugation at 1500 g for 10 min. The obtained red blood cell pellet was subjected to three washing steps and diluted to 1:50 with NaCl. The diluted mixture of erythrocytes was incubated with various sample preparations for 1 h at 37 ºC in V-bottom microtiter plates in an orbital shaker KS4000 IC (IKA Werke, Staufen, Germany). The plates were then centrifuged and the collected supernatants were measured at 540 nm using FLUOstar Optima (BMG Labtech, Ortenberg, Germany) microplate reader. Parallel measurements of PBS buffer (pH 7.4) and 1 % Triton X-100® were used as controls and the absorbance values of Triton X-100® were considered as 100 % hemolysis.

2.2.17. Chorioallantoic membrane model

Fertilized eggs were obtained from Mastkükenbrüterei Bormann (Rheda-Wiedenbrück, Germany). The eggs were disinfected using 70 % ethanol and incubated in an egg hatching incubator at 37 °C and 65 % relative humidity. The incubator is equipped with an automatic rotor every 6 h to prevent the attachment of the developing embryo at the eggshell. The intact chorioallantoic membrane model (CAM) was prepared as reported elsewhere [146,147]. Briefly, on day 4 of embryo development (EDD 4), a hole of about 3 cm was made on the apical side of the egg using a pneumatic egg puncher (Schuett biotech, Göttingen, Germany) at a pressure of about 2-3 bars to expose the CAM surface. The exposed surface was then covered with a small petri dish and the egg was further incubated. On day 11 of embryo development (EDD 11) 15 eggs for each of: free DOX, DOX-Lip$_{TS\text{-}GD\text{-}CY}$ or DOX-Lip$_{TS\text{-}GD\text{-}CY\text{-}MAB}$ were injected intravenously *in ovo* under a stereomicroscope (Stemi 2000-C, Carl Zeiss, Göttingen, Germany). All instruments were disinfected with 70 % ethanol before use. After the treatment, the eggs were placed back into the incubator and the agility of embryo, the heartbeat and the state of vessel development were monitored and recorded daily until EDD 16.

Additionally, Lip$_{TS\text{-}GD\text{-}CY\text{-}MAB}$ was injected intravenously into the chick embryo vasculature and images were acquired using UHF-MRI (Bruker, Model Clinscan 70/30) to confirm the diagnostic potential of the prepared liposomes.

2.2.18. Statistical analysis

All experiments were performed in triplicates and values are shown as mean ± standard deviation unless otherwise stated. A two-tailed Student´s t-test was performed to identify statistically significant differences. Probability values of $p < 0.05$ were considered significant. In all analyses, statistical differences are denoted as [*] $p < 0.05$, [**] $p < 0.01$, [***] $p < 0.001$.

3. Results and discussion

3.1. Hydrodynamic diameter and Zeta potential

Dynamic light scattering was used to investigate the size of the prepared liposomes. Lip_{TS} obtained a size of 120.43 ± 1.91 nm. The Particle size increased upon the incorporation of Gd-chelate within $Lip_{TS\text{-}GD}$ and $Lip_{TS\text{-}GD\text{-}CY}$ lipid bilayer to 134.53 ± 17.45 nm and 126.90 ± 12.56 nm, respectively. The minor increase in size is ascribed to the size of Gd-chelate and its alignment within the lipid bilayer. The conjugation of MAB 1031 to $Lip_{TS\text{-}GD\text{-}CY}$ to form $Lip_{TS\text{-}GD\text{-}CY\text{-}MAB}$ resulted in an increase of the particle size to reach 167.98 ± 11.53 nm, which could be accounted to the size of MAB 1031 [148] or MAB-MAB dimeric formation. Further investigation of the polydispersity index (PDI) was carried out, a monomodal size distribution was observed in the case of Lip_{TS}, $Lip_{TS\text{-}GD}$ and $Lip_{TS\text{-}GD\text{-}CY}$ with a recorded PDI of 0.14, 0.16 and 0.16, respectively (Table 1). The minor increase in the PDI after the incorporation of Gd-chelate is ascribed to the protruding Gd-chelate moieties on the liposomal surface, where Gd-chelate can be presented either as core-encapsulated, surface-conjugate or dually presented in the core and on the surface of the liposomes [149]. Multimodal size distribution was observed in the case of $Lip_{TS\text{-}GD\text{-}CY\text{-}MAB}$ (PDI: 0.23), the multimodal distribution can be attributed to either MAB 10131 conjugation or to the formation of dimeric MAB-MAB.

Laser Doppler velocimetry was used to measure Zeta potential of the formulated liposomes (Table 1), Lip_{TS} measured a Zeta potential of – 6.92 ± 2.64 mV, whereas the negative Zeta potential has increased in case of $Lip_{TS\text{-}GD}$ to – 13.96 ± 5.09 mV. The increased in negative Zeta potential is an indication of the incorporation of the negatively charged Gd-chelate complex $[GdDTPA]^{2-}$. These findings correspond with previously published results by Bartacek *et al.* [150]. In the case of $Lip_{TS\text{-}GD\text{-}CY}$, the Zeta potential measured – 50.66 ± 7.95 mV, A small variation to the charge was observed after the coupling of MAB antibody ($Lip_{TS\text{-}GD\text{-}CY\text{-}MAB}$), the Zeta potential was -43.93 ± 3.38 mV, which can be explained by the acquired charge of the antibody, these findings corresponded with previously published results [148,151].

3.2. Encapsulation efficiency

DOX was encapsulated into the liposomal payload using a remote loading method, the theoretical load of DOX was $[C]_{DOX}$=1 mg/ml. Remote loading method is using a driving force for loading amphipathic weak bases such as DOX into liposomes, it was firstly reported by

Bahrenholz and his working group [45]. They have used an ammonium sulfate gradient, which facilitates the encapsulation of DOX into liposomes. DOX was reported to be exclusively encapsulated into the liposomal core by several authors [152,132].

DOX encapsulation efficiency was 92.3 % in the case of Lip_{TS}. After the incorporation of Gd-chelate the encapsulation efficiency decreased to 84.07 %. Pitchaimani *et al*. has reported that incorporating Gd-chelate raises concerns regarding drug encapsulation efficiency [153]. Nevertheless, our liposomes showed minimal retardation effect on DOX encapsulation efficiency into the liposomal core. In the case of $Lip_{TS\text{-}GD\text{-}CY}$ the encapsulation efficiency was 86.09 % (Table 1). After the addition of MAB antibody to the liposomes, no significant difference in the encapsulation efficiency was observed, where the encapsulation efficiency was 86.01 %. It is noteworthy to mention that MAB was conjugated to the liposomes after the encapsulation of DOX into the liposomal payload, which explains the unaffected DOX encapsulation efficiency.

3.3. Atomic force microscopy

Atomic force microscopy was used to measure and visualize the morphological aspects of the prepared liposomes and help to better understand their surface characteristics. The average diameter of the liposomes measured on the AFM images corresponded well to the hydrodynamic diameter measured by dynamic light scattering. However, a slight increase was measured on the average diameter in AFM images (Table 1) that can be explained by the adhesion of the liposomes on the mica surface. AFM images showed mostly uniform round-shaped vesicles and segregated patterns of the liposomes at 37 °C. The size of the liposomes was between 130 and 184 nm at 37 °C (Figure 16 A, B, D). An increase in liposomal size can be observed in the AFM images after the incorporation of Gd-chelate (Figure 16 B, D). The temperature stability of the liposomes was observed under AFM after hyperthermia application using UHF-MRI. The liposomes were burst and showed disrupted lipid film on the mica surface (Figure 16 C, E). For the assessment of the disruption of the liposomes, the amplitude model was utilized. The highest measured nm in all liposomes formulation was between 10 to 12 nm at 37 °C, whereas after UHF-MRI exposure in the presence of Gd-chelate it dropped down to be between 4 to 5 nm, which indicates the disruption of the liposomes and formation the flat lipid film. The amplitude model mainly gives an insight into the degree of surface roughness.

Surface roughness is defined as the calculated average of the height of the surface asperities, above a hypothetical, smooth plane, i.e. mica surface [154]. The decrease in surface roughness after hyperthermia corresponds with the change in the asperities and amplitude of the liposomes. The decrease in the amplitude suggests that liposomal integrity has been disrupted to a certain degree.

Thus indicate that after hyperthermia liposomes have lost their structure, which is clearly shown by (Figure 16 C, F). These findings confirm the thermosensitive effects of the liposomes after UHF-MRI exposure.

***Table 1**: Physiochemical properties of the liposomes. Particle size, polydispersity index (PDI), Zeta potential and encapsulation efficiency (EE) of Lip_{TS}, $Lip_{TS\text{-}GD}$, $Lip_{TS\text{-}GD\text{-}CY,}$ and $Lip_{TS\text{-}GD\text{-}CY\text{-}MAB}$. As mean ± standard deviation of three independent measurements (n=3).*

Liposomes	**Particle size [nm]**		**Zeta potential**	**EE [%]**	**AFM ± SD**
	DLS±SD	**PDI**	**± SD [mV]**		**[nm]**
Lip_{TS}	120.43 ± 1.91	0.14 ± 0.02	-6.92 ± 2.64	92.3 ± 2.82	130.33 ± 21.55
$Lip_{TS\text{-}GD}$	134.53 ± 17.45	0.16 ± 0.06	-13.96 ± 5.09	84.07 ± 2.90	154.67 ± 15.83
$Lip_{TS\text{-}GD\text{-}CY}$	126.90 ± 12.56	0.16 ± 0.05	-50.66 ± 7.95	86.09 ± 3.20	138.66 ± 34.89
$Lip_{TS\text{-}GD\text{-}CY\text{-}MAB}$	167.98 ± 11.53	0.23 ± 0.01	-43.93 ± 3.38	86.01 ± 3.02	184.16 ± 47.43

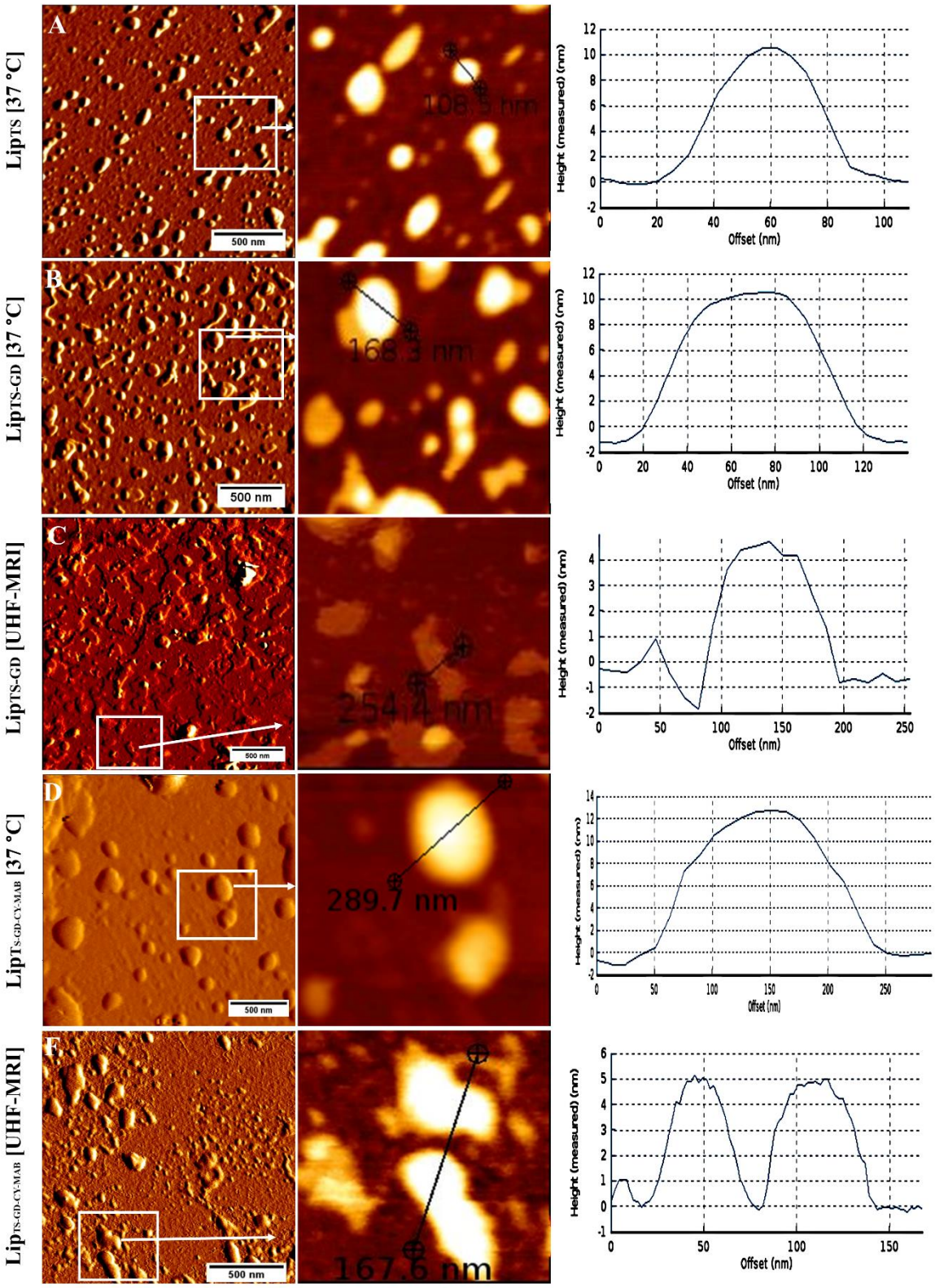

***Figure 16**: Visualization of the liposomes using AFM. Lip_{TS} incubated at 37 °C (A), $Lip_{TS\text{-}GD}$ at 37 °C (B), $Lip_{TS\text{-}GD}$ after UHF-MRI exposure (C), $Lip_{TS\text{-}GD\text{-}CY\text{-}MAB}$ at 37 °C (D) and $Lip_{TS\text{-}GD\text{-}CY\text{-}MAB}$ after UHF-MRI exposure. Images on the right side show a cross-sectional profile of the identified lines of addressed sections in AFM images for addressing surface roughness.*

3.4. Transmission electron microscopy

Transmission electron microscopy (TEM) analysis was performed to further inspect morphological aspects, confirm the structure of the liposome as well as to investigate the exact deposition of the Gd-chelate within the liposomes. Lip_{TS} (A), $Lip_{TS\text{-}GD}$ (B), and $Lip_{TS\text{-}GD\text{-}CY\text{-}MAB}$ (D) showed round spherical vesicles at 37 °C.

Lip_{TS} appears under TEM without any dark contrast, whereas in the case of $Lip_{TS\text{-}GD}$ and $Lip_{TS\text{-}GD\text{-}CY\text{-}MAB}$, a clear deposition of Gd is showing as dark contrast. Liposomes with Gd-chelate displayed good-segregated vesicles and no Gd-chelate was observed outside the liposomal domain, indicating that Gd-chelate was well encapsulated within the liposomes [149]. As shown in (Figure17 B, D). Gd is shown to be highly encapsulated in the core of the liposomes, as the lipid bilayer incorporated chelate is holding the Gd.

The temperature dependent stability of the vesicles in the presence of Gd-chelate was observed after hyperthermia application using UHF-MRI, where vesicular deformation of the liposomes was evident and Gd-chelate was released (Figure 17 C, E). This confirms the results indicated by Hardiansyah *et al*. [155] in which he reported that magnetically induced hyperthermia triggers disruption of the lipid bilayer, hence facilitate the release of the encapsulated moieties.

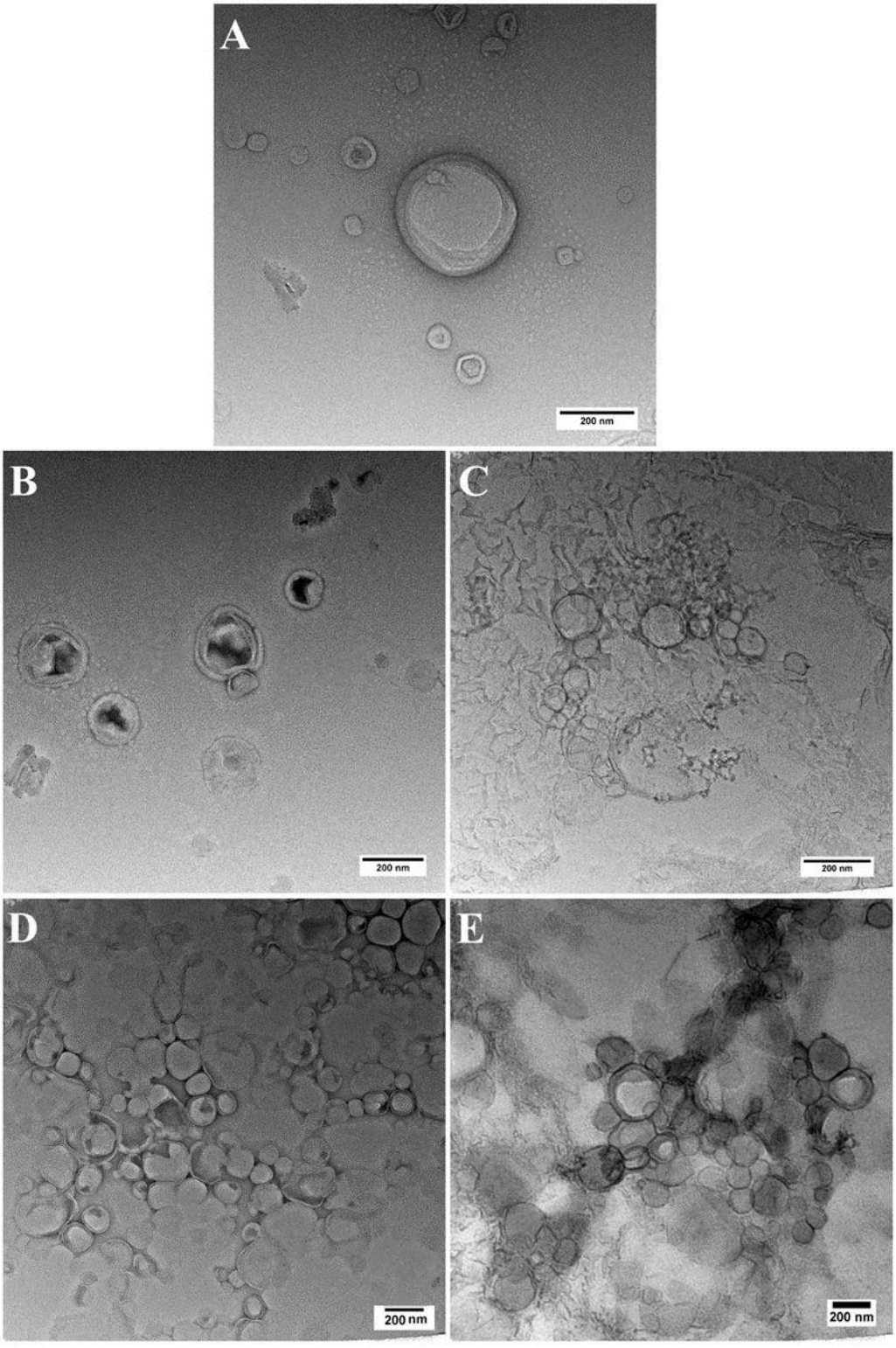

***Figure 17**: Temperature-dependent transmission electron micrographs of Lip_{TS} (A), $Lip_{TS\text{-}GD}$ (B) and $Lip_{TS\text{-}GD\text{-}CY\text{-}MAB}$ (D) incubated at 37 °C manifested well-segregated vesicular structures and well-encapsulated of Gd in the liposomes. $Lip_{TS\text{-}GD}$ after UHF-MRI exposure (C) and $Lip_{TS\text{-}GD\text{-}CY\text{-}MAB}$ after UHF-MRI exposure (E) demonstrated the release of Gd-chelate payload after disruption of the lipid bilayer of $Lip_{TS\text{-}GD}$ and $Lip_{TS\text{-}GD\text{-}CY\text{-}MAB}$.*

3.5. Differential scanning calorimetry

Differential scanning calorimetry (DSC) experiments were carried out to determine the required temperature for the transformation from the liquid condensed to liquid expanded of the prepared liposomes. Thermosensitive properties of the liposomes and their phase transition temperature were depended on the subtle blend of the lipids. The phase transition temperature was determined for both $Lip_{TS\text{-}GD}$ and $Lip_{TS\text{-}GD\text{-}CY\text{-}MAB}$. The first change in phase transition (onset temperature) for $Lip_{TS\text{-}GD}$ was detected at about 38 °C and reached a maximum value of about 42 °C (Figure 19 A). In the case of $Lip_{TS\text{-}GD\text{-}CY\text{-}MAB}$, the phase transition was detected at about 38 °C and reached its maximum value at about 39 °C (Figure 19 B). $Lip_{TS\text{-}GD}$ and $Lip_{TS\text{-}GD\text{-}CY\text{-}MAB}$ have almost the same onset thermal point, whereas $Lip_{TS\text{-}GD\text{-}CY\text{-}MAB}$ showed lower temperature for the maximum value.

The observed decrease in the phase transition temperature in $Lip_{TS\text{-}GD\text{-}CY\text{-}MAB}$ is mainly related to the increased cholesterol molar ratio in the formulation. Cholesterol can be integrated within the phospholipids membrane. It reduces the enthalpy of the phase transition of the phospholipids membrane or at higher concentrations, it can eliminate it [123]. It fluidizes the phospholipid membrane in the liquid condensed by inhibition of the align configuration of acyl chains [60] (Figure 18). Therefore, liposomes with high cholesterol concentration may lose their thermosensitive properties. It increases the packing density of phospholipids in the liquid expanded phase. Consequently, membrane permeability is altered depending on the ration and concentration of cholesterol [60,156].

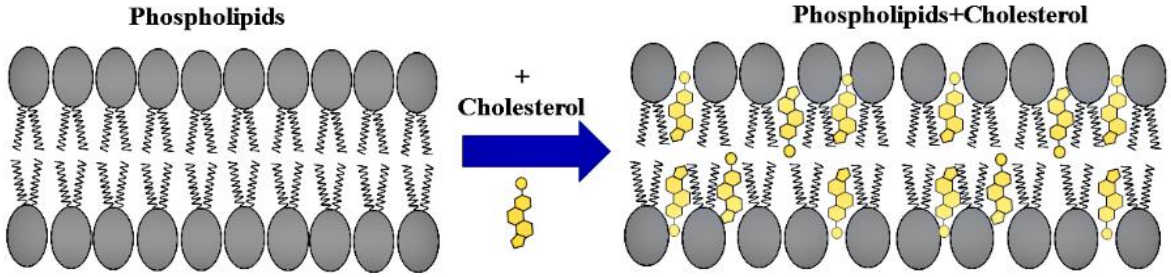

Figure 18: *Influence of cholesterol on the liquid condensed phase in the phospholipid membrane. Cholesterol between the acyl group causes fluidization of the lipid membrane.*

Many thermosensitive liposomal formulations reported in the literature showed thermosensitivity in the range of 43-45 °C [157,56]. Needham *et.al* has previously reported liposomes with mild thermosensitivity that showed a phase transition temperature of 39-40 °C [57]. Our prepared liposomes showed high thermosensitivity with low phase transition temperature starting at about 38 °C, indicating rapid thermosensitive properties with high thermosensitivity. The required temperature for our nanocarrier system can be achieved under UHF-MRI exposure. This facilitates the beneficial aspects of hyperthermia treatment without harming neighboring tissues.

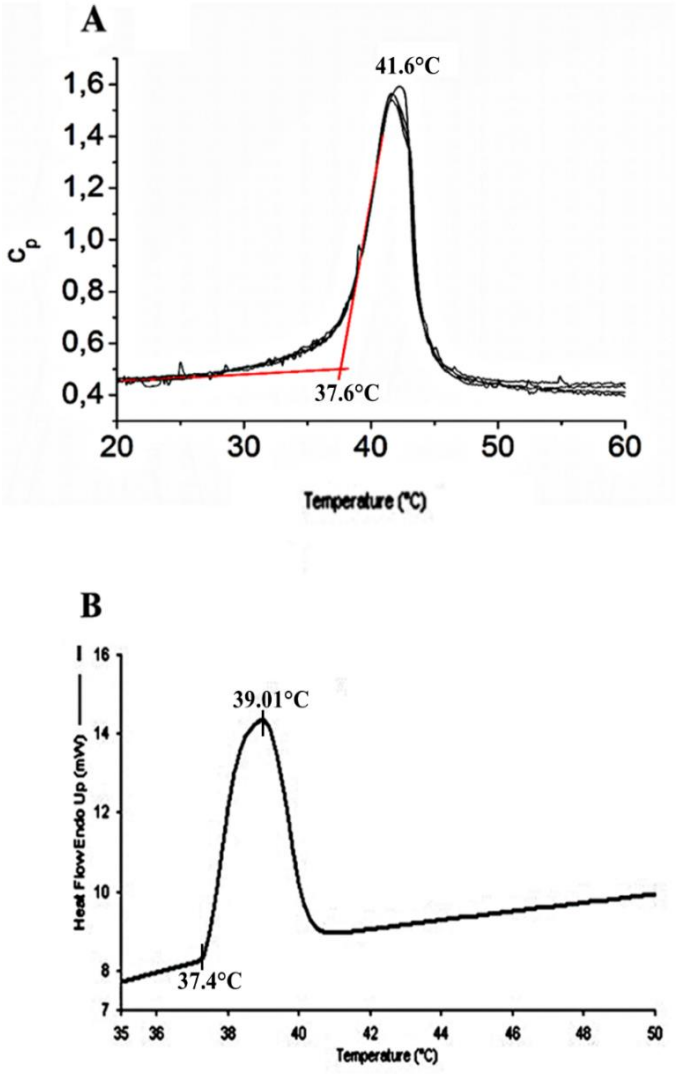

***Figure 19**: Differential scanning calorimetry thermogram of Lip$_{TS\text{-}GD}$ (A) and Lip$_{TS\text{-}GD\text{-}CY\text{-}MAB}$. Cells filled with buffer were utilized as references.*

3.6. In vitro drug release

As a proof of concept for the thermosensitive properties of the prepared liposomes, the DOX release profile from our liposomes upon hyperthermia was obtained. An active response of the liposomes upon low hyperthermia was observed, which indicates that the low hyperthermia subjected the liposomes to a phase transition from liquid condensed to liquid expanded phase [65,158,159].

Release profile from $Lip_{TS\text{-}GD}$ and $Lip_{TS\text{-}GD\text{-}CY\text{-}MAB}$ was performed at 37, 38, 39 and 40 °C (Figure 20 A, B) for different time intervals using the dialysis bag technique. No significant release was observed at 37 °C in $Lip_{TS\text{-}GD}$ and $Lip_{TS\text{-}GD\text{-}CY\text{-}MAB}$, which indicate the liposomes were mostly intact at normal physiological temperatures. However, DOX release started at 38 °C.

The maximum amount of DOX was released (about 82 %) from $Lip_{TS\text{-}GD}$ after one hour at 40 °C. Moreover, 60 % of DOX was released after one hour of temperature treatment at 39 °C. DOX release profile showed a slow blunt increase to reach its maximum release capability, which is ascribed to the low hyperthermia treatment. As reported previously by Gaber *et al.* [53,57] their thermosensitive liposomes took 30 min to release ~40 % of its contents. de Smet *et al*. previously reported DOX release from low thermosensitive liposomes with a very sharp release of about 90 % after 5 min of treatment at 42 °C [65]. Thus indicating that high-temperature treatment exceeding 40 °C can result in higher sharpness regarding thermosensitive liposomes content release.

A release profile for $Lip_{TS\text{-}GD\text{-}CY\text{-}MAB}$ was obtained (Figure 20 B) following the same parameters as $Lip_{TS\text{-}GD}$ (Figure 20 A). Results were comparable with those obtained from $Lip_{TS\text{-}GD}$ with a slight observed increase. The release reaching its maximum of about 78 % and 88 % after one hour of treatment at 39 and 40 °C, respectively. This increase can be ascribed to higher cholesterol content in $Lip_{TS\text{-}GD\text{-}CY\text{-}MAB}$ as the phase transition temperature is decreased, therefore, the disruption of the liposomal bilayer is faster and subsequently, the cargo release is faster.

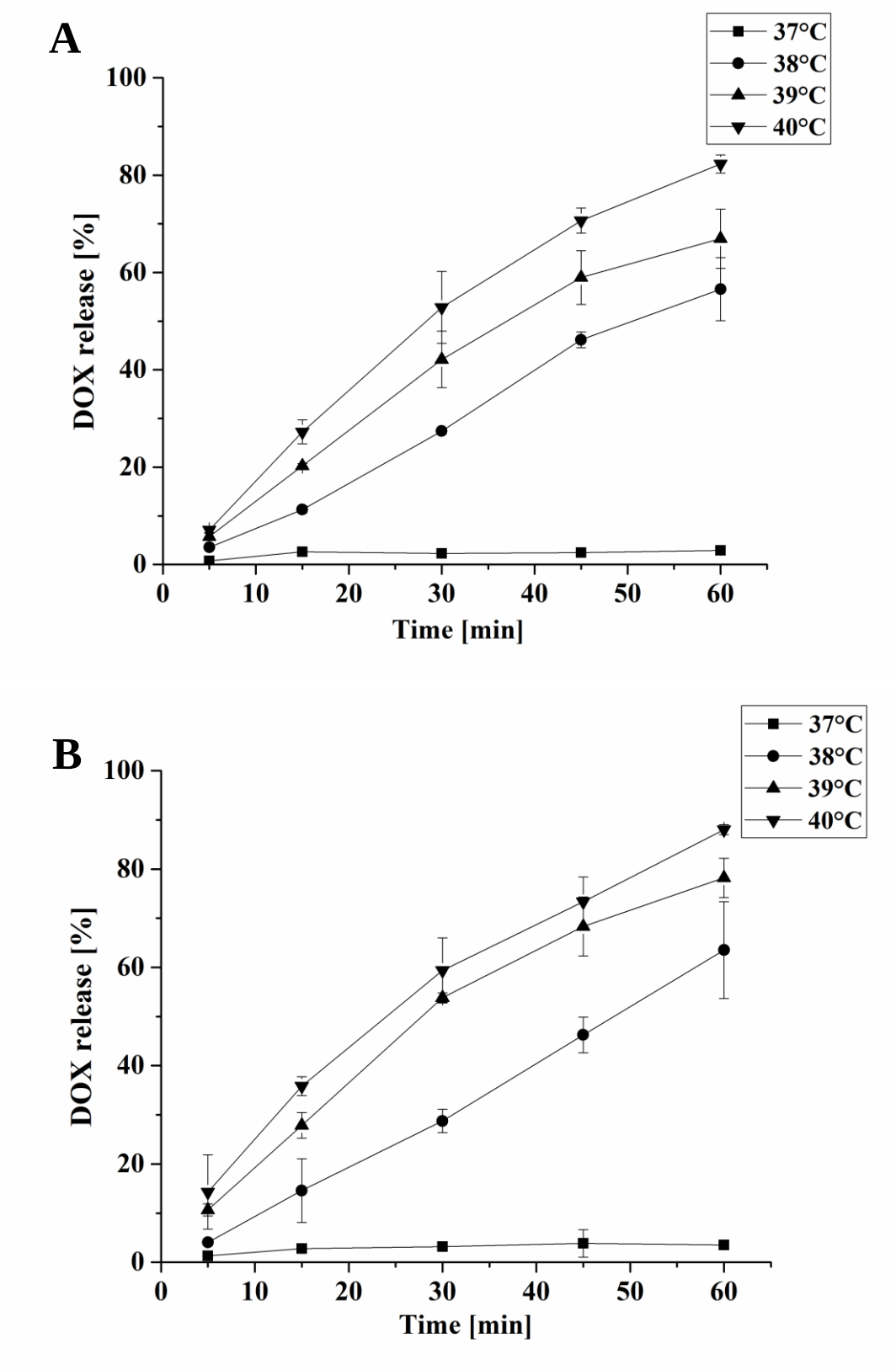

***Figure 20**: Time-dependent release of DOX from Lip$_{TS\text{-}GD}$ (A) and Lip$_{TS\text{-}GD\text{-}CY\text{-}MAB}$ (B) at various temperatures (37, 38, 39 and 40 °C). DOX release was plotted as an average of percentages ± SD of three independent experiments and the release of DOX within the first 60 min was measured.*

3.7. Ultra high magnetic resonance imaging

Gd-chelate is encapsulated in both $Lip_{TS\text{-}GD}$ and $Lip_{TS\text{-}GD\text{-}CY\text{-}MAB}$ thus giving these liposomes paramagnetic properties, to facilitate imaging mediated DOX delivery. Furthermore, in order to further understand and quantify the changes in the relaxation rate R1 of the liposomes, MR images and T1 quantification was performed. R1 was determined by measuring the relaxation time T1 at different dilutions of Gd-chelate before and after heating above T_m ($T > T_m$). The contrast of $Lip_{TS\text{-}GD}$ was low before heating, thus correlates with the results obtained by TEM image (Figure 17 B) which visualized Gd-chelate to be in the aqueous payload of the liposomes. The contrast is decreased because of the restricted water exchange between the outer and inner liposomal domains. After heating of $Lip_{TS\text{-}GD}$, Gd-chelate was released and higher water exchange was achieved, therefore, higher contrast was observed in Figure 21 A. Figure 21 B represents the relaxation rate of $Lip_{TS\text{-}GD}$ plotted against different Gd-chelate concentrations. Relaxivity *r1* before heating can be obtained from the slope of the black line and *r1* after heating is obtained from the slope of the red line. Where *r1* before heating is $3.10 \pm 0.5\ s^{-1}\ mM^{-1}$ and *r1* after heating is $4.01 \pm 0.58\ s^{-1}\ mM^{-1}$ (Figure 21 B).

It is observed that the release of the hydrophilic Gd-chelate is triggered at $T > T_m$, as R1 is increased after heating. The phospholipid layer surrounding the incorporated Gd-chelate hinders diffusion and exchange of water between the inner and outer compartments of liposomes, therefore, the longitudinal relaxation rate is increased after heating [160]. Indicating that Gd-chelate was successfully released after heating and higher water exchange was available from both the surrounding buffer and from the buffer entering the aqueous lumen of the liposomes, hence increasing the relaxation rate.

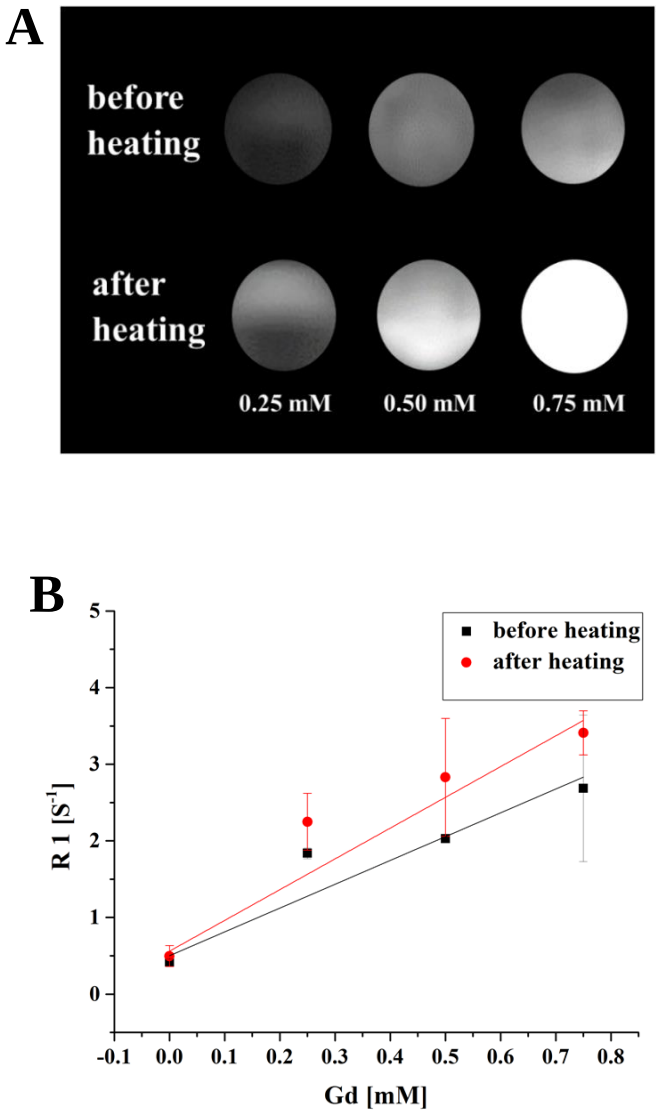

***Figure 21**: UHF-MRI images of different concentrations of Gd-chelate before and after heating of Lip $_{TS\text{-}GD}$ at $T > T_m$ (A). UHF-MRI relaxation rates were measured at different dilutions of Gd-chelate before and after heating ($T > T_m$) (B). It represents the slope of the fitted linear plot before (black) r1= 3.10 ± 0.5 s^{-1} mM^{-1} (Gd) and after heating (red) r1 = 4.01 ± 0.58 s^{-1} mM^{-1} (Gd).*

Moreover, evaluation of the paramagnetic properties of the Lip$_{TS\text{-}GD\text{-}CY\text{-}MAB}$ was conducted, T1 weighted images of Lip$_{TS\text{-}GD\text{-}CY\text{-}MAB}$ with different Gd-chelate dilutions before and after heating have higher contrast (Figure 22 A).

These results correspond with the results obtained from TEM images, as the Gd-chelate in Lip$_{TS\text{-}GD\text{-}CY\text{-}MAB}$ appears to be positioned in the lipid bilayer and protruding on the liposomal surface. Therefore, the possibility of water exchange is higher, thereafter, a more pronounced

contrast is observed. The relaxation rate R1 was determined after measuring relaxation time T1 at different dilutions of Gd-chelate before and after heating above T_m ($T > T_m$).

Relativity *r*1 before and after heating is determined from the slope (Figure 22 B), where *r*1 before heating is 4.91 ± 0.15 s^{-1} mM^{-1} and *r*1 after heating is 7.98 ±1.24 s^{-1} mM^{-1}. An increment in *r1* was observed after heating indicating a successful lipid bilayer destruction at $T > T_m$, which enabled water crossing throughout the disrupted membrane.

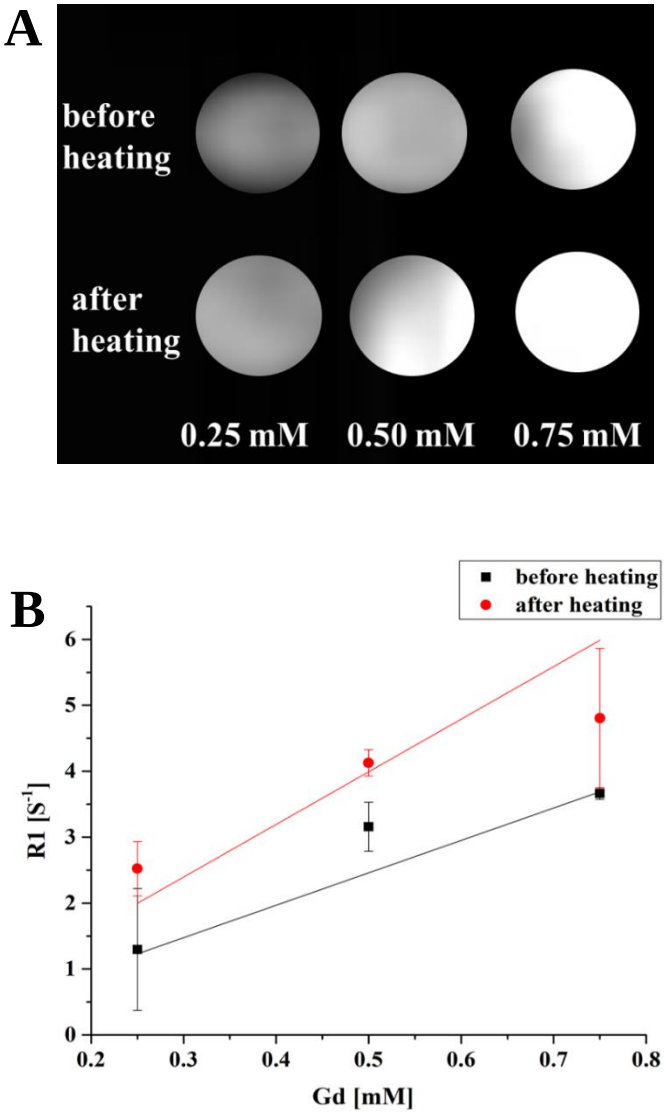

***Figure 22**: UHF-MRI images of different concentrations of Gd-chelate of $Lip_{TS\text{-}GD\text{-}CY\text{-}MAB}$ before and after heating (A). UHF-MRI relaxation rates measured at different dilutions of Gd-chelate before and after heating (T > Tm) (B). Slope of the fitted linear plot before heating (black) r1=4.91 ± 0.15 s-1 mM-1 (Gd) and after heating (red) r1= 7.98 ±1.24 s-1 mM-1 (Gd).*

These findings correspond with previously published results by de Smet *et al.* [65] and Fossheim *et al.* [159], who studied the feasibility of Gd-DTPA encapsulation in liposomes and the triggered release of Gd-chelate from liposomes, respectively. In both works, there was an increase in *r1* as the temperature reached T_m. T1 weighted images of liposomes with different Gd-chelate concentrations after heating appeared with higher contrast. The longitudinal relaxivity of the liposomal encapsulated paramagnetic MRI contrast agent is regulated by the water diffusion across the phospholipid bilayer that increases with temperature increase. Regarding the cellular internalizing cell receptors, it has been reported that the longitudinal relaxivity *r1* is regulated and can be modified by cellular compartmentalization effects. Therefore, an efficient *r1* does not only help inducing hyperthermia but can as well provide promising opportunities to observe and record the biological fate of liposomes either *in vitro* or *in vivo* [161].

3.8. Cytotoxicity studies upon hyperthermia

MTT assay was used to determine the cell viability after treatment with DOX-liposomes. Cell toxicity experiments were investigated against MDA-MB-231-ctrl cells obtaining overexpression of ADAM8 on their cell surface. To investigate the optimum incubation conditions, cells were incubated with $Lip_{TS\text{-}GD}$ for 3 or 3.5 hours at 37 °C followed by thermal therapy at 40 °C or cellular exposure to commercially available UHF-MRI field for 30 or 60 min (Figure 23).

Cells treated at 37 °C showed cellular viability of about 85 % proving that the liposomes are mostly intact at normal physiological temperature. This correlates with the results obtained by DSC thermogram (Figure 19 A) as the first detected change in temperature of $Lip_{TS\text{-}GD}$ was at about 38 °C and with DOX release profile (Figure 20 A). The cellular toxicity obtained after 37 °C treatment can either be explained by minor liposomal DOX lumen leakage or by the endocytosis events of DOX-liposomes in the cells independent of the triggered release. Our DDS shows low toxicity at 37 °C, whereas DOX low-temperature sensitive liposomes with cell viability < 40 % at 37 °C were reported by de Smet *et al.* [65]. Cells treated at 38 °C manifested a decrease in cellular viability to 77 % and 63 % after 30 min and 60 min of thermal treatment, respectively. Consequently, we can conclude that the $Lip_{TS\text{-}GD}$ portrays high thermosensitivity. At 39 °C and 40 °C thermal treatment, a reduction in cellular viability was observed to

67 % or 51 % and 45 % or 31 % after 30 or 60 min of treatment was observed, respectively. This indicates that the release of DOX from our liposomes is only triggered upon hyperthermia. This correlates with the results obtained from the release studies displaying a gradual constant release of DOX in correlation with temperature and time increase. After 30 or 60 min treatment under UHF-MRI, cells exhibited cellular viability of 49 % and 36 %, which is comparable to cellular viability after thermal treatment at 40 °C.

Temperature of samples with $Lip_{TS\text{-}GD}$ was measured after UHF-MRI exposure using IR thermometer and it recorded 38.5 ± 0.3 °C. Thus using a UHF-MRI could be used to induce hyperthermia slightly higher than the physiological temperature in a tumor location. Cell viability in UHF-MRI correlated with temperature and exposure time.

Thermosensitive liposomes exhibit preferable characteristics in cancer treatment as they provide a more effective accumulation of DOX within the nuclear domain [140]. This can be attributed to the endocytotic thermo-triggered release of liposomal DOX-payload after cellular localization, these results are consistent with that described by Pan *et al.* [162]. This correlates with magnetic hyperthermia induced by MRI [104-106,163] and enhanced cellular uptake of magnetic particles under the magnetic field as previously reported [164-166].

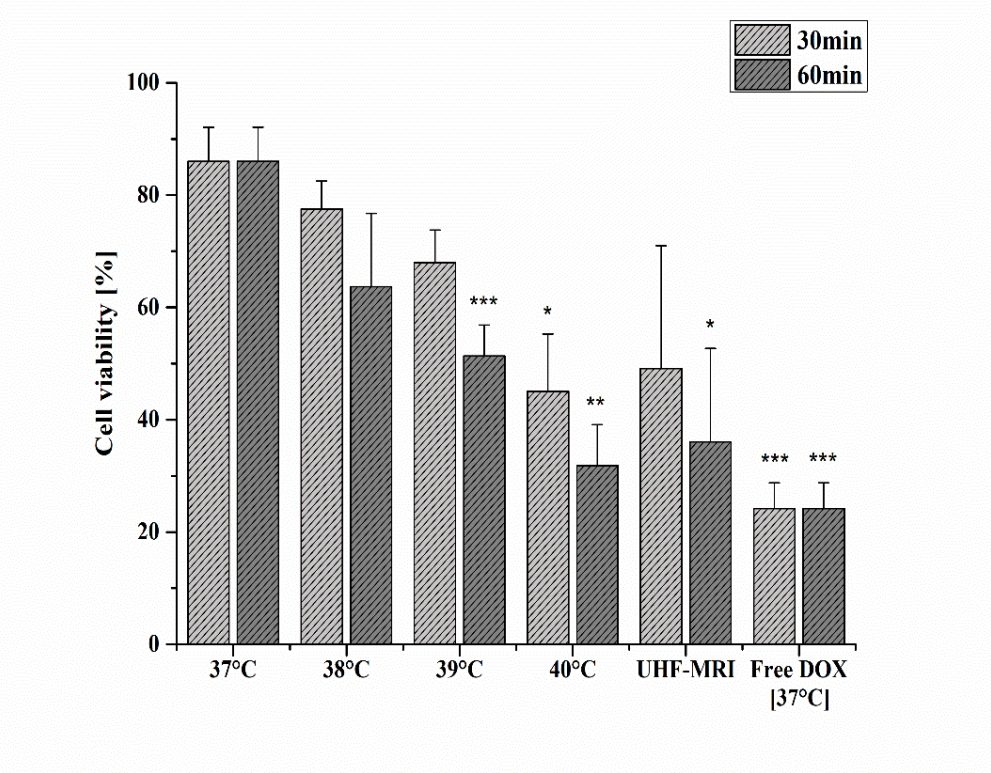

***Figure 23**: Temperature-dependent cytotoxicity of DOX-$Lip_{TS\text{-}GD}$. MDA-MB-231 were incubated with $Lip_{TS\text{-}GD}$ liposomes for 3 or 3.5 hours at 37 °C followed by thermal therapy or cellular exposure to UHF-MRI field for 60 or 30 minutes. Data is expressed as the mean ± SD. For statistical analysis the results were compared against the results of treated cells at 37°C.*

Moreover, the evaluation of the cellular viability for $Lipo_{TS\text{-}GD}$ has enabled us to choose the optimal thermal treatment time span for the additionally modified liposomes, i.e., $Lip_{TS\text{-}GD\text{-}CY}$ and $Lip_{TS\text{-}GD\text{-}CY\text{-}MAB}$. The chosen thermal treatment time was set at 60 min, depending on the previous results.

Cytotoxicity for $Lip_{TS\text{-}GD\text{-}CY}$ and $Lip_{TS\text{-}GD\text{-}CY\text{-}MAB}$ were also carried out on MDA-MB-231-ctrl cells. Cells were incubated for 3 hours at 37 °C followed by thermal therapy or cellular exposure to commercially available UHF-MRI field for 60 min (Figure 24). Furthermore, cellular cytotoxicity experiments were carried out in MDA-MB-231-ctrl cells to evaluate the contribution of targeting features implemented by DOX-$Lip_{TS\text{-}GD\text{-}CY}$ and DOX-$Lip_{TS\text{-}GD\text{-}CY\text{-}MAB}$ (targeting of ADAM8 receptors, and magnetic hyperthermia targeting). Both liposomal formulations ($Lip_{TS\text{-}GD\text{-}CY}$ and $Lip_{TS\text{-}GD\text{-}CY\text{-}MAB}$) were evaluated under the presence and absence of hyperthermia or UHF-MRI exposure. Cellular cytotoxicity was low at 37 °C, with cellular viability of 85 % in the case of DOX-$Lip_{TS\text{-}GD\text{-}CY}$ and 80 % in the case of DOX-$Lip_{TS\text{-}GD\text{-}CY\text{-}MAB}$, this can be ascribed to DOX lumen leakage or by the endocytosis events of DOX-liposomes in the cells as described above. Thus indicating that the incorporation of cyanur or/and the cellular modification did not affect the drug release from liposomes at normal physiological temperature. The integrity of the liposomal formulation is rather intact at 37 °C. As shown by the DSC thermogram for $Lip_{TS\text{-}GD\text{-}CY\text{-}MAB}$, the recorded phase transition temperature T_m is about 39 °C. Thus allow higher cellular toxicity at a temperature slightly higher than the physiological temperature. At 38 °C thermal treatment cellular viability decreased around 20 % from that obtained at 37 °C in both $Lip_{TS\text{-}GD\text{-}CY}$ and $Lip_{TS\text{-}GD\text{-}CY\text{-}MAB}$, this points out the high thermosensitivity and rapid liposomal response to a slight change in temperature. At 39 °C and 40 °C cells showed a significant reduction in cellular viability to 48 % and 32 % in the case of $Lip_{TS\text{-}GD\text{-}CY}$, and 41 % and 27 % in the case of $Lip_{TS\text{-}GD\text{-}CY\text{-}MAB}$, respectively.

Temperatures of samples with $Lip_{TS\text{-}GD\text{-}CY}$ and $Lip_{TS\text{-}GD\text{-}CY\text{-}MAB}$ were measured after UHF-MRI exposure by IR thermometer and 38.6 ± 0.3 °C was recorded. Moreover, after thermal treatment under UHF-MRI, cellular viability was 36 % and 29 % in the case of DOX-$Lip_{TS\text{-}GD\text{-}CY}$ and DOX-$Lip_{TS\text{-}GD\text{-}CY\text{-}MAB}$, respectively. DOX-liposomes cytotoxicity after 60 min under UHF-MRI exposure showed a good correlation to the surviving fraction obtained at 40 °C. This correlates with magnetic hyperthermia induced by UHF-MRI and elevated cellular uptake under the magnetic field as reported by Venugopal *et al.* [165]. The increased uptake under the magnetic field is ascribed to either energy-dependent endocytotic events or a simple pulling of the magnetic nanocarrier into the cell by magnetic force [166].

Thus, confirming the thermosensitive feasibility of the prepared liposomes as a triggerable nanocarrier. When comparing DOX-Lip$_{TS\text{-}GD\text{-}Cy}$ and DOX-Lip$_{TS\text{-}GD\text{-}CY\text{-}MAB}$, the highest cytotoxicity was observed after the combination of targeting and magnetic hyperthermia. These results correlate with previous reports by Laginha *et al*. [167] and Venugopal *et al*.[165], who have observed an increased in cytotoxicity when facilitating magnetic hyperthermia.

We hypothesized that the incorporation of MAB 1031 into liposomes slightly increased the cellular internalization, as can be observed by the increased cellular cytotoxicity. This supports the previous suggestion that targeted liposomes displayed higher cytotoxicity to its non-targeted counterparts [168]. Moreover, these findings implement that immuno targeting and magnetic induced hyperthermia are synergically performing for the enhancement of cellular uptake and cytotoxicity [169,170].

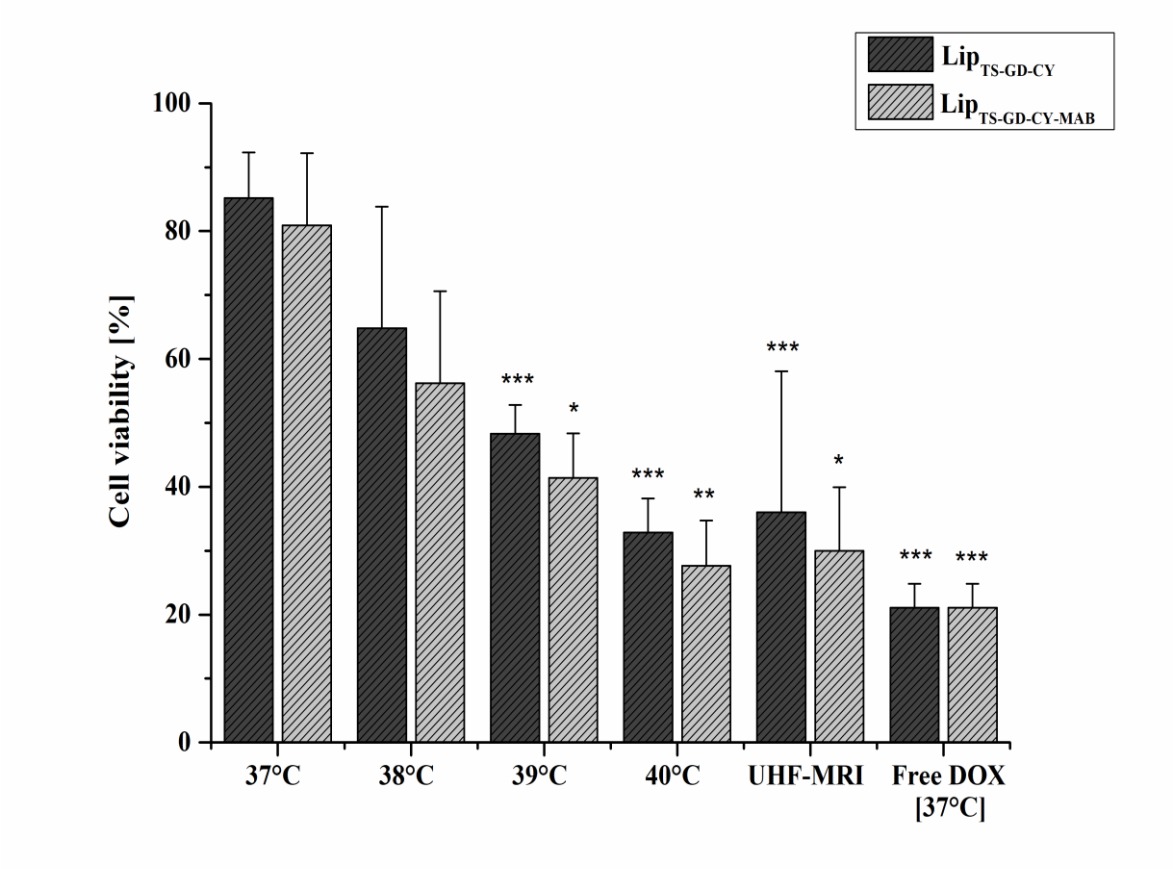

***Figure 24**: Temperature-dependent cytotoxicity of DOX-Lip$_{TS\text{-}GD\text{-}CY}$ and DOX-Lip$_{TS\text{-}GD\text{-}CY\text{-}MAB}$. MDA-MB-231-ctrl were incubated with Lip$_{TS\text{-}GD\text{-}CY}$ or DOX-Lip$_{TS\text{-}GD\text{-}CY\text{-}MAB}$ liposomes for 3 h at 37 °C followed by thermal therapy or cellular exposure to UHF-MRI for 60 min. Data is expressed as the mean ± SD. For statistical analysis, the results were compared against the results of treated cells at 37 °C.*

3.9. Cellular uptake evaluation

The ability of the nanocarrier system to load DOX preferentially inside the cellular compartment makes it available to exert its cytotoxic effects. The cellular uptake studies of DOX were performed on MDA-MB 231-ctrl cells and the internalization and the subcellular localization of DOX were visualized using confocal laser scanning microscope (CLSM) (Figure 25). DAPI was used to counterstain the nuclei for cell visualization under CLSM. Results were compared with free DOX uptake at 37 °C, which appears to be localized in the nuclear area [171]. As expected, a minor release of DOX was achieved after incubating the $Lip_{TS\text{-}GD}$ at 37 °C, and its uptake was less pronounced than at 40 °C. Hence, it showed minimal uptake (Figure 25). Cells after thermal and UHF-MRI treatments rendered strong red fluorescence indicating that the liposomes are intranuclearly internalized by MDA-MB 231-ctrl. The observed increase in cellular uptake of DOX at 40 °C closely correlates to the enhanced DOX release as previously discussed. DOX-$Lip_{TS\text{-}GD}$ after UHF-MRI exposure prevailed a reasonable enhancement in DOX distribution throughout the cellular compartments. Cells appear oval to spherical in shape, indicating cytotoxicity induced by apoptosis. This correlates with the appearance of the cells incubated with free DOX. The varying fluorescence intensity indicates that the uptake was enhanced in the presence of an external magnetic field as previously reported [172,173]. The enhanced cellular uptake under magnetic exposure can be attributed to an energy-dependent endocytic event or the liposomes are just pulled directly into the cells by the force of the magnetic field [166].

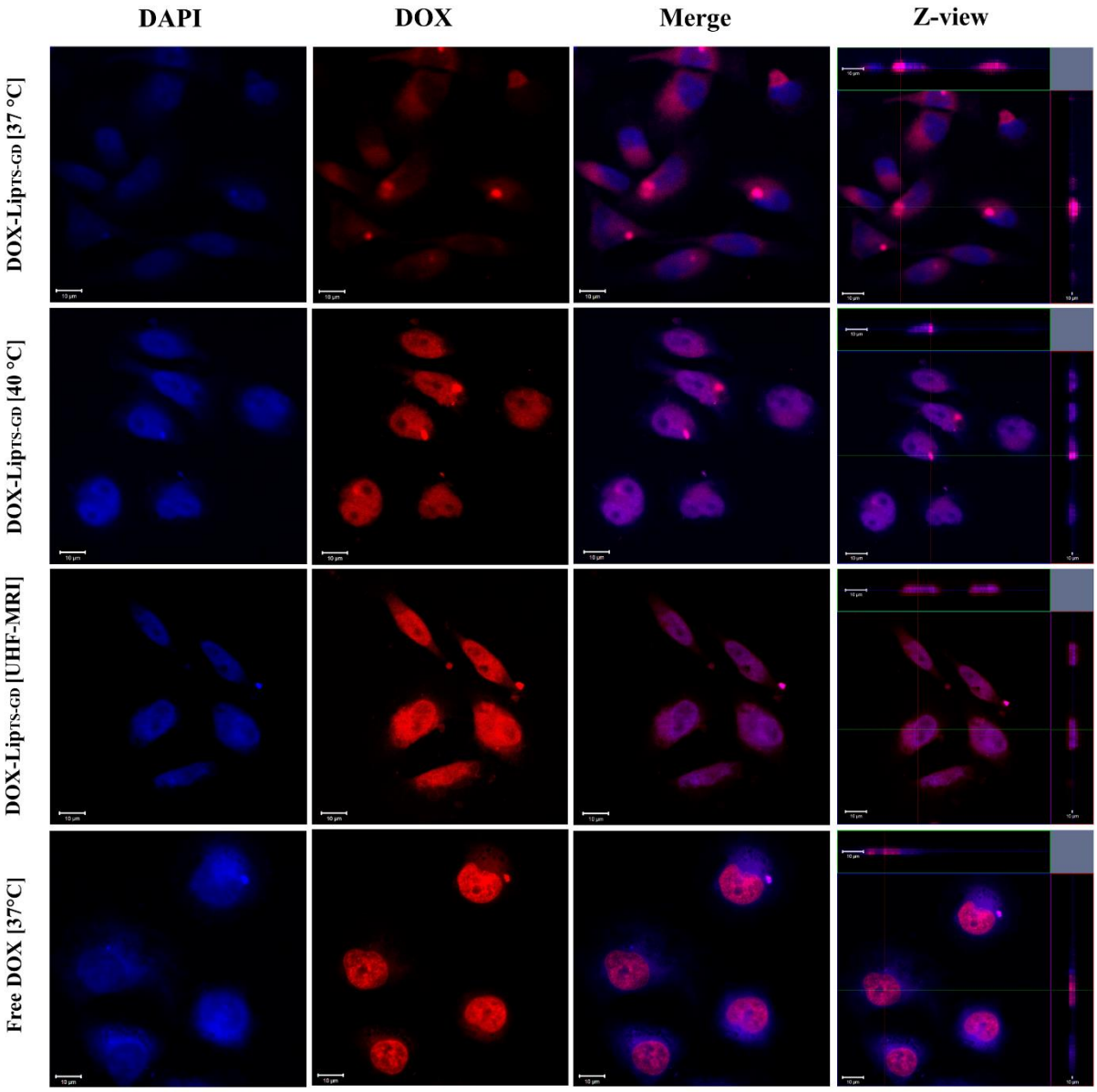

***Figure 25**: Temperature-dependent confocal laser scanning acquisitions of MDA-MB-231-ctrl cells treated with DOX Lip$_{TS\text{-}GD}$ or free DOX. Scale bar represents 10 µm.*

3.10. Pathway studies

Liposomes interact with the cell membrane in different mechanisms; they either adsorb to the cellular surface and the subsequently released drug would be uptake into the liposomal membrane by simple diffusion. They can simply fuse with the cellular membrane, owing to that both membranes - liposomal and cellular - are similar in their component and functionality. Another possibility is the exchange of the lipids between the liposomal membrane and the cellular membrane after the liposomes adhesion to the cellular membrane. The last and most common possibility of cellular uptake for the liposomes is endocytosis [174].

Active endocytosis is comprised of several pathways: clathrin-mediated endocytosis (CME), caveolin-dependent endocytosis, and others that have been reported recently including transmembrane penetration [175].

Moreover, CME can be classified as non-specific adsorption uptake, which occurs due to hydrophobic or electrostatic interactions that facilitate the internalization process. Or receptor-mediated uptake that carries out the uptake of the nanocarriers that is modified with a specific ligand) after their binding to receptors on the cell surface. This binding triggers the cellular plasma membrane, which forms “coated pits” that subsequently enable the uptake of the liposomes into the cells [176].

To further assess the mechanism of liposomal internalization and cellular uptake of $Lip_{TS\text{-}GD\text{-}CY}$ and $Lip_{TS\text{-}GD\text{-}CY\text{-}MAB}$ into MDA-MB-231-ctrl cells, endocytotic pathways were investigated. Filipin III and chlorpromazine were employed to inhibit the caveolae-mediated and clathrin-mediated endocytosis, respectively (Figure 26). Cells treated with $Lip_{TS\text{-}GD\text{-}CY}$ and $Lip_{TS\text{-}GD\text{-}CY\text{-}MAB}$ under UHF-MRI without pathway inhibition exerted comparable cytotoxicity as previously described (Figure 24). Pre-incubation with filipin III showed minor inhibition of liposomal uptake.

Pre-incubation with chlorpromazine inhibited the uptake of both $Lip_{TS\text{-}GD\text{-}CY}$ and $Lip_{TS\text{-}GD\text{-}CY\text{-}MAB}$. The notable effect of chlorpromazine inhibition indicates that cellular uptake occurs predominantly by clathrin-mediated endocytosis. These results correspond with previously reported works stating that spheres < 200 nm in size are mainly taken up into the cells by the formation of clathrin-coated pits [177,178].

On another note, $Lip_{TS\text{-}GD\text{-}CY\text{-}MAB}$ exhibited less cellular viability, so it can be assumed that the antibody-mediated endocytosis plays a role in the internalization of MAB decorated liposomes [179]. Cells treated with $Lip_{TS\text{-}GD}$ and $Lip_{TS\text{-}GD\text{-}MAB}$ at 37 °C exhibited low toxicity with or without inhibition.

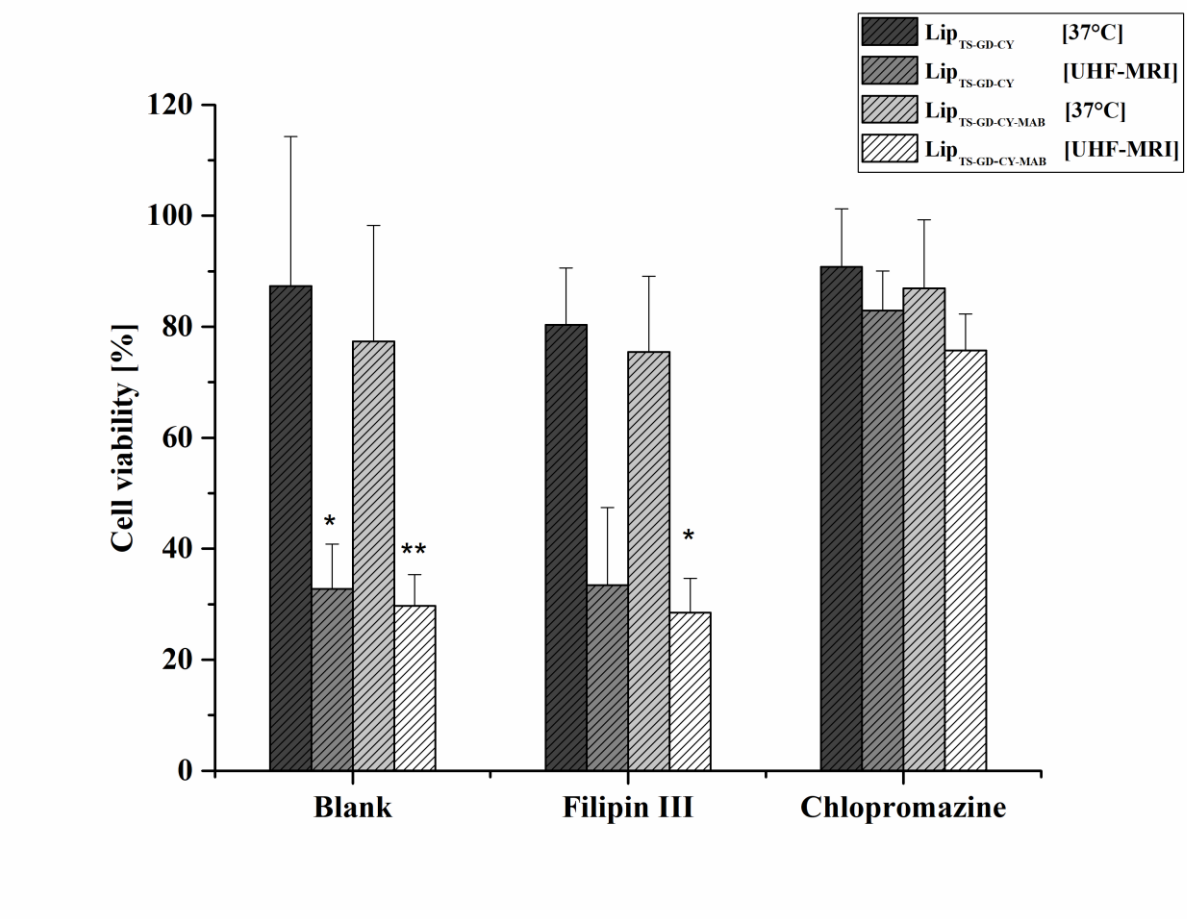

***Figure 26**: Cell viability of MDA-MB-231-ctrl cells after incubation with $Lip_{TS\text{-}GD\text{-}CY}$ and $Lip_{TS\text{-}GD\text{-}CY\text{-}MAB}$ in the presence of two pathway inhibitors (filipin III or chlorpromazine) with/without UHF-MRI exposure. Blank represents cells without inhibitors. For statistical analysis, results were compared with treated blank cells with the same conditions.*

3.11. Mechanism of endosomal escape by fluorescence microscopy

A successful endosomal escape is important for the release of cargo from a nanoscaled carrier. Therefore, to check the role of ligand-gated antibody against ADAM8 antigen, endosomal escape was investigated in MDA-MB231-ctrl and MDA-MB-231-rna cell lines. The cells were treated with NBD-labelled (green) liposomal formulations ($Lip_{TS\text{-}GD\text{-}CY\text{-}MAB}$ and $Lip_{TS\text{-}GD\text{-}CY}$). Figure 27 depicted that higher green fluorescence signals were obtained from the cells incubated with the ADAM8 antibody tagged liposomes, showing the ligand-specific targeting of the antibody to the cells. In addition, to further characterize the intracellular trafficking, the co-localization mechanism using a lysosomal marker (Lyso Tracker® red-DND 99) was used. It was observed that the targeting by ADAM8 antibody significantly enhanced the co-localization of liposomes within the lysosomes, which leads to a yellow color as shown by Guo *et al*.[180] and efficient release of cargo into the cytosol without any lysosomal degradation. On the other hand, NBD-$Lip_{TS\text{-}GD\text{-}CY}$, showed a negligible endosomal escape, suggesting the contribution of ADAM8 antibody in the facilitation of endocytosis and endosomal release. These results indicate the previous report by Mortensen *et al*. [181], which explains that the incorporation of the antibody to the liposomes would selectively increase the cellular internalization due to antibody binding to cellular surface.

To evaluate the active targeting by our nanocarrier system, MDA-MB-231-rna cells were incubated with NBD-labelled (green) liposomal formulations ($Lip_{TS\text{-}GD\text{-}CY}$ and $Lip_{TS\text{-}GD\text{-}CY\text{-}MAB}$). It has been observed that lower green fluorescence signals were obtained from the cells incubated with the ADAM8 antibody tagged liposomes, which indicated that the ligand-specific targeting of the antibody can only be accomplished by the presence of specific receptor sites. The results of figure 28 also showed a decreased co-localization of liposomes and the lysosomal vicinity further confirming the lower cellular uptake of the carrier system.

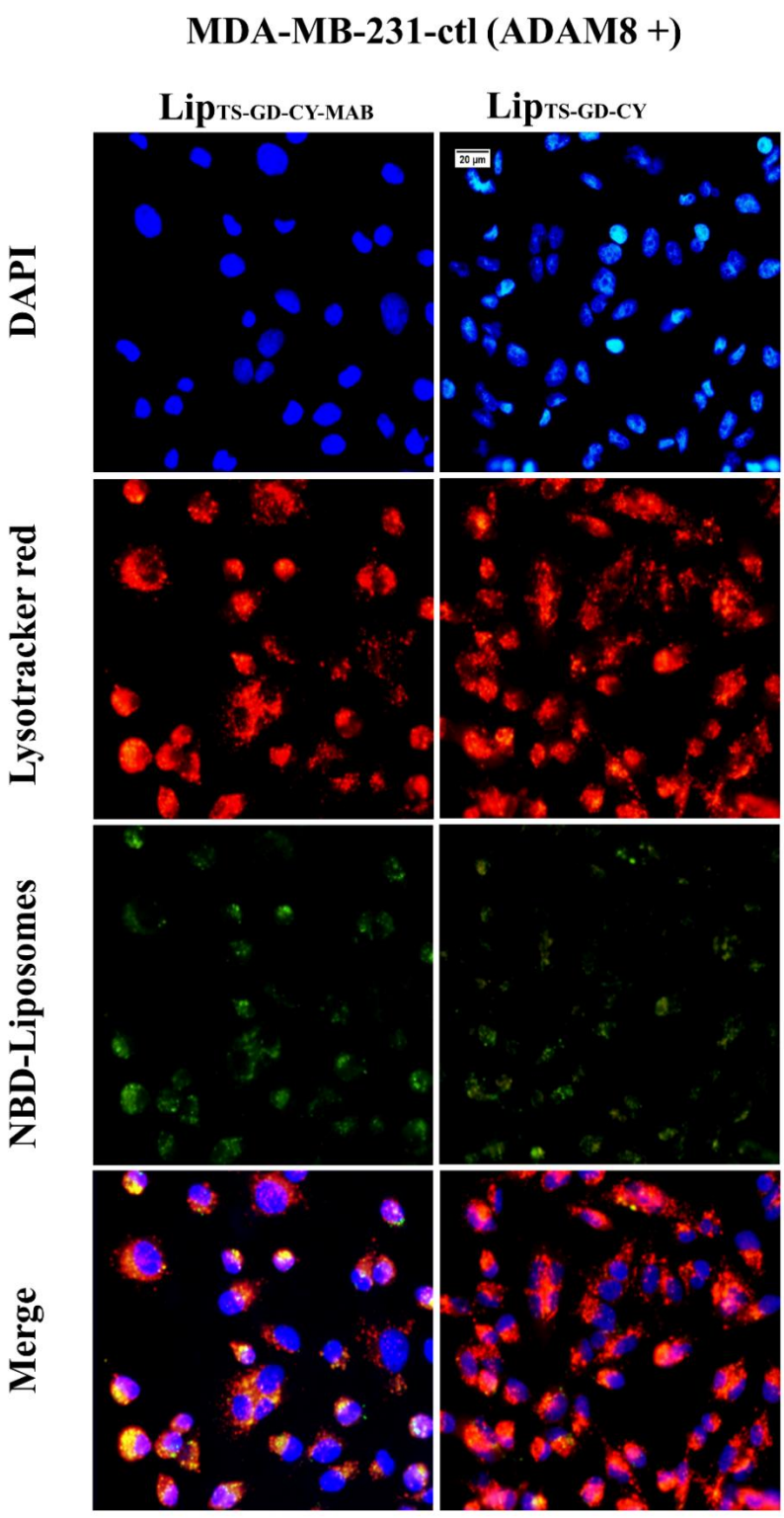

***Figure 27**: Endosomal escape of NBD labeled liposomal formulation with or without MAB1031 against MDA-MB-231-ctrl cells, using fluorescence microscopy. Blue channel depicting the nuclei staining, while the red fluorescence represents the lysosomes. Green signals depicting the NBD labeled liposomes. Colocalization of the liposome within the lysosomes indicated by yellow color. Scale bar 20µm.*

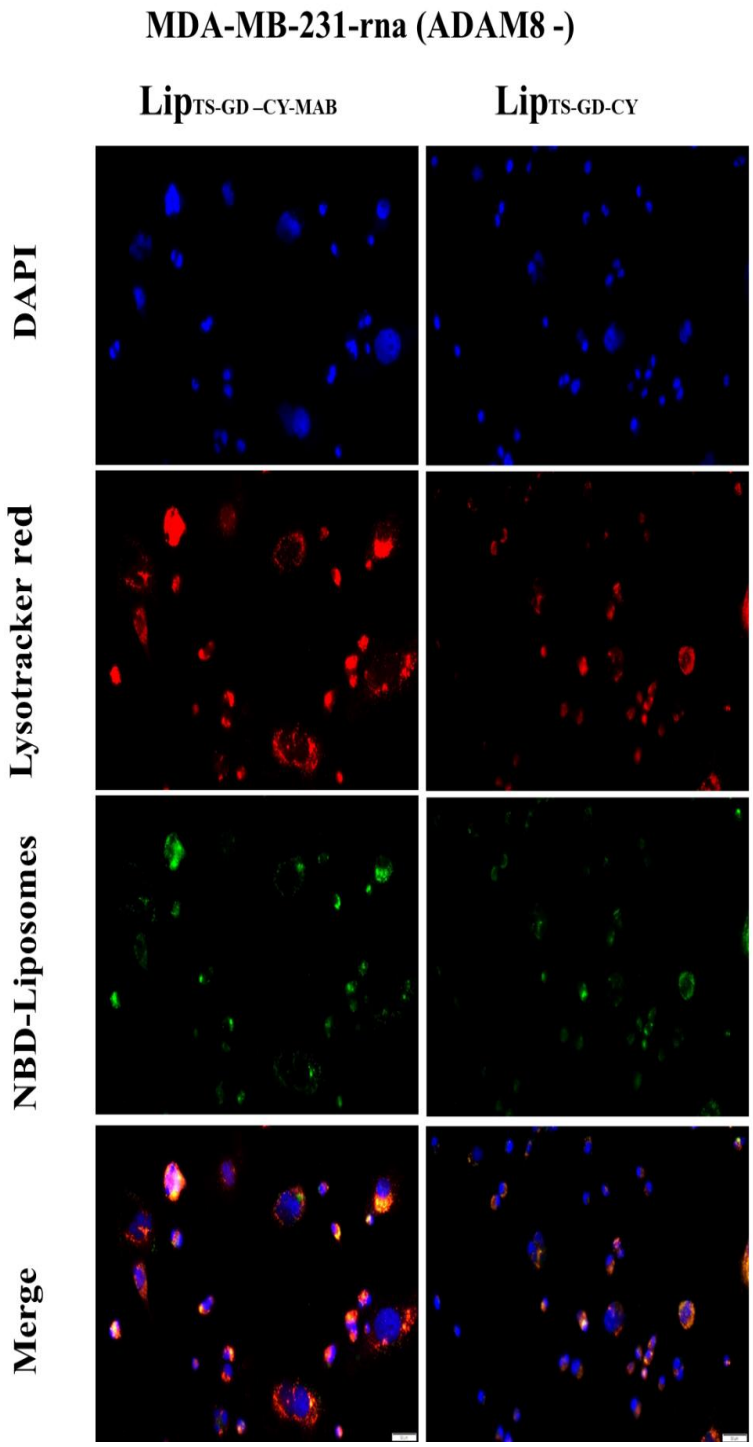

***Figure 28**: Endosomal escape of NBD labeled liposomal formulation with or without MAB 1031 against MDA-MB-231-rna cells, using fluorescence microscopy. Blue channel depicting the nuclei staining, while the red fluorescence represents the lysosomes. Green signals depicting the NBD labeled liposomes. Colocalization of the liposome within the lysosomes indicated by yellow color. Scale bar 50µm.*

3.12. *In vitro* evaluation of ADAM8 targeting by immunoliposomes

Commercially available nontargeting liposomal DOX formulations (e.g. Doxil®) manifest an enhanced safety profile compared to conventional chemotherapy and exhibit little adverse effects. However, these FDA approved chemotherapeutics fail to exhibit enhanced clinical benefits in treating TNBC due to their lack of specific targeting to the tumor tissues [182]. Consequently, a delivery system to specifically target the TNBC is the need of time to overcome the demerits, as mentioned above. One of the approaches to achieve targeting to the TNBC cells in their solid tumors or circulating cells (metastatic) is the use of cellular modified liposomes. One of the major modification for targeting is the PEGylation of liposomes, as the PEGylation achieve long-circulating liposomes allowing higher accumulation of the liposomes in the solid tumors by EPR effect. One the other hand, EPR effect is hampered by the disrupted vascularity system of the tumor as well as it lacks the ability to target circulating cells or normally vascularized tumors. For a more efficient active targeting of TNBC, liposomes can be surface modified by the conjugation of therapeutic ligands, e.g. aptamers, or by the conjugation of antibodies.

3.12.1. Cellular binding investigation using washing method

MDA-MB-231-ctrl and MDA-MB-231-rna cells were treated with NBD-$Lip_{TS\text{-}GD\text{-}CY\text{-}MAB}$ and NBD-$Lip_{TS\text{-}GD\text{-}CY}$ for 2 h at 4 °C to prevent any endocytotic events as the main object of this experiment was to evaluate the cellular binding capabilities of the modified / non-modified liposomes regardless of the endocytosis. NBD-PE was used as a colored lipid that allows fluorescence imaging of the treated cells with the liposomes. This would not only allow imaging it would as well allow quantification of the liposomal binding by the fluorescence intensity. In the case of MDA-MB-231-ctrl cells, an increment in NBD fluorescence in the case of $Lip_{TS\text{-}GD\text{-}CY\text{-}MAB}$ in comparison with its non-targeted counterpart ($Lip_{TS\text{-}GD\text{-}CY}$) was observed, indicating effective cellular binding (Figure 29A) [75]. In the case of MDA-MB-231-rna cells, the absence of ADAM8 receptor deprived the $Lip_{TS\text{-}GD\text{-}CY\text{-}MAB}$ to specifically target the cells that further confirming the lock key phenomenon of ligand-specific binding (Figure 30). Moreover, in the case of $Lip_{TS\text{-}GD\text{-}CY}$ no significant binding was achieved (Figure 29).

Notably, the overexpressed ADAM8 ectodomain on the cellular surface of MDA-MB-231-ctrl cells is responsible for selective binding of $Lip_{TS\text{-}GD\text{-}CY\text{-}MAB}$. These results correlate with a previous report presenting MAB 1031 as a therapeutic target of ADAM8 for TNBC cells [113]. An efficient binding may contribute to ADAM8 inhibition and therefore decrease tumor adhesion, metastasis, and dissemination. Furthermore, the fluorescence intensity of the cellular binding was quantified using fluorescence intensity reader (Figure 29B), the quantified fluorescence intensity of the binding of $Lip_{TS\text{-}GD\text{-}CY\text{-}MAB}$ was the highest to MDA-MB-231-ctrl indicating the targetability of the MAB 1031 modified liposomes to the ADAM8 positive cells.

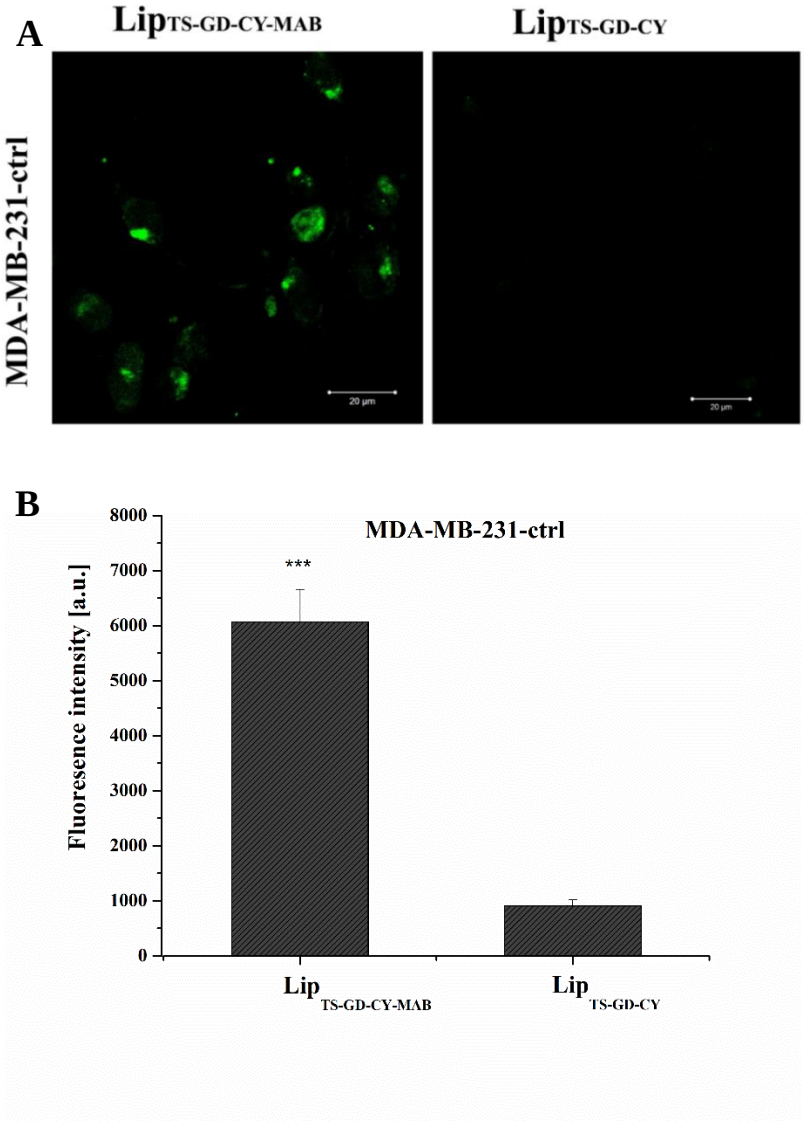

***Figure 29**: Binding efficiency of NBD labeled liposomal formulations $Lip_{TS\text{-}GD\text{-}CY\text{-}MAB}$ and $Lip_{TS\text{-}GD\text{-}CY}$ on MDA-MB-231-ctrl cells (A). Green signals depicting the NBD labeled liposomes. Higher green fluorescence depicting the enhanced cellular binding of the liposomes. Scale bar represents 20 µm. Quantitative determination of the binding efficiency of NBD labeled liposomal formulation $Lip_{TS\text{-}GD\text{-}CY\text{-}MAB}$ and $Lip_{TS\text{-}GD\text{-}CY}$ on MDA-MB-231 cells (B).*

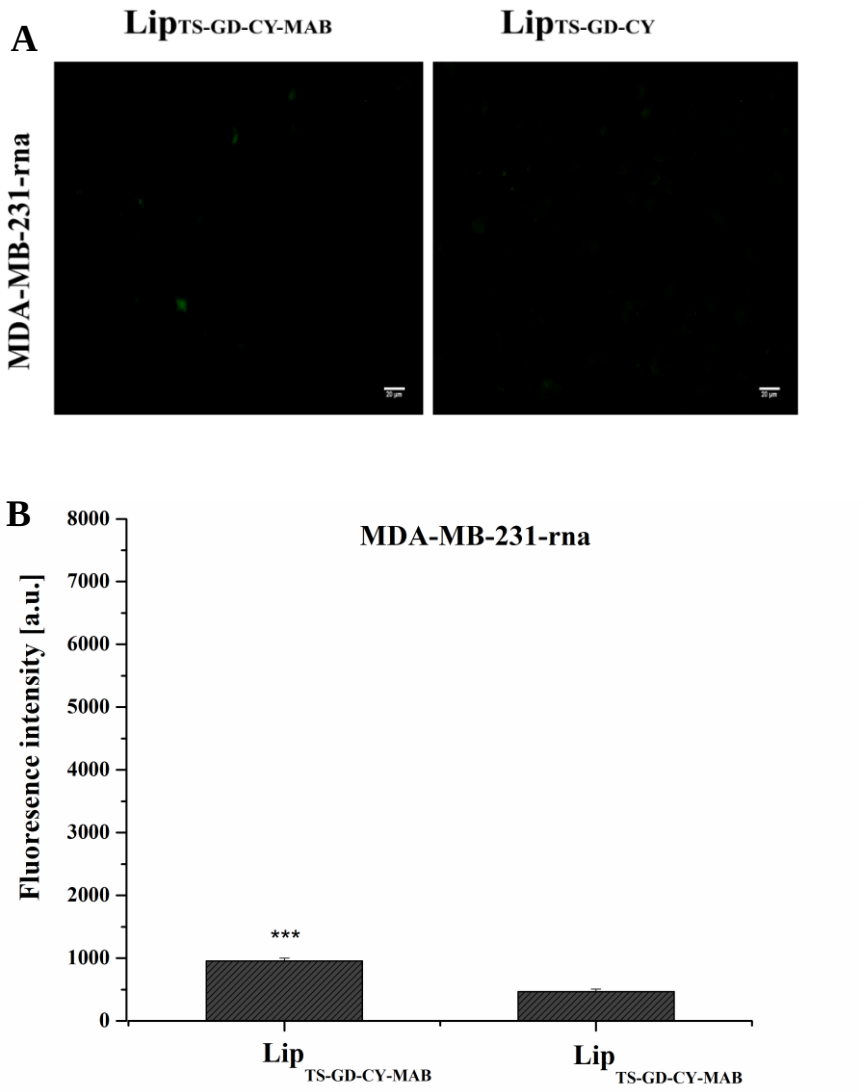

Figure 30: *Binding efficiency of NBD labeled liposomal formulations* $Lip_{TS\text{-}GD\text{-}CY\text{-}MAB}$ *and* $Lip_{TS\text{-}GD\text{-}CY}$ *on MDA-MB-231-rna cells (A). Green signals depicting the NBD labeled liposomes. The green fluorescence depicting the cellular binding of the liposomes. Scale bar represents 20 µm. Quantitative determination of the binding efficiency of NBD labeled liposomal formulation* $Lip_{TS\text{-}GD\text{-}CY\text{-}MAB}$ *and* $Lip_{TS\text{-}GD\text{-}CY}$ *on MDA-MB-231-rna cells (B).*

3.12.2. Evaluation of cellular binding using washing method under UHF-MRI

Both $Lip_{TS\text{-}GD\text{-}CY\text{-}MAB}$ and $Lip_{TS\text{-}GD\text{-}CY}$ obtain Gd in their composition. Gd-chelate is a contrast agent that would allow imaging as well as quantification of the cellular binding capabilities under UHF-MRI imaging. Presumably, liposomes with higher binding efficiency would illustrate higher contrast in the UHF-MRI images. While liposomes with less binding abilities would be washed out during the washing protocol, therefore, lesser amounts of Gd would be present and consequently lower contrast would be evident.

As a proof of concept for the binding efficiency, MDA-MB-231-ctrl and MDA-MB-231-rna cells were treated with both $Lip_{TS\text{-}GD\text{-}CY\text{-}MAB}$ and $Lip_{TS\text{-}GD\text{-}CY}$ and UHF-MRI images were acquired after washing protocol. MDA-MB-231-ctrl cells treated with $Lip_{TS\text{-}GD\text{-}CY\text{-}MAB}$ showed a significant contrast in comparison to its counterpart $Lip_{TS\text{-}GD\text{-}CY}$ (Figure 31A, 32A), which indicate a higher binding efficiency. MDA-MB-231-rna treated with both the abovementioned liposomes showed no noticeable contrast under UHF-MRI, thus represents a lesser Gd concentration in the treated area, which proves that less cellular binding was achieved.

Additionally, the mean gray value of the cellular binding was measured, the mean gray value of the binding of $Lip_{TS\text{-}GD\text{-}CY\text{-}MAB}$ was the highest in MDA-MB-231-ctrl (Figure 31B) indicating the targetability of the MAB 1031 modified liposomes to the ADAM8 positive overexpression cells. The noticeable availability of Gd serves as proof of the significant enhancement in $Lip_{TS\text{-}GD\text{-}CY\text{-}MAB}$ binding after incorporation of MAB 1031 antibody. Whereas, no significant gray value has been observed in the case of MDA-MB-231-rna cells for both liposomal formulations. Thereupon, $Lip_{TS\text{-}GD\text{-}CY\text{-}MAB}$ could be used for diagnostic targeted imaging of solid tumors and metastatic cells under UHF-MRI.

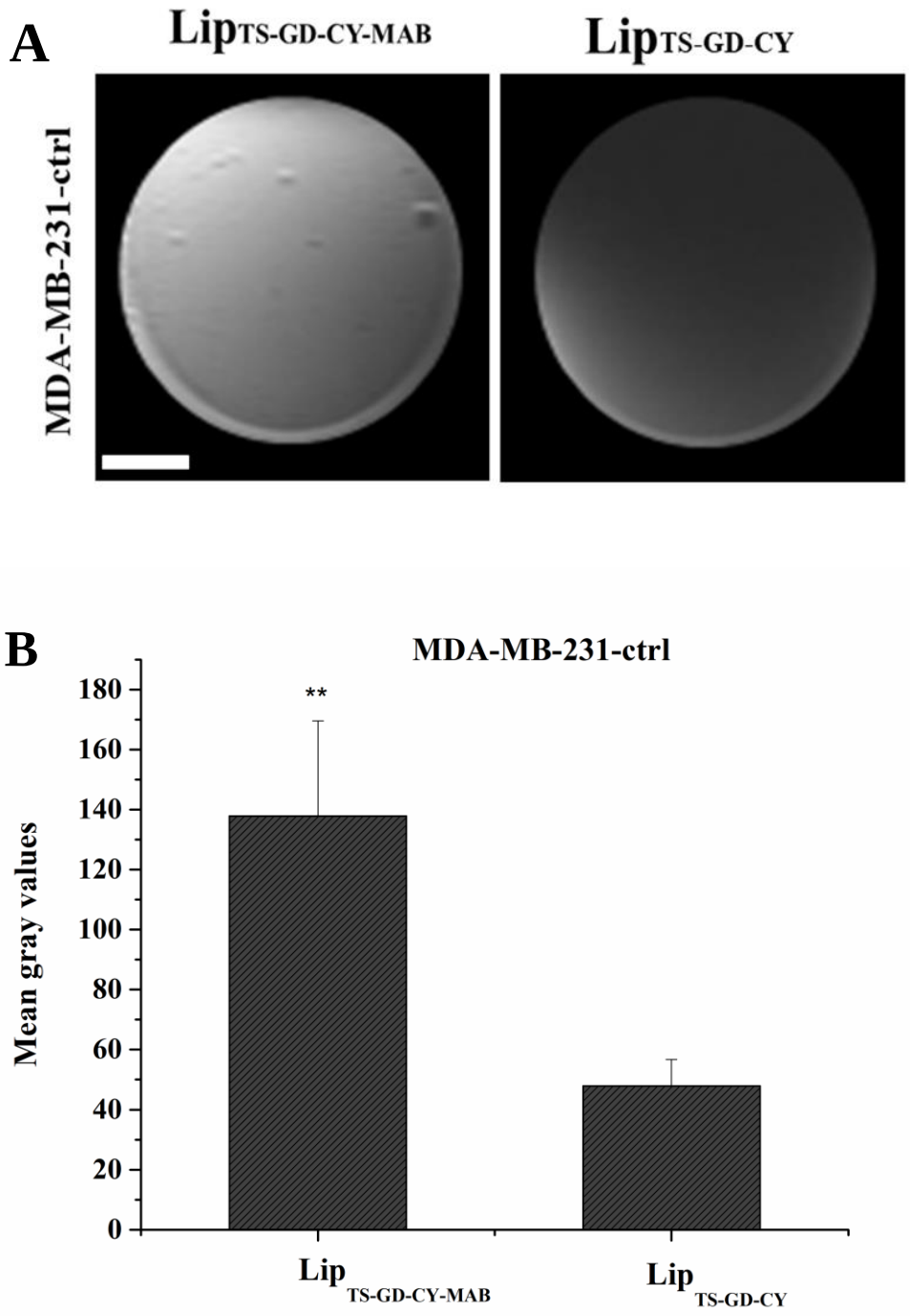

***Figure 31**: Binding efficiency of Lip$_{TS\text{-}GD\text{-}CY\text{-}MAB}$ and Lip$_{TS\text{-}GD\text{-}CY}$ on MDA-MB-23-ctrl cells, under UHF-MRI (A), scale bar represents 4 μm. The mean gray value of the binding efficiency of Lip$_{TS\text{-}GD\text{-}CY\text{-}MAB}$ and Lip$_{TS\text{-}GD\text{-}CY}$ on MDA-MB-231-ctrl cells (B).*

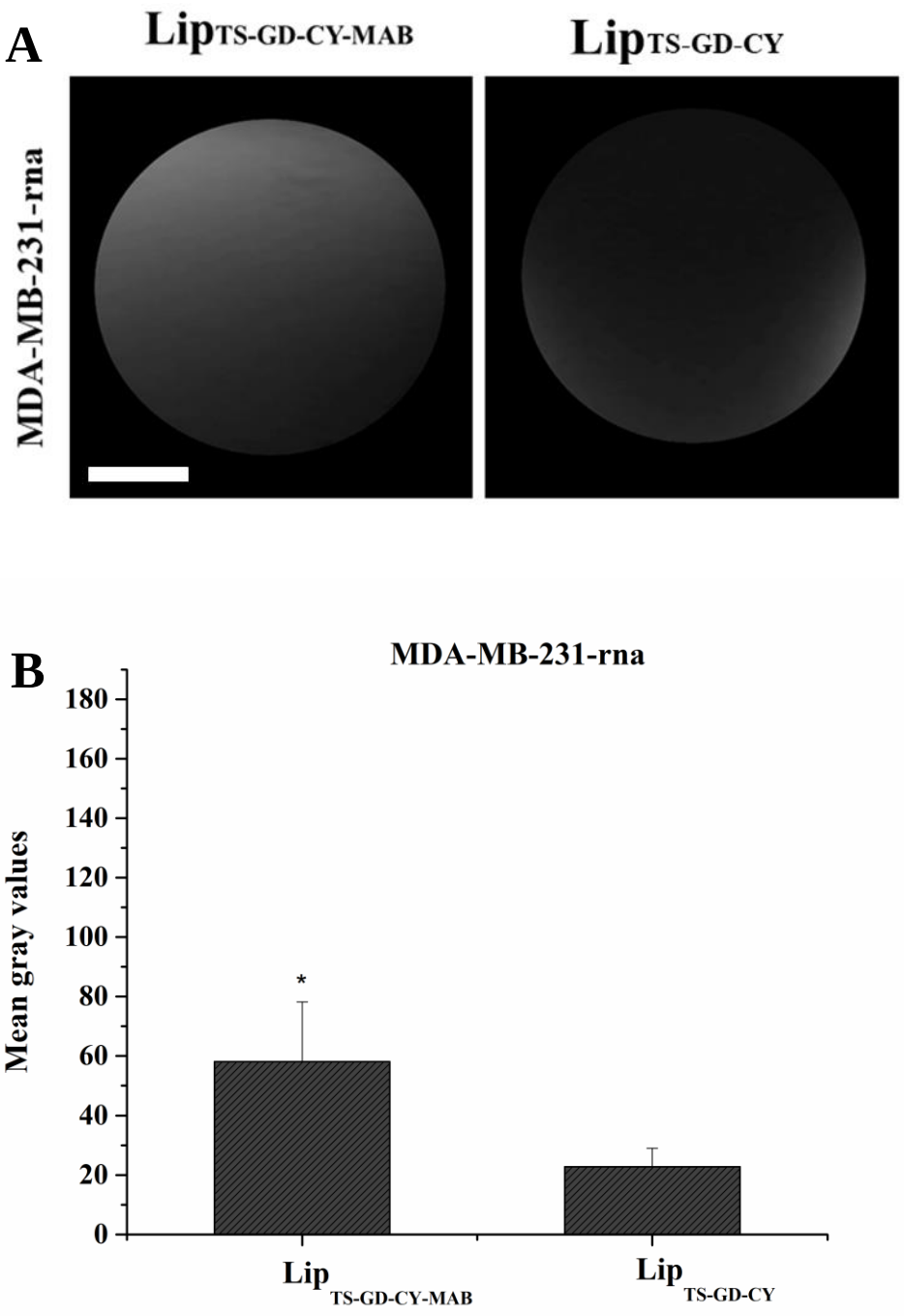

***Figure 32**: Binding efficiency of $Lip_{TS\text{-}GD\text{-}CY\text{-}MAB}$ and $Lip_{TS\text{-}GD\text{-}CY}$ on MDA-MB-23-rna cells, under UHF-MRI, scale bar represents 4 μm (A). The mean gray value of the binding efficiency of $Lip_{TS\text{-}GD\text{-}CY\text{-}MAB}$ and $Lip_{TS\text{-}GD\text{-}CY}$ on MDA-MB-231-rna cells (B).*

3.13. Circulation method

The circulation method represents an approach for mimicking cellular binding while the liposomes are circulating in the bloodstream. NBD-labeled $Lip_{TS\text{-}GD\text{-}CY\text{-}MAB}$ and $Lip_{TS\text{-}GD\text{-}CY}$ were used to detect the binding efficiency of the liposomes using the circulation method. Fluorescence microscopy images of $Lip_{TS\text{-}GD\text{-}CY\text{-}MAB}$ and $Lip_{TS\text{-}GD\text{-}CY}$ depicted that a higher green fluorescence signal was obtained from the MDA-MB-231-ctrl cells incubated with the $Lip_{TS\text{-}GD\text{-}CY\text{-}MAB}$ antibody tagged liposomes (Figure 33A), showing the ligand-specific targeting of the antibody to the cell. However, fluorescence microscopy images obtained after incubating with $Lip_{TS\text{-}GD\text{-}CY\text{-}MAB}$ or $Lip_{TS\text{-}GD\text{-}CY}$ with MDA-MB-231-rna rendered a very slight green fluorescence signal (Figure 34A). Thus demonstrating that the knockdown of ADAM8 in MDA-MB-231-rna cells reduced the targetability of the liposomes. Likewise, high fluorescence intensity serves as an indication of the promising binding, hence cellular internalization, when utilizing these liposomes *in vivo*. It is observed that the $Lip_{TS\text{-}GD\text{-}CY\text{-}MAB}$ tagging played a crucial role in binding with ADAM8 antigens present in MDA-MB-231-ctrl cell line. The results of the quantitative assay exhibited a significant ($p < 0.001$) increase in binding of $Lip_{TS\text{-}GD\text{-}CY\text{-}MAB}$ tagged NBD liposome (Figure 33B). These results support the previously suggested results by Romangoli *et al*.[113], which proclaimed MAB 1031 as a therapeutic target for ADAM8. Moreover, non-significant binding was depicted in MDA-MB-231-rna cells (Figure 34B), the absence of ADAM8 receptor deprived the $Lip_{TS\text{-}GD\text{-}CY\text{-}MAB}$ to specifically target the cells that further confirming the lock key phenomenon of ligand-specific binding.

The results indicate that liposomes obtain high binding capability in a system that mimics blood circulation. This can be a sign of a promising binding for further *in vivo* applications for metastasis, in which blood circulating $Lip_{TS\text{-}GD\text{-}CY\text{-}MAB}$ bind to the circulating metastatic ADAM8 overexpressed malignant tumor cells for further diagnosis (UHF-MRI imaging) and treatment by DOX delivery.

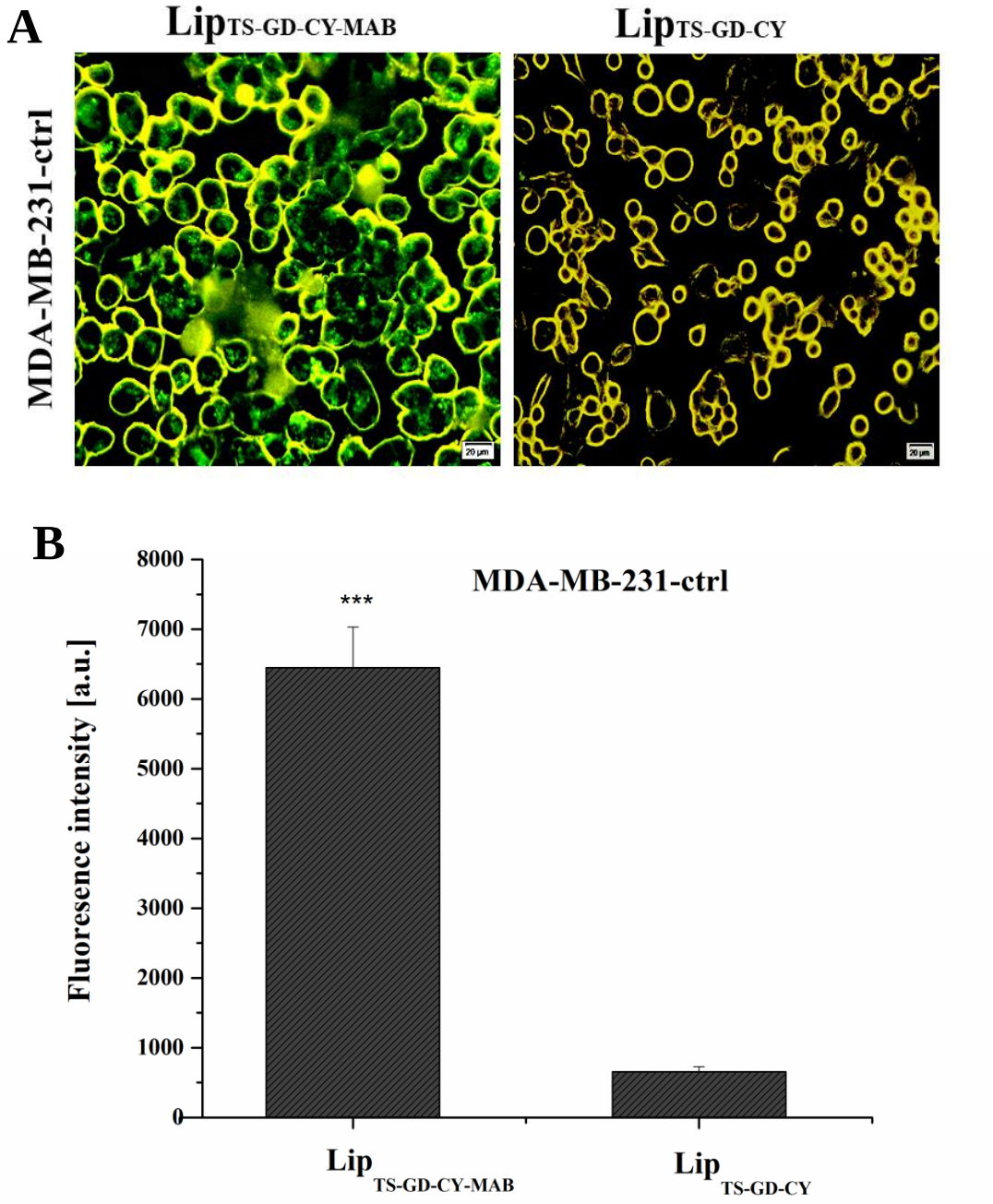

***Figure 33**: Binding efficiency of NBD labeled liposomes $Lip_{TS\text{-}GD\text{-}CY\text{-}MAB}$ and $Lip_{TS\text{-}GD\text{-}CY}$ on MDA-MB-231-ctr (A). Green signals depicting the NBD labeled liposomes. Higher green fluorescence depicting the enhanced cellular binding of the liposomes. Scale bar represents 20 µm. Quantitative determination of binding efficiency of NBD labeled liposomal formulation $Lip_{TS\text{-}GD\text{-}CY\text{-}MAB}$ and $Lip_{TS\text{-}GD\text{-}CY}$ on MDA-MB-231-ctrl cells (B).*

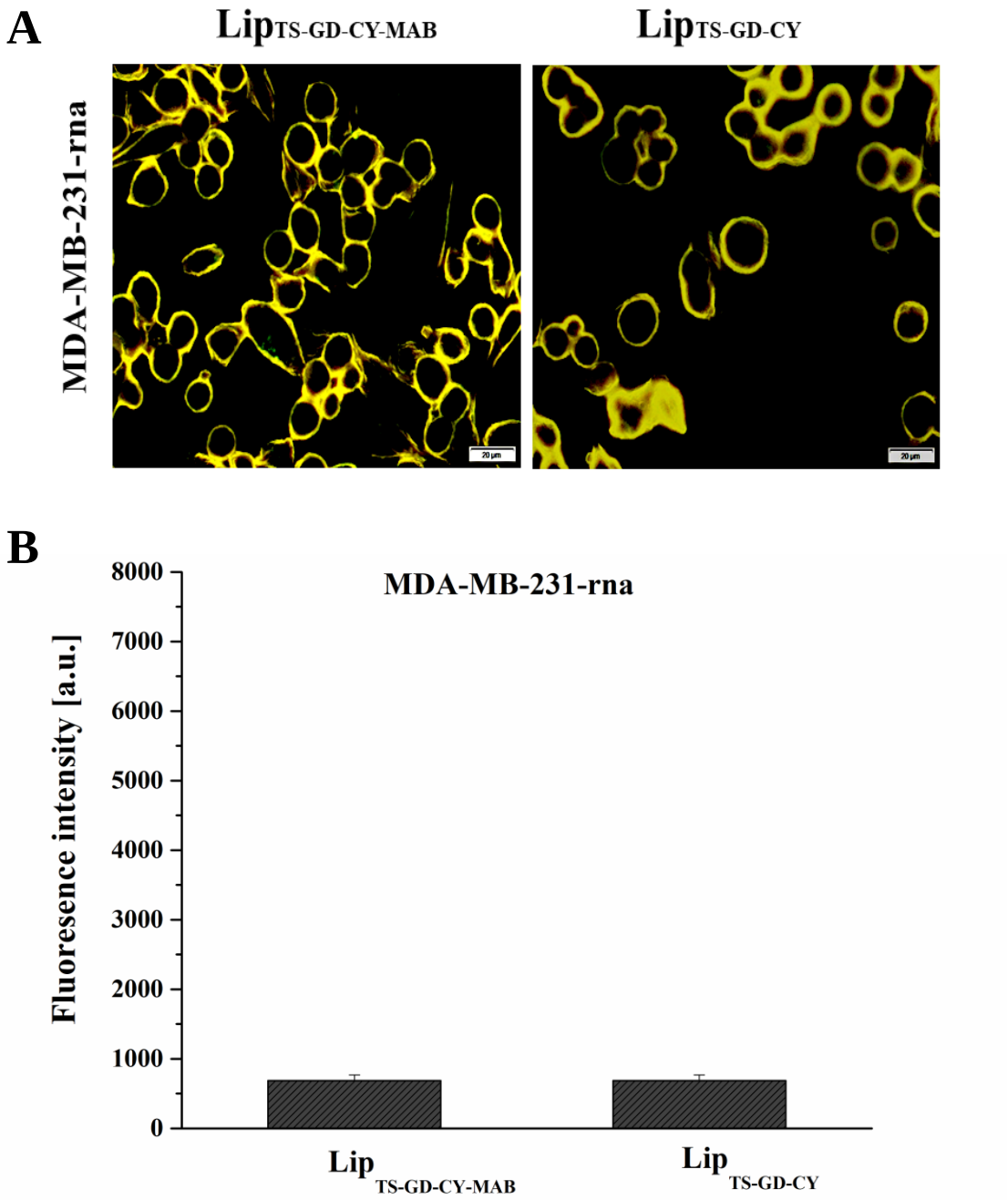

***Figure 34**: Binding efficiency of NBD labeled liposomal formulations $Lip_{TS\text{-}GD\text{-}CY\text{-}MAB}$ and $Lip_{TS\text{-}GD\text{-}CY}$ on MDA-MB-231-rna cells (A). Green signals depicting the NBD labeled liposomes. The green fluorescence depicting the cellular binding of the liposomes. Scale bar represents 20 µm. Quantitative determination of binding efficiency of NBD labeled liposomal formulation $Lip_{TS\text{-}GD\text{-}CY\text{-}MAB}$ and $Lip_{TS\text{-}GD\text{-}CY}$ on MDA-MB-231-rna (B).*

3.14. Hemocompatibility studies

The inherent properties of liposomes increase their tolerability towards the encapsulated drugs, improves the subsequent therapeutic index after their administration as well as provide tolerable pharmaceutical formulations for those drugs which cannot be administrated in conventional approaches [183]. Liposomes are a great nanocarrier to carry and deliver pharmaceutical agents, which is challenging parenterally. This reflects the clinical relevance and importance of evaluating the systematic administration of liposomal formulation and assess their hemocompatibility. Our prepared liposomes are meant for parenteral application to provide long blood circulation times and to deliver DOX to tumor tissues. In order to ensure a high level of safety during this long journey of the prepared liposomes, hemocompatibility studies are of great importance. Blood is a mixture of components. The drug carrier should be compatible with all the blood constitutes. For more understanding of the interaction between the liposomes and the blood components, hemocompatibility studies were carried out. These studies are essential to estimate the liposome's utility and provide a better understanding of the *in vivo* liposomal behavior. Therefore, hemolysis and aPTT tests were carried out of the liposomal formulations.

3.14.1. Hemolysis assay

Hemocompatibility studies could help understand the correlation between *in vitro* and *in vivo* and are as well useful for the determination of safe concentration to be administered in an *in vivo* experiment. Hemolysis assay represents the amount of hemoglobin released from the erythrocytes upon the addition of liposomes. The hemoglobin released from the erythrocytes reacts with atmospheric oxygen, which forms oxyhemoglobin that can be determined spectrophotometrically at 540 nm [184]. 1 % Triton X-100® was used as controls and the absorbance values of Triton X-100® were considered as 100 % hemolysis, due to its complete hemolysis capability [185]. The hemolytic potentials of DOX-Lip$_{TS}$, DOX-Lip$_{TS\text{-}GD}$, Lip$_{TS\text{-}GD\text{-}CY,}$ and Lip$_{TS\text{-}GD\text{-}CY\text{-}MAB}$ were about 5 %. The hemolytic potentials can thus be neglected (Figure 35).

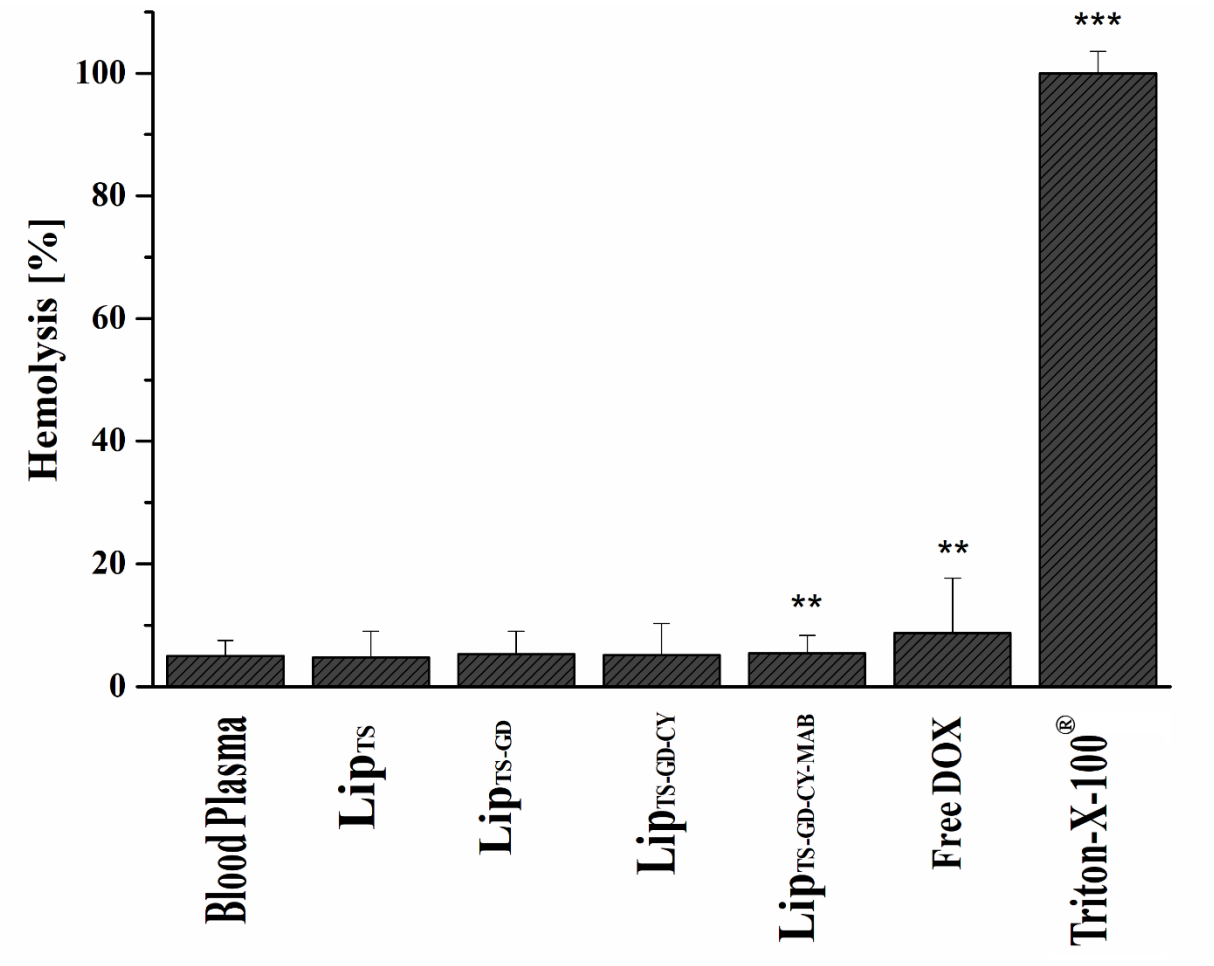

***Figure 35**: Hemolysis assay of Lip_{TS}, $Lip_{TS\text{-}GD}$, $Lip_{TS\text{-}GD\text{-}CY}$, $Lip_{TS\text{-}GD\text{-}CY\text{-}MAB}$ encapsulated DOX at DOX concentration of 1 mg/5 mg lipids, and free DOX at a concentration of 1 mg/ml. Triton X-100® was used as a positive control in hemolysis assay, depending on its ability to lyse the cells. For statistical analysis, the results were compared to fresh blood plasma.*

3.14.2. Activated partial thromboplastin time test

Activated partial thromboplastin time test (aPTT) test was performed to determine the change of the blood coagulation time upon exposure to liposomes. This test donates an *in vitro* test for a better understanding of *in vivo* application. aPTT test gives an insight into the effect of the liposomes on blood coagulation time. Results showed that the coagulation time for blood plasma was 30.4 s. The coagulation time increased to around 37.2 s for DOX-Lip_{TS} and 37.6 s for DOX-$Lip_{TS\text{-}GD}$. In the case of DOX-$Lip_{TS\text{-}GD\text{-}CY}$ and DOX-$Lip_{TS\text{-}GD\text{-}CY\text{-}MAB}$ the coagulation times were 37.5 and 38.4 s, respectively. Free DOX obtained a coagulation time of 50.8 s and these are considered acceptable values for aPTT (Figure 36). An aPTT higher than 70 s implies continuous bleeding leaving the patient with a risk of hemorrhage as reported by Lee *et al.*[145]. These results indicate that the prepared liposomes can be administered intravenously.

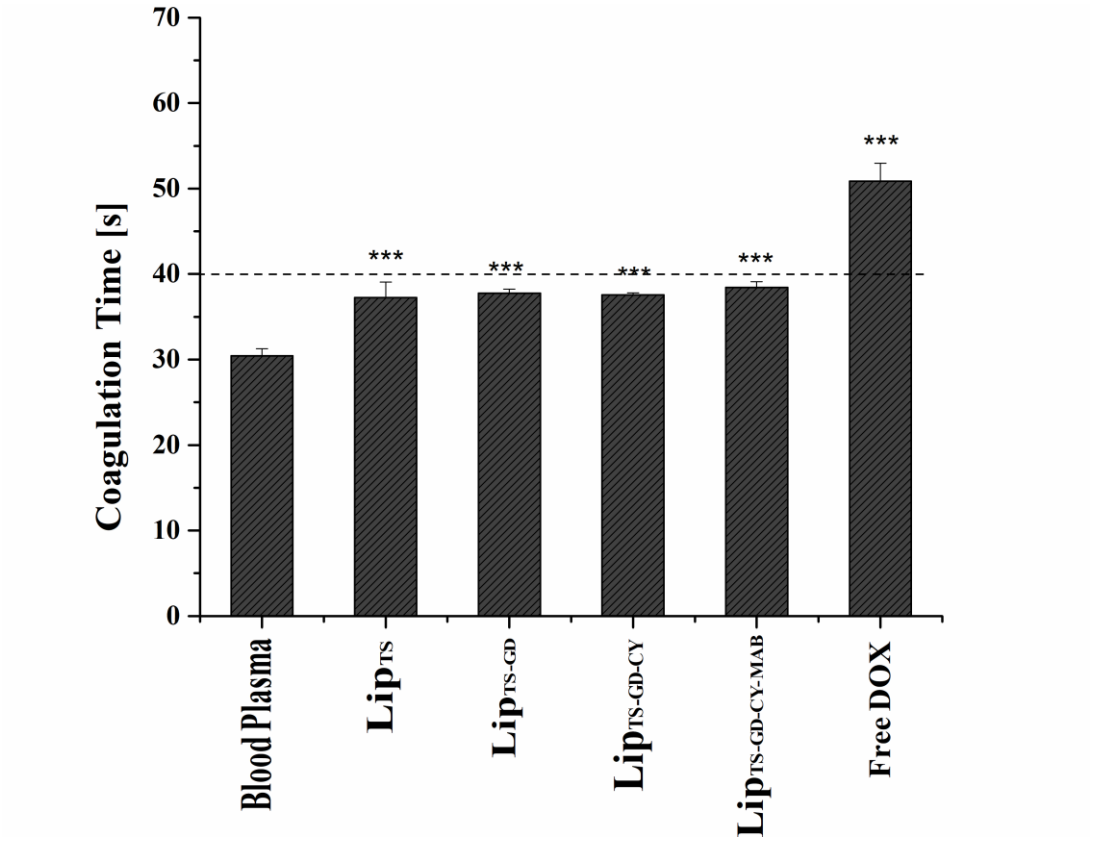

***Figure 36**: aPTT assay of Lip_{TS}, $Lip_{TS\text{-}GD}$, $Lip_{TS\text{-}GD\text{-}CY}$, $Lip_{TS\text{-}GD\text{-}CY\text{-}MAB}$ encapsulated DOX at DOX concentration of 1 mg/5 mg lipids, and free DOX at a concentration of 1 mg/ml. Values between 30 and 40 s are considered acceptable. Blood plasma was used as a control. For statistical analysis, the results were compared to fresh blood plasma.*

3.15. Chorioallantoic membrane

In order to evaluate systemic biocompatibility, liposomes were administered intravenously into chick embryos to assess toxicity due to their systemic exposure [186]. Free DOX, DOX-Lip$_{TS\text{-}GD\text{-}CY}$, and DOX-Lip$_{TS\text{-}GD\text{-}CY\text{-}MAB}$ were injected intravenously on egg development day 11 (EDD 11). The heartbeat and the state of vessel development were monitored and recorded daily until EDD 16 to evaluate the cytotoxic effect of the administered liposomes. Free DOX showed a major cytotoxic effect with chick viability of only 40 % on EDD 16, whereas the chick viability in the case of DOX-Lip$_{TS\text{-}GD\text{-}CY}$ and DOX-Lip$_{TS\text{-}GD\text{-}CY\text{-}MAB}$ was 87 % and 74 %, respectively (Figure 37). The model system of CAM is considered vulnerable, however, it has withstood the liposomal treatment protocol under normal physiological conditions with minimum or no intervention to its physiology, indicating that the liposomes are safe for further *in vivo* experiments. This investigation can be used as a proof of concept that DOX liposomes remained intact at normal physiological temperatures.

In other experiments, Lip$_{TS\text{-}GDCY\text{-}MAB}$ was injected into the chick embryo vasculature on EDD 11 and scanned under UHF-MRI to evaluate the magnetic properties of the liposomes in a biological system with T2-weighted images (3D) (Figure 38). Lip$_{TS\text{-}GD\text{-}CY\text{-}MAB}$ had clear magnetic properties under UHF-MRI and the chick survived the scan. As well as chick embryo showed high viability at 37 °C for 6 days indicating the safety of our nanoscale carrier.

The UHF-MRI offered anatomical information about the chick embryo. UHF-MRI T2-weighted images did not only offer anatomical information and information about embryo development, but it is also a great non-invasive technique to observe and detect the localization of the liposomes in a biological system that offers high-resolution images. On the other hand, UHF-MRI can be used to detect metastatic dissemination. In order to reduce metastasis-related mortality, an early, as well as a selective detection, is required. Metastatic dissemination is a complex process, and once the cells are circulating in the system, their identification is quite difficult [187].

Introducing a nanocarrier that would allow an active targeting selectively to the ADAM8 overexpressing cancer cells, a chemotherapeutic agent as well as an imaging agent that would allow the acquisition of UHF-MRI images. This facilitates the treatment of metastatic cancer as well as offers a deeper understanding of the metastasis dissemination. As a model for imaging mediated delivery of the nanocarrier, imaging the liposomal localization was obtained in a chick embryo. The chick embryo is healthy and no tumor model could be achieved within it.

Therefore, as observed from the contrast, $Lip_{TS\text{-}GD\text{-}CY\text{-}MAB}$ are circulating in the whole body of the chick embryo and is not localized in a specific tumor region. This can be a promising approach to obtain an imagining mediated drug delivery system for the detection and treatment of tumors and metastatic cells.

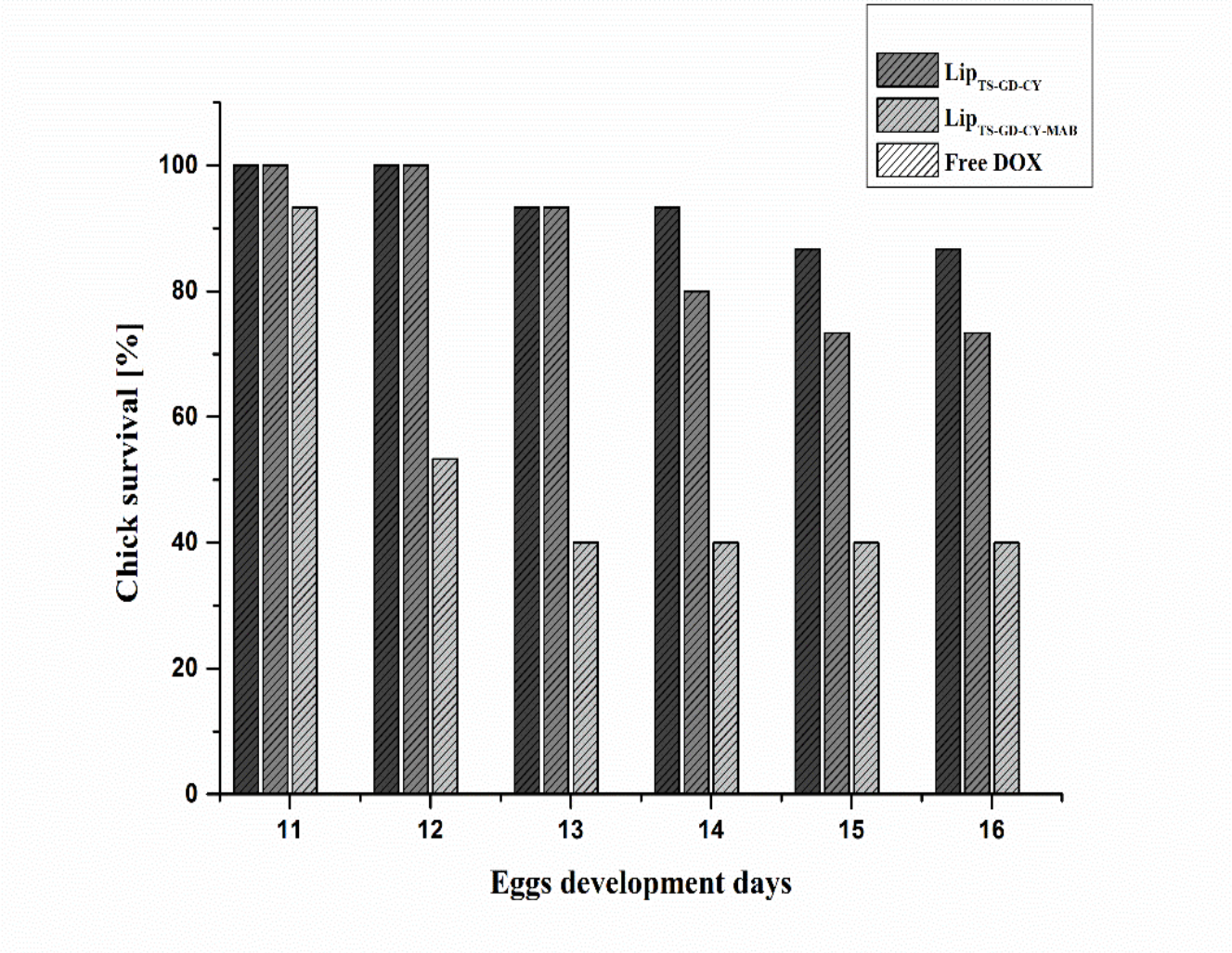

***Figure 37**: Chick embryo viability after injection of DOX-$Lip_{TS\text{-}GD\text{-}CY}$, $Lip_{TS\text{-}GD\text{-}CY\text{-}MAB}$ and free DOX in 15 eggs for each of the samples at normal physiological conditions. Results showed no remarkable toxicity for DOX-liposomes; whereas, free DOX was used as control.*

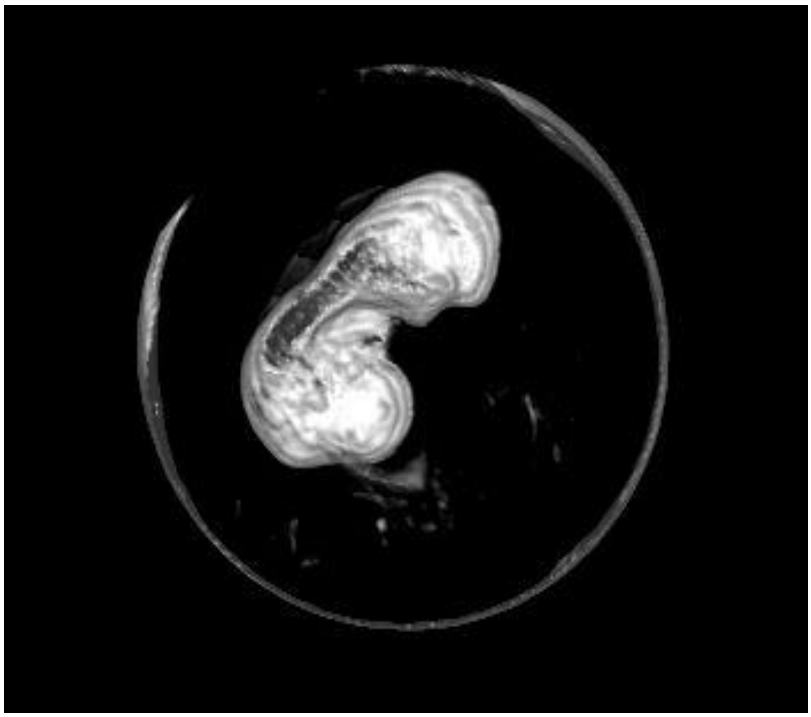

***Figure 38**: T2-weighted 3D image of a living chick embryo after administration of $Lip_{TS\text{-}GD\text{-}CY\text{-}MAB}$ under UHF-MRI.*

4. Summary and outlook

4.1. Summary and outlook

The present work describes the encapsulation of the drug doxorubicin (DOX) in immuno paramagnetic thermosensitive liposomes. DOX is the most common chemotherapeutic agent for the treatment of a variety of carcinomas. However, the pure drug has high cytotoxicity and therefore requires a targeted and biocompatible delivery system.

The introduction includes concepts, modalities, and functionalities of the project. First, a detailed description of the cell type (triple-negative breast cancer) is given. Furthermore, the importance of liposomal doxorubicin is explained and the current state of research is shown. The importance of modification to achieve thermosensitive properties and the procedure for co-encapsulation with Gd chelate to achieve paramagnetic properties is also discussed. In addition, the first part describes the surface modification with ADAM8 antibodies, which leads to improved targeting.

The second part of the thesis covers the different materials and methods used in this paper. The production of the liposomes Lip_{TS}, $Lip_{TS\text{-}GD}$, $Lip_{TS\text{-}GD\text{-}CY}$, $Lip_{TS\text{-}GD\text{-}CY\text{-}MAB}$ and the loading of DOX using an ammonium sulfate gradient method were described in detail.

The results part deals with the physicochemical characterization using dynamic light scattering and laser Doppler velocimetry, which confirmed a uniform monodisperse distribution of the liposomes. These properties facilitate the approach of liposomes to target cancer cells. The influence of lipid composition of liposomes, co-encapsulation with Gd chelate and surface modification of liposomes was evaluated and described accordingly. The size and structure of the individual liposomal formulations were determined by atomic force microscopy and transmission electron microscopy. Morphological examination of the liposomes confirmed agreement with the sizes obtained by dynamic light scattering. Temperature-dependent AFM images showed an intact liposome structure at 37 °C, whereas heating by UHF-MRI led to a lipid film indicating the destruction of the lipid bilayer. Furthermore, TEM images showed the morphological properties of the liposomes and gave a more precise indication of how Gd-chelate accumulates within the liposomes. Liposomes with Gd-chelate showed well-separated vesicles, suggesting that Gd- chelate is deposited in the lipid bilayer of the liposomes. Gd was encapsulated in the hydrophilic core whereas chelate was extended into the lipid bilayer.

By differential scanning calorimetry and drug release, the heat-sensitive functionality of the liposomes could be determined. Liposomes showed a beginning of phase transition temperature

at about 38 °C, which can be achieved by UHF-MRI exposure. The maximum phase transition temperature in the case of $Lip_{TS\text{-}GD}$ and $Lip_{TS\text{-}GD\text{-}CY\text{-}MAB}$ was 42 °C and 40 °C, respectively. A proof of concept study for the thermosensitive properties of liposomes and a time-dependent DOX release profile in hyperthermia was performed.

Gd-chelate is encapsulated in both $Lip_{TS\text{-}GD}$ and $Lip_{TS\text{-}GD\text{-}CY\text{-}MAB}$ and led to paramagnetic properties of the liposomes. This facilitates imaging mediated DOX delivery and diagnosis of the solid tumor and metastatic cells. The change in relaxation rate R1 of liposomes was quantified before and after heating above T_m ($T > T_m$). The relaxivity of the liposomes was obtained from the adapted slope of the relaxation rate against the Gd concentration. Remarkably, the relaxation rate and relaxivity increased after heating the liposomes above T_m ($T > T_m$), suggesting that the liposomes opened, released Gd chelate, and the exchange of water molecules became faster and more practicable.

Toxicity studies describe the different mechanisms for induced DOX toxicity. The increased cytotoxic effect at elevated temperatures showed that the induced toxicity is thermally dependent, i.e. DOX was released from the liposomes. The high viability of the cells at 37 °C indicates that the liposomes were intact at normal physiological temperatures. Under UHF-MRI treatment, cell toxicity due to elevated temperature was observed. The cellular uptake of liposomes under UHF-MRI was followed by a confocal laser scanning microscope. An increase in fluorescence intensity was observed after UHF-MRI exposure. The study of the uptake pathway showed that the majority of liposomes were mainly uptake by clathrin-mediated endocytosis.

In addition, the liposomes were modified with anti-ADAM8 antibodies (MAB 1031) to allow targeted delivery. The cellular binding capabilities of surface-modified and non-modified liposomes were tested on cells that had ADAM8 overexpression and on ADAM8 knockdown cells. Surface-modified liposomes showed a significant increase in binding ability, indicating significant targeting against cells that overexpress ADAM8 on their surface. In addition, cells with knockdown ADAM8 could not bind a significant amount of modified liposomes.

The biocompatibility of liposomes was assessed using a hemolysis test, which showed neglected hemolytic potential and an activated thromboplastin time (aPTT), where liposomes showed minimal interference with blood clotting. Hemocompatibility studies may help to understand the correlation between *in vitro* and *in vivo*.

The chorioallantois model was used *in ovo* to evaluate systematic biocompatibility in an alternative animal model. In the toxicity test, liposomes were injected intravenously into the

chicken embryo. The liposomes showed a neglectable harmful effect on embryo survival. While free DOX has a detrimental effect on the survival of chicken embryos, this confirms the safety profile of liposomes compared to free DOX. $Lip_{TS\text{-}GD\text{-}CY\text{-}MAB}$ were injected into the vascular system of the chicken embryo on egg development day 11 and scanned under UHF-MRI to evaluate the magnetic properties of the liposomes in a biological system with T2-weighted images (3D). The liposomal formulation had distinct magnetic properties under UHF MRI and the chick survived the scan.

In summary, immunomagnetic heat-sensitive liposomes are a novel drug for the treatment of TNBC. It is used both for the diagnosis and therapy of solid and metastasizing tumors without side effects on the neighboring tissue.

Furthermore, a tumor in the CAM model will be established. Thereafter, the selective targeting of the liposomes will be visualized and quantitated using fluorescence and UHF-MRI. Liposomes are yet to be tested on mice as a xenograft triple-negative breast cancer model, in which further investigation on the effect of DOX-$Lip_{TS\text{-}GD\text{-}CY\text{-}MAB}$ is evaluated. On one hand, the liposomes will be evaluated regarding their targetability and their selective binding. On the other hand, the triggered release of DOX from the liposomes after UHF-MRI exposure will be quantitated, as well as evaluate the DOX-Liposomes therapeutic effect on the tumor.

4.2. Zussamenfassung und Ausblick

Die vorliegende Arbeit beschreibt die Verkapselung des Arzneistoffs Doxorubicin (DOX) in immunparamagnetische thermosensitive Liposomen. DOX ist das häufigste Chemotherapeutikum zur Behandlung einer Vielzahl von Karzinomen. Jedoch besitzt der reine Arzneistoff eine hohe Zytotoxizität und erfordert somit ein gezieltes und biokompatibles Trägersystem.

Das einleitende Kapitel dieser Arbeit umfasst Konzepte, Modalitäten und Funktionalitäten des Projektes. Es findet zunächst eine detaillierte Beschreibung des Zelltyps (dreifach-negativer Brustkrebs) statt. Des Weiteren wird die Bedeutung von liposomalem DOX erklärt und der aktuelle Forschungsstand aufgezeigt. Die Bedeutung der Modifikation zur Erzielung der thermosensitiven Eigenschaften und die Vorgehensweise zur Co-Verkapselung mit Gd-Chelat um paramagnetische Eigenschaften zu erreichen wird ebenfalls behandelt. Zudem wird im ersten Teil die Oberflächenmodifikation mit ADAM8-Antikörper beschrieben, was zu einem verbesserten Targeting führt.

Der zweite Teil der Arbeit umfasst die verschiedenen Materialien und Methoden, die in der vorliegende Arbeit zum Einsatz kamen. Die Herstellung der Liposomen Lip_{TS}, $Lip_{TS\text{-}GD}$, $Lip_{TS\text{-}GD\text{-}CY}$, $Lip_{TS\text{-}GD\text{-}CY\text{-}MAB}$ und die Beladung von DOX unter Verwendung eines Ammoniumsulfatgradienten wurden detailliert beschrieben.

Das erste Kapitel des Ergebnisteils behandelt die physikalisch-chemische Charakterisierung mittels dynamischer Lichtstreuung und Laser-Doppler-Velocimetrie, welche eine gleichmäßige monodisperse Verteilung der Liposomen bestätigte. Diese Eigenschaften erleichtern die Annäherung der Liposomen an die Zielkrebszellen. Der Einfluss der Lipidzusammensetzung der Liposomen, der Co-Verkapselung von Gd-Chelat und der Oberflächenmodifikation der Liposomen wurde entsprechend bewertet und beschrieben. Größe und Struktur der einzelnen liposomalen Formulierungen wurden mit Hilfe der Rasterkraftmikroskopie und Transmission-selektronenmikroskopie bestimmt. Die morphologische Untersuchung der Liposomen bestätigte eine Übereinstimmung mit den Größen, die durch dynamische Lichtstreuung erhalten wurden. Temperaturabhängige AFM-Bilder zeigten eine intakte Liposomenstruktur bei 37 °C, wohingegen eine Erhitzung durch UHF-MRI, zu einem Lipidfilm führte, der auf die Zerstörung der Lipiddoppelschicht hinwies. Des Weiteren zeigten TEM-Bilder die morphologischen Eigenschaften der Liposomen und gaben einen genaueren Hinweis wie sich Gd-Chelat innerhalb der Liposomen anlagert. Liposomen mit Gd-Chelat zeigten gut getrennte Vesikel,

was darauf hindeutete, dass sich Gd-Chelat in der Lipiddoppelschicht der Liposomen einlagert. Gd wurde in den hydrophilen Kern der Liposomen vereingekapselt, wohingegen das Gd-chelat in die Lipidmembran ragt.

Durch dynamische Differenzkalorimetrie und temperaturabhängige Arzneimittelfreisetzung konnte die Wärmeempfindlichkeit der Liposomen bestimmt werden. Liposomen zeigten einen Beginn der Phasenübergangstemperatur bei etwa 38 °C, was ebenfalls unter UHF-MRT-Exposition erreicht werden kann. Das Maximum dieser Temperatur lag im Fall von $Lip_{TS\text{-}GD}$ und $Lip_{TS\text{-}GD\text{-}CY\text{-}MAB}$ bei 42 und 40 °C. Eine „Proof-of-Concept-Studie“ für die thermosensitiven Eigenschaften der Liposomen sowie ein zeitabhängiges DOX-Freisetzungsprofil bei Hyperthermie wurde erstellt.

Gd-Chelat ist sowohl in $Lip_{TS\text{-}GD}$ als auch in $Lip_{TS\text{-}GD\text{-}CY\text{-}MAB}$ enthalten und führte daher zu paramagnetischen Eigenschaften dieser Liposomen. Dies ermöglichte die UHF-MRT-vermittelte DOX-Freisetzung sowie die Diagnostik solider Tumore und metastasierender Zellen. Die Änderung der Relaxationsrate R1 der Liposomen wurde vor und nach dem Erhitzen über T_m ($T > T_m$) quantifiziert. Die Relaxivität der Liposomen wurde aus der berechneten Steigung der Relaxationsrate gegen die Gd-Konzentration erhalten. Bemerkenswerterweise erhöhten sich die Relaxationsrate und die Relaxivität nach dem Erhitzen der Liposomen über T_m ($T > T_m$), was darauf hinweist, dass sich die Liposomen öffneten, Gd-Chelat freisetzten und der Austausch von Wassermolekülen schneller und praktikabler wurde.

Toxizitätsstudien beschreiben die verschiedenen Mechanismen für die induzierte DOX-Toxizität. Die stärkere zytotoxische Wirkung bei erhöhten Temperaturen zeigt eine thermisch induzierte Toxizität, d.h. es kam zu einer Freisetzung von DOX aus den Liposomen bei erhöhter Temperatur. Die Überlebensrate der Zellen bei 37 °C deutet darauf hin, dass die Liposomen bei normalen physiologischen Temperaturen intakt waren. Unter UHF-MRT-Behandlung wurde eine Zelltoxizität aufgrund einer erhöhten Temperatur erreicht. Die Verfolgung der zellulären Aufnahme der Liposomen unter UHF-MRT fand mit Hilfe der konfokaler Lasermikroskopie statt. Ein Anstieg der Fluoreszenzintensität wurde nach UHF-MRT-Exposition beobachtet. Die Untersuchung des Aufnahmewegs zeigte, dass die Mehrzahl der Liposomen hauptsächlich durch Clathrin-vermittelte Endozytose aufgenommen wurden.

Darüber hinaus wurden die Liposomen mit Anti-ADAM8-Antikörper (MAB 1031) modifiziert um ein gezieltes Targeting zu ermöglichen. Die zellulären Bindungsfähigkeiten der oberflächenmodifizierten und nicht-modifizierten Liposomen wurden auf Zellen getestet, die eine ADAM8-Überexpression hatten, sowie auf ADAM8-Knockdown-Zellen.

Oberflächenmodifizierte Liposomen zeigten einen signifikanten Anstieg der Bindungsfähigkeiten, was auf ein signifikantes Targeting gegen Zellen hinweist, die ADAM8 auf ihrer Oberfläche überexprimieren. Zusätzlich konnten Zellen mit Knockdown-ADAM8 keine signifikante Menge an modifizierten Liposomen binden.

Die Bewertung der Biokompatibilität der Liposomen wurde unter Verwendung eines Hämolysetests und einer aktivierten Thromboplastinzeit (aPTT) bestimmt. Liposomen zeigten ein vernachlässigbares hämolytisches Potential. Ebenso zeigen aPTT-Studien, dass Liposomen die Blutgerinnung nicht stören. Hämokompatibilitätsstudien können helfen, die Korrelation zwischen *in vitro* und *in vivo* zu verstehen.

Zur bewertung der systemischen Biokompatibilität wurde das *in ovo* Chorioallantoismembranmodell verwendet, das einen alternativen Tierversuch darstellt. Im Toxizitätstest wurden Liposomen intravenös in die Hühnerembryonen injiziert. Die Liposomen zeigten eine vernachlässigbar schädliche Wirkung auf die Entwicklung des Embryos. Während freies DOX einen schädlichen Effekt auf das Überleben der Hühnerembryonen hatte, dies bestätigt das verbesserte Sicherheitsprofil der Liposomen im Vergleich zu freiem DOX. $Lip_{TS\text{-}GD\text{-}CY\text{-}MAB}$ wurden am Eierentwicklungstag 11 in das Gefäßsystem des Hühnerembryos injiziert und unter UHF-MRT gescannt, um die magnetischen Eigenschaften der Liposomen in einem biologischen System mit T2-gewichteten Bildern (3D) zu bewerten. Die liposomale Formulierung hatte erkennbare magnetische Eigenschaften unter UHF-MRT und das Küken überlebte den Scan.

Zusammenfassend lässt sich sagen, dass immunomagnetische wärmeempfindliche Liposomen eine neuartige Arzneiform zur TNBC-Behandlung darstellen könnte. Sie dient sowohl zur Diagnose als auch zur Therapie von soliden und metastasierenden Tumore ohne Nebenwirkungen auf das Nachbargewebe zu haben.

Das weitere Vorgehen besteht darin einen Tumor im CAM-Modell zu etablieren, das selektive Targeting der Liposomen zu visualisieren und mittels Fluoreszenz sowie UHF-MRT zu quantifizieren. Ebenso müssen die Liposomen an Mäusen als dreifach-negatives Brustkrebsmodell im Xenograft-Verfahren getestet werden, um weitere Wirkungen von DOX-$Lip_{TS\text{-}GD\text{-}CY\text{-}MAB}$ zu untersuchen. Zum einen sollen die Liposomen hinsichtlich ihrer Zielbarkeit und ihrer selektiven Bindung bewertet werden. Andererseits wird die ausgelöste Freisetzung von DOX aus den Liposomen nach UHF-MRT-Exposition und die therapeutische Wirkung von DOX-Liposomen auf den Tumor bewertet.

5. Appendix

5.1. References

[1]. Liedke, P. E. R., Reolon, G. K., Kilpp, B., Brunetto, A. L., Roesler, R., & Schwartsmann, G. (2009). Systemic administration of doxorubicin impairs aversively motivated memory in rats. *Pharmacology biochemistry and behavior*, *94*, 239-243.

[2]. Siegel, R. L., Miller, K. D., & Jemal, A. (2019). Cancer statistics, 2019. *CA: A cancer journal for clinicians*, *69*, 7-34.

[3]. D. Schottenfeld, J.F. Fraumeni, Cancer epidemiology and prevention, Oxford University Press, 2009, 100-101.

[4]. WHO | Breast cancer, WHO. (2018).

[5]. Eliyatkın, N., Yalçın, E., Zengel, B., Aktaş, S., & Vardar, E. (2015). Molecular classification of breast carcinoma: from traditional, old-fashioned way to a new age, and a new way. *The journal of breast health*, *11*, 1-11.

[6]. Dawson, S. J., Provenzano, E., & Caldas, C. (2009). Triple negative breast cancers: clinical and prognostic implications. *European journal of cancer*, *45*, 27-40.

[7]. Al-Mahmood, S., Sapiezynski, J., Garbuzenko, O. B., & Minko, T. (2018). Metastatic and triple-negative breast cancer: challenges and treatment options. *Drug delivery and translational research*, *8*(5), 1483-1507.

[8]. Neophytou, C., Boutsikos, P., & Papageorgis, P. (2018). Molecular mechanisms and emerging therapeutic targets of triple-negative breast cancer metastasis. *Frontiers in oncology*, *8*, 1-10.

[9]. Safra, T., Muggia, F., Jeffers, S., Tsao-Wei, D. D., Groshen, S., Lyass, O., & Gabizon, A. (2000). Pegylated liposomal doxorubicin (doxil): reduced clinical cardiotoxicity in patients reaching or exceeding cumulative doses of 500 mg/m2. *Annals of oncology*, *11*, 1029-1033.

[10]. Thirumaran, R., Prendergast, G. C., & Gilman, P. B. (2007). Cytotoxic chemotherapy in clinical treatment of cancer. In *cancer immunotherapy*, 101-116.

[11]. Hilmer, S. N., Cogger, V. C., Muller, M., & Le Couteur, D. G. (2004). The hepatic pharmacokinetics of doxorubicin and liposomal doxorubicin. *Drug metabolism and disposition*, *32*, 794-799.

[12]. Carvalho, C., Santos, R. X., Cardoso, S., Correia, S., Oliveira, P. J., Santos, M. S., & Moreira, P. I. (2009). Doxorubicin: the good, the bad and the ugly effect. *Current medicinal chemistry*, *16*, 3267-3285.

[13]. Wang, S., Wang, Y., Zhang, Z., Liu, Q., & Gu, J. (2017). Cardioprotective effects of fibroblast growth factor 21 against doxorubicin-induced toxicity via the SIRT1/LKB1/AMPK pathway. *Cell death & disease*, *8*, 1-13.

[14]. Gewirtz, D. (1999). A critical evaluation of the mechanisms of action proposed for the antitumor effects of the anthracycline antibiotics adriamycin and daunorubicin. *Biochemical pharmacology*, *57*, 727-741.

[15]. Thorn, C. F., Oshiro, C., Marsh, S., Hernandez-Boussard, T., McLeod, H., Klein, T. E., & Altman, R. B. (2011). Doxorubicin pathways: pharmacodynamics and adverse effects. *Pharmacogenetics and genomics*, *21*, 440.

[16]. Rafiyath, S. M., Rasul, M., Lee, B., Wei, G., Lamba, G., & Liu, D. (2012). Comparison of safety and toxicity of liposomal doxorubicin vs. conventional anthracyclines: a meta-analysis. *Experimental hematology & oncology*, *1*, 1-10.

[17]. Hobbs, S. K., Monsky, W. L., Yuan, F., Roberts, W. G., Griffith, L., Torchilin, V. P., & Jain, R. K. (1998). Regulation of transport pathways in tumor vessels: role of tumor type and microenvironment. *Proceedings of the national academy of sciences*, *95*, 4607-4612.

[18]. Yuan, F., Dellian, M., Fukumura, D., Leunig, M., Berk, D. A., Torchilin, V. P., & Jain, R. K. (1995). Vascular permeability in a human tumor xenograft: molecular size dependence and cutoff size. *Cancer research*, *55*, 3752-3756.

[19]. Maeda, H., Wu, J., Sawa, T., Matsumura, Y., & Hori, K. (2000). Tumor vascular permeability and the EPR effect in macromolecular therapeutics: a review. *Journal of controlled release*, *65*, 271-284.

[20]. Lasic, D. D., Martin, F. J., Gabizon, A., Huang, S. K., & Papahadjopoulos, D. (1991). Sterically stabilized liposomes: a hypothesis on the molecular origin of the extended circulation times. *Biochimica et biophysica acta (BBA)-biomembranes*, *1070*, 187-192.

[21]. Torchilin, V. P. (2010). Passive and active drug targeting: drug delivery to tumors as an example. *Drug delivery*, 19, 3-53.

[22]. Bangham, A. D., Standish, M. M., & Watkins, J. C. (1965). Diffusion of univalent ions across the lamellae of swollen phospholipids. *Journal of molecular biology*, *13*, 238-245.

[23]. Gregoriadis, G., Leathwood, P. D., & Ryman, B. E. (1971). Enzyme entrapment in liposomes. *FEBS letters*, *14*, 95-99.

[24]. Gregoriadis, G., & Ryman, B. E. (1972). Fate of protein-containing liposomes injected into rats: an approach to the treatment of storage diseases. *European journal of biochemistry*, *24*, 485-491.

[25]. Akbarzadeh, A., Rezaei-Sadabady, R., Davaran, S., Joo, S. W., Zarghami, N., Hanifehpour, Y., & Nejati-Koshki, K. (2013). Liposome: classification, preparation, and applications. *Nanoscale research letters*, *8*, 102-108.

[26]. Cevc, G. (2012). Rational design of new product candidates: the next generation of highly deformable bilayer vesicles for noninvasive, targeted therapy. *Journal of controlled release*, *160*, 135-146.

[27]. Shek, P. N., Yung, B. Y., & Stanacev, N. Z. (1983). Comparison between multilamellar and unilamellar liposomes in enhancing antibody formation. *Immunology*, *49*, 37-44.

[28]. Sharma Vijay, K., Mishra, D., Sharma, A., & Srivastava, B. (2010). Liposomes: present prospective and future challenges. *International journal of current pharmaceutical review & research*, *1*, 6-16.

[29]. Harris, L., Batist, G., Belt, R., Rovira, D., Navari, R., Azarnia, N., & TLC D-99 Study Group. (2002). Liposome-encapsulated doxorubicin compared with conventional doxorubicin in a randomized multicenter trial as first-line therapy of metastatic breast carcinoma. *Cancer*, *94*, 25-36.

[30]. Xing, H., Hwang, K., & Lu, Y. (2016). Recent developments of liposomes as nanocarriers for theranostic applications. *Theranostics*, *6*, 1336-1345.

[31]. Maherani, B., Arab-Tehrany, E., R Mozafari, M., Gaiani, C., & Linder, M. (2011). Liposomes: a review of manufacturing techniques and targeting strategies. *Current nanoscience*, *7*, 436-452.

[32]. Batzri, S., & Korn, E. D. (1973). Single bilayer liposomes prepared without sonication. *Biochimica et biophysica acta (BBA)-biomembranes*, *298*, 1015-1019.

[33]. Lasic, D. D. (1995). Mechanisms of liposome formation. *Journal of liposome research*, *5*, 431-441.

[34]. Szoka, F., & Papahadjopoulos, D. (1978). Procedure for preparation of liposomes with large internal aqueous space and high capture by reverse-phase evaporation. *Proceedings of the national academy of sciences*, *75*, 4194-4198.

[35]. Enoch, H. G., & Strittmatter, P. (1979). Formation and properties of 1000-A-diameter, single-bilayer phospholipid vesicles. *Proceedings of the national academy of sciences*, *76*, 145-149.

[36]. Milsmann, M. H., Schwendener, R. A., & Weder, H. G. (1978). The preparation of large single bilayer liposomes by a fast and controlled dialysis. *Biochimica et biophysica acta -biomembranes*, *512*, 147-155.

[37]. Bangham, A. D., De Gier, J., & Greville, G. D. (1967). Osmotic properties and water permeability of phospholipid liquid crystals. *Chemistry and physics of lipids*, *1*, 225-246.

[38]. Kim, S., Jacobs, R. E., & White, S. H. (1985). Preparation of multilamellar vesicles of defined size-distribution by solvent-spherule evaporation. *Biochimica et biophysica acta -biomembranes*, *812*, 793-801.

[39]. Payne, N. I., Ambrose, C. V., Timmins, P., Ward, M. D., & Ridgway, F. (1986). Proliposomes: a novel solution to an old problem. *Journal of pharmaceutical sciences*, *75*, 325-329.

[40]. Zhang, H. (2017). Thin-film hydration followed by extrusion method for liposome preparation. In *Liposomes* (17-22). Humana Press, New York, NY.

[41]. Çağdaş, M., Sezer, A. D., & Bucak, S. (2014). Liposomes as potential drug carrier systems for drug delivery. In *Application of nanotechnology in drug delivery*. IntechOpen.

[42]. O'Shaughnessy, J. (2003). Liposomal anthracyclines for breast cancer: overview. *The oncologist*, *8*, 1-2.

[43]. Gabizon, A., Dagan, A., Goren, D., Barenholz, Y., & Fuks, Z. (1982). Liposomes as *in vivo* carriers of adriamycin: reduced cardiac uptake and preserved antitumor activity in mice. *Cancer research*, *42*, 4734-4739.

[44]. Bolotin, E. M., Cohen, R., Bar, L. K., Emanuel, N., Ninio, S., Barenholz, Y., & Lasic, D. D. (1994). Ammonium sulfate gradients for efficient and stable remote loading of amphipathic weak bases into liposomes and ligandoliposomes. *Journal of liposome research*, *4*, 455-479.

[45]. Haran, G., Cohen, R., Bar, L. K., & Barenholz, Y. (1993). Transmembrane ammonium sulfate gradients in liposomes produce efficient and stable entrapment of amphipathic weak bases. *Biochimica et biophysica acta -biomembranes*, *1151*, 201-215.

[46]. Lasic, D. D., Frederik, P. M., Stuart, M. C. A., Barenholz, Y., & McIntosh, T. J. (1992). Gelation of liposome interior A novel method for drug encapsulation. *FEBS letters*, *312*, 255-258.

[47]. Gabizon, A., Catane, R., Uziely, B., Kaufman, B., Safra, T., Cohen, R., & Barenholz, Y. (1994). Prolonged circulation time and enhanced accumulation in malignant exudates of doxorubicin encapsulated in polyethylene-glycol coated liposomes. *Cancer research*, *54*, 987-992.

[48]. Harrington, K. J., Mohammadtaghi, S., Uster, P. S., Glass, D., Peters, A. M., Vile, R. G., & Stewart, J. S. W. (2001). Effective targeting of solid tumors in patients with locally advanced cancers by radiolabeled pegylated liposomes. *Clinical cancer research*, *7*, 243-254.

[49]. Bertrand, N., Simard, P., & Leroux, J. C. (2010). Serum-stable, long-circulating, pH-sensitive PEGylated liposomes. In *Liposomes* (545-558). Humana Press.

[50]. Sterpetti, P., Marucci, L., Candelaresi, C., Toksoz, D., Alpini, G., Ugili, L., & Benedetti, A. (2006). Cell proliferation and drug resistance in hepatocellular carcinoma are modulated by Rho GTPase signals. *American journal of physiology-gastrointestinal and liver physiology*, *290*, G624-G632.

[51]. Uster, P. S., Working, P. K., & Vaage, J. (1998). Pegylated liposomal doxorubicin (Doxil®, Caelyx®) distribution in tumour models observed with confocal laser scanning microscopy. *International journal of pharmaceutics*, *162*, 77-86.

[52]. Yatvin, M. B., Weinstein, J. N., Dennis, W. H., & Blumenthal, R. (1978). Design of liposomes for enhanced local release of drugs by hyperthermia. *Science*, *202*, 1290-1293.

[53]. Gaber, M. H., Hong, K., Huang, S. K., & Papahadjopoulos, D. (1995). Thermosensitive sterically stabilized liposomes: formulation and *in vitro* studies on mechanism of doxorubicin release by bovine serum and human plasma. *Pharmaceutical research*, *12*, 1407-1416.

[54]. Yatvin, M. B., Kreutz, W., Horwitz, B. A., & Shinitzky, M. (1980). pH-sensitive liposomes: possible clinical implications. *Science*, *210*, 1253-1255.

[55]. Al-Ahmady, Z. S., Al-Jamal, W. T., Bossche, J. V., Bui, T. T., Drake, A. F., Mason, A. J., & Kostarelos, K. (2012). Lipid–peptide vesicle nanoscale hybrids for triggered drug release by mild hyperthermia *in vitro* and *in vivo*. *ACS nano*, *6*, 9335-9346.

[56]. Lindner, L. H., Reinl, H. M., Schlemmer, M., Stahl, R., & Peller, M. (2005). Paramagnetic thermosensitive liposomes for MR-thermometry. *International journal of hyperthermia*, *21*, 575-588.

[57]. Needham, D., Anyarambhatla, G., Kong, G., & Dewhirst, M. W. (2000). A new temperature-sensitive liposome for use with mild hyperthermia: characterization and testing in a human tumor xenograft model. *Cancer research*, *60*, 1197-1201.

[58]. Chen, Q., Tong, S., Dewhirst, M. W., & Yuan, F. (2004). Targeting tumor microvessels using doxorubicin encapsulated in a novel thermosensitive liposome. *Molecular cancer therapeutics*, *3*, 1311-1317.

[59]. Chen, W., Duša, F., Witos, J., Ruokonen, S. K., & Wiedmer, S. K. (2018). Determination of the main phase transition temperature of phospholipids by nanoplasmonic sensing. *Scientific reports*, *8*, 14815-14820.

[60]. M.D. Houslay, K.K. Stanley, Dynamics of biological membranes : influence on synthesis, structure, and function, Wiley, 1982 (201-202).

[61]. Wendlandt P.K.G. W.W., Thermal characterization of polymeric materials, Elsevier, New York, Paris, London, Tokyo, Toronto, 1981.

[62]. Teotia, A. K., Sami, H., & Kumar, A. (2015). Thermo-responsive polymers: structure and design of smart materials. In *Switchable and responsive surfaces and materials for biomedical applications* (3-43). Woodhead Publishing.

[63]. Chen, H., Zeng, X., Tham, H. P., Phua, S. Z. F., Cheng, W., Zeng, W., & Zhao, Y. (2019). NIR-light-activated combination therapy with a precise ratio of photosensitizer and prodrug using a host–guest strategy. *Angewandte chemie*, *131*, 7723-7728.

[64]. Kheirolomoom, A., Lai, C. Y., Tam, S. M., Mahakian, L. M., Ingham, E. S., Watson, K. D., & Ferrara, K. W. (2013). Complete regression of local cancer using temperature-sensitive liposomes combined with ultrasound-mediated hyperthermia. *Journal of controlled release*, *172*, 266-273.

[65]. De Smet, M., Langereis, S., van den Bosch, S., & Grüll, H. (2010). Temperature-sensitive liposomes for doxorubicin delivery under MRI guidance. *Journal of controlled release*, *143*, 120-127.

[66]. Caride, V. J., Sostman, H. D., Winchell, R. J., & Gore, J. C. (1984). Relaxation enhancement using liposomes carrying paramagnetic species. *Magnetic resonance imaging*, *2*, 107-112.

[67]. Caride, V. J. (1985). Liposomes as carriers of imaging agents. *Critical reviews in therapeutic drug carrier systems*, *1*, 121-153.

[68]. Frich, L., Bjørnerud, A., Fossheim, S., Tillung, T., & Gladhaug, I. (2004). Experimental application of thermosensitive paramagnetic liposomes for monitoring magnetic resonance imaging guided thermal ablation. *Magnetic resonance in medicine: an official journal of the international society for magnetic resonance in medicine*, *52*, 1302-1309.

[69]. Merino, M., Zalba, S., & Garrido, M. J. (2018). Immunoliposomes in clinical oncology: state of the art and future perspectives. *Journal of controlled release*, *275*, 162-176.

[70]. Waldmann, T. A. (1991). Monoclonal antibodies in diagnosis and therapy. *Science*, *252*, 1657-1662.

[71]. Allen, T. M., Agrawal, A. K., Ahmad, I., Hansen, C. B., & Zalipsky, S. (1994). Antibody-mediated targeting of long-circulating (Stealth^{R}) liposomes. *Journal of liposome research*, *4*, 1-25.

[72]. Chua, M. M., Fan, S. T., & Karush, F. (1984). Attachment of immunoglobulin to liposomal membrane via protein carbohydrate. *Biochimica et biophysica acta (BBA)-general subjects*, *800*, 291-300.

[73]. Heath, T. D. (1987). [10] Covalent attachment of proteins to liposomes. In *Methods in enzymology 149*,111-119.

[74]. Loughrey, H. C., Choi, L. S., Cullis, P. R., & Bally, M. B. (1990). Optimized procedures for the coupling of proteins to liposomes. *Journal of immunological methods*, *132*(1), 25-35.

[75]. Bendas, G., Krause, A., Bakowsky, U., Vogel, J., & Rothe, U. (1999). Targetability of novel immunoliposomes prepared by a new antibody conjugation technique. *International journal of pharmaceutics*, *181*(1), 79-93.

[76]. Lauterber, P. C. (1974). Image formation by induced local interactions: examples employing nuclear magnetic resonance. *Nature*, *246*, 469-475.

[77]. Garroway, A. N., Grannell, P. K., & Mansfield, P. (1974). Image formation in NMR by a selective irradiative process. *Journal of physics c: solid state physics*, *7*, 457-462.

[78]. Mansfield, P., & Maudsley, A. A. (1977). Planar spin imaging by NMR. *Journal of magnetic resonance (1969)*, *27*, 101-119.

[79]. Edelstein, W. A., Hutchison, J. M., Johnson, G., & Redpath, T. (1980). Spin warp NMR imaging and applications to human whole-body imaging. *Physics in medicine & biology*, *25*, 751-756.

[80]. Tsai, L. L., Grant, A. K., Mortele, K. J., Kung, J. W., & Smith, M. P. (2015). A practical guide to MR imaging safety: what radiologists need to know. *Radiographics*, *35*, 1722-1737.

[81]. Hendee, W. R., & Morgan, C. J. (1984). Magnetic resonance imaging part I—physical principles. *Western journal of medicine*, *141*, 491.

[82]. Barnaal, D. E., & Lowe, I. J. (1968). Proton spin–lattice relaxation in hexagonal ice. *The Journal of chemical physics*, *48*, 4614-4618.

[83]. Bottomley, P. A., Foster, T. H., Argersinger, R. E., & Pfeifer, L. M. (1984). A review of normal tissue hydrogen NMR relaxation times and relaxation mechanisms from 1–100

MHz: dependence on tissue type, NMR frequency, temperature, species, excision, and age. *Medical physics*, *11*, 425-448.

[84]. Bloch, F. (1946). Nuclear induction. *Physical review*, *70*, 460-465.

[85]. De Graaf, R. A., Brown, P. B., McIntyre, S., Nixon, T. W., Behar, K. L., & Rothman, D. L. (2006). High magnetic field water and metabolite proton T1 and T2 relaxation in rat brain *in vivo*. *Magnetic resonance in medicine: An official journal of the international society for magnetic resonance in medicine*, *56*, 386-394.

[86]. Bloembergen, N., Purcell, E. M., & Pound, R. V. (1948). Relaxation effects in nuclear magnetic resonance absorption. *Physical review*, *73*, 679-712.

[87]. Solomon, I. (1955). Relaxation processes in a system of two spins. *Physical Review*, *99*, 559.

[88]. Zhen, Z., & Xie, J. (2012). Development of manganese-based nanoparticles as contrast probes for magnetic resonance imaging. *Theranostics*, *2*, 45-51.

[89]. Nakamura, H., Ito, N., Kotake, F., Mizokami, Y., & Matsuoka, T. (2000). Tumor-detecting capacity and clinical usefulness of SPIO-MRI in patients with hepatocellular carcinoma. *Journal of gastroenterology*, *35*, 849-855.

[90]. Taylor, R. M., Huber, D. L., Monson, T. C., Ali, A. M. S., Bisoffi, M., & Sillerud, L. O. (2011). Multifunctional iron platinum stealth immunomicelles: targeted detection of human prostate cancer cells using both fluorescence and magnetic resonance imaging. *Journal of nanoparticle research*, *13*, 4717-4729.

[91]. Xiao, Y. D., Paudel, R., Liu, J., Ma, C., Zhang, Z. S., & Zhou, S. K. (2016). MRI contrast agents: classification and application. *International journal of molecular medicine*, *38*, 1319-1326.

[92]. Laine, M., Arjamaa, O., Vuolteenaho, O., Ruskoaho, H., & Weckström, M. (1994). Block of stretch-activated atrial natriuretic peptide secretion by gadolinium in isolated rat atrium. *The Journal of physiology*, *480*, 553-561.

[93]. Ramalho, J., Semelka, R. C., Ramalho, M., Nunes, R. H., AlObaidy, M., & Castillo, M. (2016). Gadolinium-based contrast agent accumulation and toxicity: an update. *American journal of neuroradiology*, *37*, 1192-1198.

[94]. Agarwal, R., Brunelli, S. M., Williams, K., Mitchell, M. D., Feldman, H. I., & Umscheid, C. A. (2008). Gadolinium-based contrast agents and nephrogenic systemic fibrosis: a systematic review and meta-analysis. *Nephrology dialysis transplantation*, *24*, 856-863.

[95]. Perazella, M. A. (2008). Gadolinium-contrast toxicity in patients with kidney disease: nephrotoxicity and nephrogenic systemic fibrosis. *Current drug safety*, *3*, 67-75.

[96]. Rohrer, M., Bauer, H., Mintorovitch, J., Requardt, M., & Weinmann, H. J. (2005). Comparison of magnetic properties of MRI contrast media solutions at different magnetic field strengths. *Investigative radiology*, *40*, 715-724.

[97]. Mikhail, A. S., Partanen, A., Yarmolenko, P., Venkatesan, A. M., & Wood, B. J. (2015). Magnetic resonance-guided drug delivery. *Magnetic resonance imaging clinics*, *23*, 643-655.

[98]. Taylor, D. G., & Bushell, M. C. (1985). The spatial mapping of translational diffusion coefficients by the NMR imaging technique. *Physics in medicine & biology*, *30*, 345.

[99]. Ojha, T., Rizzo, L., Storm, G., Kiessling, F., & Lammers, T. (2015). Image-guided drug delivery: preclinical applications and clinical translation. Expert Opin. *Drug delivery. 12*, 1203–1207.

[100]. Fatehi, D., Zee, J. V. D., Bruijne, M. D., Franckena, M., & Rhoon, G. C. V. (2007). RF-power and temperature data analysis of 444 patients with primary cervical cancer: deep hyperthermia using the Sigma-60 applicator is reproducible. *International journal of hyperthermia*, *23*, 623-643.

[101]. Juang, T., Stauffer, P. R., Neuman, D. G., & Schlorff, J. L. (2006). Multilayer conformal applicator for microwave heating and brachytherapy treatment of superficial tissue disease. *International journal of hyperthermia*, *22*, 527-544.

[102]. Mcnichols, R. J., Kangasniemi, M., Gowda, A., Bankson, J. A., Price, R. E., & Hazle, J. D. (2004). Technical developments for cerebral thermal treatment: water-cooled diffusing laser fibre tips and temperature-sensitive MRI using intersecting image planes. *International journal of hyperthermia*, *20*, 45-56.

[103]. Yang, Q. X., Wang, J., Zhang, X., Collins, C. M., Smith, M. B., Liu, H., & Chen, W. (2002). Analysis of wave behavior in lossy dielectric samples at high field. *Magnetic resonance in medicine: an official journal of the international society for magnetic resonance in medicine*, *47*, 982-989.

[104]. Kim, M. S. (2016). Investigation of factors affecting body temperature changes during routine clinical head magnetic resonance imaging. *Iranian journal of radiology*, *13*, 1-6.

[105]. Van den Brink, J. S. (2019). Thermal Effects Associated with RF Exposures in Diagnostic MRI: Overview of Existing and Emerging Concepts of Protection. *Concepts in magnetic resonance part b*, *2019*, 5-11.

[106]. Van Lier, A. L., Kotte, A. N., Raaymakers, B. W., Lagendijk, J. J., & van den Berg, C. A. (2012). Radiofrequency heating induced by 7T head MRI: thermal assessment using discrete vasculature or pennes' bioheat equation. *Journal of magnetic resonance imaging*, *35*, 795-803.

[107]. Yoshida, S., Setoguchi, M., Higuchi, Y., Akizuki, S. I., & Yamamoto, S. (1990). Molecular cloning of cDNA encoding MS2 antigen, a novel cell surface antigen strongly expressed in murine monocytic lineage. *International immunology*, *2*, 585-591.

[108]. Koller, G., Schlomann, U., Golfi, P., Ferdous, T., Naus, S., & Bartsch, J. W. (2009). ADAM8/MS2/CD156, an emerging drug target in the treatment of inflammatory and invasive pathologies. *Current pharmaceutical design*, *15*, 2272-2281.

[109]. Schlomann, U., Wildeboer, D., Webster, A., Antropova, O., Zeuschner, D., Knight, C. G., & Bartsch, J. W. (2002). The metalloprotease disintegrin ADAM8 processing by autocatalysis is required for proteolytic activity and cell adhesion. *Journal of biological chemistry*, *277*, 48210-48219.

[110]. Rao, H., Lu, G., Kajiya, H., Garcia-Palacios, V., Kurihara, N., Anderson, J., & Choi, S. J. (2006). α9β1: a novel osteoclast integrin that regulates osteoclast formation and function. *Journal of bone and mineral research*, *21*, 1657-1665.

[111]. K. Kelly, G. Hutchinson, D. Nebenius-Oosthuizen, A.J.H. Smith, J.W. Bartsch, K. Horiuchi, A. Rittger, K. Manova, A.J.P. Docherty, C.P. Blobel, Metalloprotease-disintegrin ADAM8: expression analysis and targeted deletion in mice., Dev. Dyn. *232*, 221–231.

[112]. Bartsch, J. W., Wildeboer, D., Koller, G., Naus, S., Rittger, A., Moss, M. L., & Jockusch, H. (2010). Tumor necrosis factor-α (TNF-α) regulates shedding of TNF-α receptor 1 by the metalloprotease-disintegrin ADAM8: evidence for a protease-regulated feedback loop in neuroprotection. *Journal of neuroscience*, *30*, 12210-12218.

[113]. Romagnoli, M., Mineva, N. D., Polmear, M., Conrad, C., Srinivasan, S., Loussouarn, D., & Duffy, M. J. (2014). ADAM8 expression in invasive breast cancer promotes tumor dissemination and metastasis. *EMBO molecular medicine*, *6*, 278-294.

[114]. Das, S. G., Pianetti, S., Sonenshein, G. E., & Mineva, N. D. (2017). Antibody targeting of ADAM8 for treatment of triple-negative breast cancer. *American association for cancer research*, 23-27.

[115]. Kelly, K., Hutchinson, G., Nebenius-Oosthuizen, D., Smith, A. J., Bartsch, J. W., Horiuchi, K., & Blobel, C. P. (2005). Metalloprotease-disintegrin ADAM8: expression

analysis and targeted deletion in mice. *Developmental dynamics: an official publication of the American Association of Anatomists*, *232*, 221-231.

[116]. Schlomann, U., Koller, G., Conrad, C., Ferdous, T., Golfi, P., Garcia, A. M., & Bossard, M. (2015). ADAM8 as a drug target in pancreatic cancer. *Nature communications*, *6*, 6175-6179.

[117]. Gómez-Gaviro, M., Domínguez-Luis, M., Canchado, J., Calafat, J., Janssen, H., Lara-Pezzi, E., & Sánchez-Madrid, F. (2007). Expression and regulation of the metalloproteinase ADAM-8 during human neutrophil pathophysiological activation and its catalytic activity on L-selectin shedding. *The journal of immunology*, *178*, 8053-8063.

[118]. Klopfer, K. J., & Vanderlick, T. K. (1996). Isotherms of dipalmitoylphosphatidylcholine (DPPC) monolayers: features revealed and features obscured. *Journal of colloid and interface science*, *182*, 220-229.

[119]. Zhai, J., Tran, N., Sarkar, S., Fong, C., Mulet, X., & Drummond, C. J. (2017). Self-assembled lyotropic liquid crystalline phase behavior of monoolein–capric acid–phospholipid nanoparticulate systems. *Langmuir*, *33*, 2571-2580.

[120]. Mabrey, S., & Sturtevant, J. M. (1976). Investigation of phase transitions of lipids and lipid mixtures by sensitivity differential scanning calorimetry. *Proceedings of the national academy of sciences*, *73*, 3862-3866.

[121]. Grüll, H., & Langereis, S. (2012). Hyperthermia-triggered drug delivery from temperature-sensitive liposomes using MRI-guided high intensity focused ultrasound. *Journal of controlled release*, *161*, 317-327.

[122]. Bastiat, G., & Lafleur, M. (2007). Phase behavior of palmitic acid/cholesterol/cholesterol sulfate mixtures and properties of the derived liposomes. *The journal of physical chemistry b*, *111*, 10929-10937.

[123]. Redondo-Morata, L., Giannotti, M. I., & Sanz, F. (2012). Influence of cholesterol on the phase transition of lipid bilayers: a temperature-controlled force spectroscopy study. *Langmuir*, *28*, 12851-12860.

[124]. Vance, J. E., & Tasseva, G. (2013). Formation and function of phosphatidylserine and phosphatidylethanolamine in mammalian cells. *Biochimica et biophysica acta-molecular and cell biology of lipids*, *1831*, 543-554.

[125]. Pétriat, F., Roux, E., Leroux, J. C., & Giasson, S. (2004). Study of molecular interactions between a phospholipidic layer and a pH-sensitive polymer using the langmuir balance technique. *Langmuir*, *20*, 1393-1400.

[126]. Skrabalak, S. E., Chen, J., Sun, Y., Lu, X., Au, L., Cobley, C. M., & Xia, Y. (2008). Gold nanocages: synthesis, properties, and applications. *Accounts of chemical research*, *41*, 1587-1595.

[127]. Sherry, A. D., Caravan, P., & Lenkinski, R. E. (2009). Primer on gadolinium chemistry. *Journal of magnetic resonance imaging: an official journal of the international society for magnetic resonance in medicine*, *30*, 1240-1248.

[128]. Caravan, P., Ellison, J. J., McMurry, T. J., & Lauffer, R. B. (1999). Gadolinium (III) chelates as MRI contrast agents: structure, dynamics, and applications. *Chemical reviews*, *99*, 2293-2352.

[129]. Zhang, H. (2017). Thin-film hydration followed by extrusion method for liposome preparation. In *Liposomes*. Humana Press, New York, NY, 17-22.

[130]. Nwe, K., Xu, H., Regino, C. A. S., Bernardo, M., Ileva, L., Riffle, L., & Brechbiel, M. W. (2009). A new approach in the preparation of dendrimer-based bifunctional diethylenetriaminepentaacetic acid MR contrast agent derivatives. *Bioconjugate chemistry*, *20*, 1412-1418.

[131]. Levacheva, I., Samsonova, O., Tazina, E., Beck-Broichsitter, M., Levachev, S., Strehlow, B., & Bakowsky, U. (2014). Optimized thermosensitive liposomes for selective doxorubicin delivery: formulation development, quality analysis and bioactivity proof. *Colloids and surfaces b: biointerfaces*, *121*, 248-256.

[132]. Fritze, A., Hens, F., Kimpfler, A., Schubert, R., & Peschka-Süss, R. (2006). Remote loading of doxorubicin into liposomes driven by a transmembrane phosphate gradient. *Biochimica et biophysica acta -biomembranes*, *1758*, 1633-1640.

[133]. Negussie, A. H., Yarmolenko, P. S., Partanen, A., Ranjan, A., Jacobs, G., Woods, D., & Dreher, M. R. (2011). Formulation and characterisation of magnetic resonance imageable thermally sensitive liposomes for use with magnetic resonance-guided high intensity focused ultrasound. *International journal of hyperthermia*, *27*, 140-155.

[134]. Hansen, C. B., Kao, G. Y., Moase, E. H., Zalipsky, S., & Allen, T. M. (1995). Attachment of antibodies to sterically stabilized liposomes: evaluation, comparison and optimization of coupling procedures. *Biochimica et biophysica acta -biomembranes*, *1239*, 133-144.

[135]. Brüßler, J., Marxer, E., Becker, A., Schubert, R., Schümmelfeder, J., Nimsky, C., & Bakowsky, U. (2014). Correlation of structure and echogenicity of nanoscaled ultrasound contrast agents in vitro. *Colloids and surfaces b: biointerfaces*, *117*, 206-215.

[136]. Plenagl, N., Duse, L., Seitz, B. S., Goergen, N., Pinnapireddy, S. R., Jedelska, J., & Bakowsky, U. (2019). Photodynamic therapy–hypericin tetraether liposome conjugates and their antitumor and antiangiogenic activity. *Drug delivery*, *26*, 23-33.

[137]. Engelhardt, K. H., Pinnapireddy, S. R., Baghdan, E., Jedelská, J., & Bakowsky, U. (2017). Transfection studies with colloidal systems containing highly purified bipolar tetraether lipids from sulfolobus acidocaldarius. *Archaea*, *2017*, 1-9.

[138]. Schmid, M., Wölk, C., Giselbrecht, J., Chan, K. A., & Harvey, R. D. (2018). A combined FTIR and DSC study on the bilayer-stabilising effect of electrostatic interactions in ion paired lipids. *Colloids and surfaces b: biointerfaces*, *169*, 298-304.

[139]. Conrad, C., Götte, M., Schlomann, U., Roessler, M., Pagenstecher, A., Anderson, P., & Kamm, R. D. (2018). ADAM8 expression in breast cancer derived brain metastases: Functional implications on MMP-9 expression and transendothelial migration in breast cancer cells. *International journal of cancer*, *142*, 779-791.

[140]. Ta, T., & Porter, T. M. (2013). Thermosensitive liposomes for localized delivery and triggered release of chemotherapy. *Journal of controlled release*, *169*, 112-125.

[141]. Mosmann, T. (1983). Rapid colorimetric assay for cellular growth and survival: application to proliferation and cytotoxicity assays. *Journal of immunological methods*, *65*, 55-63.

[142]. Tariq, I., Pinnapireddy, S. R., Duse, L., Ali, M. Y., Ali, S., Amin, M. U., & Bakowsky, U. (2019). Lipodendriplexes: A promising nanocarrier for enhanced gene delivery with minimal cytotoxicity. *European journal of pharmaceutics and biopharmaceutics*, *135*, 72-82.

[143]. Duse, L., Pinnapireddy, S. R., Strehlow, B., Jedelská, J., & Bakowsky, U. (2018). Low level LED photodynamic therapy using curcumin loaded tetraether liposomes. *European journal of pharmaceutics and biopharmaceutics*, *126*, 233-241.

[144]. Mahmoud, G., Jedelská, J., Strehlow, B., Omar, S., Schneider, M., & Bakowsky, U. (2017). Photo-responsive tetraether lipids based vesicles for prophyrin mediated vascular targeting and direct phototherapy. *Colloids and surfaces b: biointerfaces*, *159*, 720-728.

[145]. Lee, G. R., & Wintrobe, M. M. (1993). *Wintrobe's clinical hematology* (2). Lea & Febiger, 81-82.

[146]. Özcetin, A., Aigner, A., & Bakowsky, U. (2013). A chorioallantoic membrane model for the determination of anti-angiogenic effects of imatinib. *European journal of pharmaceutics and biopharmaceutics*, *85*, 711-715.

[147]. Goergen, N., Wojcik, M., Drescher, S., Pinnapireddy, S. R., Brüßler, J., Bakowsky, U., & Jedelská, J. (2019). The use of artificial gel forming bolalipids as novel formulations in antimicrobial and antifungal therapy. *Pharmaceutics*, *11*, 307-313.

[148]. Li, B., Tesar, D., Boswell, C. A., Cahaya, H. S., Wong, A., Zhang, J., & Kapadia, S. B. (2014). Framework selection can influence pharmacokinetics of a humanized therapeutic antibody through differences in molecule charge. In *MAbs 6*, 5, 1255-1264.

[149]. Ghaghada, K. B., Ravoori, M., Sabapathy, D., Bankson, J., Kundra, V., & Annapragada, A. (2009). New dual mode gadolinium nanoparticle contrast agent for magnetic resonance imaging. *PloS one*, *4*, 1-9.

[150]. Bartacek, J., Vergeldt, F. J., Maca, J., Gerkema, E., Van As, H., & Lens, P. N. (2016). Iron, cobalt, and gadolinium transport in methanogenic granules measured by 3D magnetic resonance imaging. *Frontiers in environmental science*, *4*, 1-9.

[151]. Shi, C., Cao, H., He, W., Gao, F., Liu, Y., & Yin, L. (2015). Novel drug delivery liposomes targeted with a fully human anti-VEGF165 monoclonal antibody show superior antitumor efficacy in vivo. *Biomedicine & pharmacotherapy*, *73*, 48-57.

[152]. Barenholz, Y. C. (2012). Doxil®—the first FDA-approved nano-drug: lessons learned. *Journal of controlled release*, *160*, 117-134.

[153]. Pitchaimani, A., Nguyen, T. D. T., Wang, H., Bossmann, S. H., & Aryal, S. (2016). Design and characterization of gadolinium infused theranostic liposomes. *RSC Advances*, *6*, 36898-36905.

[154]. Kumar, B. R., & Rao, T. S. (2012). AFM Studies on surface morphology, topography and texture of nanostructured zinc aluminum oxide thin films. *Digest journal of nanomaterials and biostructures*, *7*, 1881-1889.

[155]. Hardiansyah, A., Huang, L. Y., Yang, M. C., Liu, T. Y., Tsai, S. C., Yang, C. Y., & Lin, C. H. (2014). Magnetic liposomes for colorectal cancer cells therapy by high-frequency magnetic field treatment. *Nanoscale research letters*, *9*, 497-503.

[156]. Lee, A. G. (1977). Lipid phase transitions and phase diagrams I. Lipid phase transitions. *Biochimica et biophysica acta -reviews on biomembranes*, *472*, 237-281.

[157]. Gaber, M. H., Wu, N. Z., Hong, K., Huang, S. K., Dewhirst, M. W., & Papahadjopoulos, D. (1996). Thermosensitive liposomes: extravasation and release of contents in tumor microvascular networks. *International journal of radiation oncology biology physics*, *36*, 1177-1187.

[158]. Klemm P.J., Floyd W.C., Smiles D.E., Fréchet J.M.J., Raymond K.N. (2012), Improving T_1 and T_2 magnetic resonance imaging contrast agents through the conjugation of an esteramide dendrimer to high-water-coordination Gd(III) hydroxypyridinone complexes., *Contrast media molecular imaging*, 7, 95–9.

[159]. Fossheim, S. L., Il'yasov, K. A., Hennig, J., & Bjørnerud, A. (2000). Thermosensitive paramagnetic liposomes for temperature control during MR imaging-guided hyperthermia: *in vitro* feasibility studies. *Academic radiology*, *7*, 1107-1115.

[160]. Lorenzato, C., Cernicanu, A., Meyre, M. E., Germain, M., Pottier, A., Levy, L., & Smirnov, P. (2013). MRI contrast variation of thermosensitive magnetoliposomes triggered by focused ultrasound: a tool for image-guided local drug delivery. *Contrast media & molecular imaging*, *8*, 185-192.

[161]. Langereis, S., Geelen, T., Grüll, H., Strijkers, G. J., & Nicolay, K. (2013). Paramagnetic liposomes for molecular MRI and MRI-guided drug delivery. *NMR in biomedicine*, *26*, 728-744.

[162]. Pan, L., Liu, J., & Shi, J. (2018). Cancer cell nucleus-targeting nanocomposites for advanced tumor therapeutics. *Chemical society reviews*, *47*, 6930-6946.

[163]. Gellermann, J., Hildebrandt, B., Issels, R., Ganter, H., Wlodarczyk, W., Budach, V., & Wust, P. (2006). Noninvasive magnetic resonance thermography of soft tissue sarcomas during regional hyperthermia: correlation with response and direct thermometry. *Cancer*, *107*, 1373-1382.

[164]. Chen, L., Chen, C., Wang, P., & Song, T. (2017). Mechanisms of cellular effects directly induced by magnetic nanoparticles under magnetic fields. *Journal of nanomaterials*, *2017*, 1-13.

[165]. Venugopal, I., Pernal, S., Duproz, A., Bentley, J., Engelhard, H., & Linninger, A. (2016). Magnetic field-enhanced cellular uptake of doxorubicin loaded magnetic nanoparticles for tumor treatment. *Materials research express*, *3*, 1-5.

[166]. Liu, Q., Zhang, J., Xia, W., & Gu, H. (2012). Magnetic field enhanced cell uptake efficiency of magnetic silica mesoporous nanoparticles. *Nanoscale*, *4*, 3415-3421.

[167]. Laginha, K., Mumbengegwi, D., & Allen, T. (2005). Liposomes targeted via two different antibodies: assay, B-cell binding and cytotoxicity. *Biochimica et biophysica acta - biomembranes*, *1711*, 25-32.

[168]. De Menezes, D. E. L., Pilarski, L. M., & Allen, T. M. (1998). *In vitro* and *in vivo* targeting of immunoliposomal doxorubicin to human B-cell lymphoma. *Cancer research*, *58*, 3320-3330.

[169]. Ito, A., Kuga, Y., Honda, H., Kikkawa, H., Horiuchi, A., Watanabe, Y., & Kobayashi, T. (2004). Magnetite nanoparticle-loaded anti-HER2 immunoliposomes for combination of antibody therapy with hyperthermia. *Cancer letters*, *212*, 167-175.

[170]. Pradhan, P., Giri, J., Rieken, F., Koch, C., Mykhaylyk, O., Döblinger, M., & Plank, C. (2010). Targeted temperature sensitive magnetic liposomes for thermo-chemotherapy. *Journal of controlled release*, *142*, 108-121.

[171]. Farhane, Z., Bonnier, F., & Byrne, H. J. (2017). Monitoring doxorubicin cellular uptake and trafficking using in vitro Raman microspectroscopy: short and long time exposure effects on lung cancer cell lines. *Analytical and bioanalytical chemistry*, *409*, 1333-1346.

[172]. Plassat, V., Wilhelm, C., Marsaud, V., Ménager, C., Gazeau, F., Renoir, J. M., & Lesieur, S. (2011). Anti-estrogen-loaded superparamagnetic liposomes for intracellular magnetic targeting and treatment of breast cancer tumors. *Advanced functional materials*, *21*, 83-92.

[173]. Adamo, R. F., Fishbein, I., Zhang, K., Wen, J., Levy, R. J., Alferiev, I. S., & Chorny, M. (2016). Magnetically enhanced cell delivery for accelerating recovery of the endothelium in injured arteries. *Journal of controlled release*, *222*, 169-175.

[174]. Foldvari, M., Faulkner, G. T., Mezei, C., & Mezei, M. (1992). Interaction of liposomal drug delivery systems with cells and tissues: microscopic studies. *Cells and materials*, *2*, 1-8.

[175]. Zhao, J., & Stenzel, M. H. (2018). Entry of nanoparticles into cells: The importance of nanoparticle properties. *Polymer chemistry*, *9*, 259-272.

[176]. Palade, G. E. (1953). An electron microscope study of the mitochondrial structure. *Journal of histochemistry & cytochemistry*, *1*, 188-211.

[177]. Foroozandeh, P., & Aziz, A. A. (2018). Insight into cellular uptake and intracellular trafficking of nanoparticles. *Nanoscale research letters*, *13*, 339-347.

[178]. Rejman, J., Oberle, V., Zuhorn, I. S., & Hoekstra, D. (2004). Size-dependent internalization of particles via the pathways of clathrin-and caveolae-mediated endocytosis. *Biochemical journal*, *377*, 159-169.

[179]. Matthay, K. K., Abai, A. M., Cobb, S., Hong, K., Papahadjopoulos, D., & Straubinger, R. M. (1989). Role of ligand in antibody-directed endocytosis of liposomes by human T-leukemia cells. *Cancer research*, *49*, 4879-4886.

[180]. Guo, N., Gao, C., Liu, J., Li, J., Liu, N., Hao, Y., & Zhang, X. (2018). Reversal of ovarian cancer multidrug resistance by a combination of LAH4-L1-siMDR1 nanocomplexes with chemotherapeutics. *Molecular pharmaceutics*, *15*, 1853-1861.

[181]. Mortensen, J. H., Jeppesen, M., Pilgaard, L., Agger, R., Duroux, M., Zachar, V., & Moos, T. (2013). Targeted antiepidermal growth factor receptor (cetuximab) immunoliposomes enhance cellular uptake in vitro and exhibit increased accumulation in an intracranial model of glioblastoma multiforme. *Journal of drug delivery*, *2013*, 1-12.

[182]. Guo, P., Yang, J., Liu, D., Huang, L., Fell, G., Huang, J., & Auguste, D. T. (2019). Dual complementary liposomes inhibit triple-negative breast tumor progression and metastasis. *Science advances*, *5*, eaav5010.

[183]. Kuznetsova, N. R., Sevrin, C., Lespineux, D., Bovin, N. V., Vodovozova, E. L., Mészáros, T., & Grandfils, C. (2012). Hemocompatibility of liposomes loaded with lipophilic prodrugs of methotrexate and melphalan in the lipid bilayer. *Journal of controlled release*, *160*, 394-400.

[184]. Dobrovolskaia, M. A., & McNeil, S. E. (2007). Immunological properties of engineered nanomaterials. *Nature nanotechnology*, *2*, 469-478.

[185]. Deibler, G. E., Holmes, M. S., Campbell, P. L., & Gans, J. (1959). Use of triton X-100 as a hemolytic agent in the spectrophotometric measurement of blood O_2 saturation. *Journal of applied physiology*, *14*, 133-136.

[186]. Vargas, A., Zeisser-Labouèbe, M., Lange, N., Gurny, R., & Delie, F. (2007). The chick embryo and its chorioallantoic membrane (CAM) for the *in vivo* evaluation of drug delivery systems. *Advanced drug delivery reviews*, *59*, 1162-1176.

[187]. Herrmann, A., Taylor, A., Murray, P., Poptani, H., & Sée, V. (2018). Magnetic resonance imaging for characterization of a chick embryo model of cancer cell metastases. *Molecular imaging*, *17*, 1536012118809585.

5.2. Presentations:

[1]. Development and characterization of magnetic thermosensitive liposomes; **Alawak M**, Levacheva I, Brüßler J, Bakowsky U. [Poster Presentation]. CRS Local Chapter; March, 2016; Saarland, Germany.

[2]. Optimized magnetic thermosensitive liposomes for cancer therapy; **M. Alawak**, I. Levacheva, J. Brüßler, C. Wölk, U. Bakowsky. [Poster Presentation]. CRS Local Chapter March 2017; Marburg, Germany.

[3]. Magnetic thermosensitive immunoliposomes loaded with Doxorubicin. **M. Alawak**, K. Engelhardt, G. Mahmoud, J. Brüßler, C. Wölk, J.W. Bartsch, U. Bakowsky. [Poster Presentation]. CRS Local Chapter; March 2018; Halle, Germany.

[4]. Magnetic thermosensitive liposomes loaded with Doxorubicin for selective cancer therapy. **M. Alawak**, K. Engelhardt, G. Mahmoud, J. Brüßler, I. Levacheva, J. Schäfer, C. Wölk, J. W. Bartsch, U. Bakowsky. [Poster Presentation]. 11th World Conference on Pharmaceutics, Biopharmaceutics and Pharmaceutical Technology, March 2018 Granada, Spain.

[5]. Targeting of breast cancer cells using magnetic low thermosensitive immunoliposomes **M. Alawak**, K. Engelhardt, G. Mahmoud, J. Brüßler, I. levacheva, L. Duse, S.R. Pinnapireddy, C. Wölk, J.W. Bartsch, U. Bakowsky. [Poster Presentation]. CRS Local Chapter, March, 2019; Leipzig , Germany. 7-8 March, 2019

5.3. Research Output

[1]. Fahmy, S. A., **Alawak, M**., Brüßler, J., Bakowsky, U., & El Sayed, M. M. (2019). Nanoenabled Bioseparations: Current Developments and Future Prospects. *BioMed research international, 2019.*

[2]. Fahmy, S. A., Brüßler, J., **Alawak, M**., El-Sayed, M. M., Bakowsky, U., & Shoeib, T. (2019). Chemotherapy Based on Supramolecular Chemistry: A Promising Strategy in Cancer Therapy. *Pharmaceutics*, *11*(6), 292.

[3]. **Alawak, M**., Mahmoud, G., Abu Dayyih, A., Duse, L., Pinnapireddy, S. R., Engelhardt, K., Awak, I., Wölk, C., König, A.M., Brüßler, J., Bakowsky, U. Magnetic Resonance Activatable Thermosensitive Liposomes for Controlled Doxorubicin Delivery. *Manuscript in Preparation.*

[4]. **Alawak, M.,** Mahmoud, G., Abu Dayyih, Tariq, I., Duse, L., Goergen, N., Engelhardt, K., Pinnapireddy, S. R ., Jedelska. J., Awak, M., König, A.M, Brüßler, J., Bartsch, J, W, Bakowsky, U. ADAM8 AS A N ovel Target For Doxorubicin Delivery To TNBC Cells Using Magnetic Thermosensitive Liposomes. *Manuscript in Preparation*

5.4. Curriculum Vitae

PERSONAL DETAILS

Name	Mohamad Alawak
Date-, Place of Birth	01.01.1988 in Deirazzor, Syria
Nationality	German
Marital status	Single

WORK EXPERIENCE

08/2015 - Persent

Scientific Assistance (PhD candidate)
Philipps-Universität Marburg, Germany
Institut of Pharmaceutics and Biopharmaceutics
Thesis Titled: **"**Immuno Magnetic Thermosensitive Liposomes For Cancer Therapy"

- Pharmaceutical Technology/Nanotechnology
- Cell Culture
- Lab Assistant for Student´s Practical

04/2016 - Present

Pharmacist (Part-time), Brunnen Pharmacy, „Apotheke im Hauptbahnhof"Pharmacy, Marburg, Frankfurt am Main, Germany

- Dispensing Medications and Patients Counseling
- Training the Employees and Monitoring Pharmaceutical Practice
- Emergency Service

03/2015-05/2015

Pharmacist (Fulltime), Spitzweg Pharmacy, Königslutter, Germany

- Dispensing Medications and Patients Counseling
- Offering Advice for Physicians
- Training and Supervising the Trainees and Interns

05/2014 - 10/2015

Pharmacist Internship, Lehndorf Pharmacy, Braunschweig, Germany

- Dispensing Medications and Patients Counseling
- Production and Formulation for the Prescriptions

11/2013 – 04/2014

Pharmacy Internship, K10 Pharmacy, Brunswick, Germany

▪ Dispensing Medications and Patients Counseling
▪ Production and Formulation for the Prescriptions
Pharmacy Intern, Faten Ghareeb Pharmacy, Syria

02/2008 - 09/2010 Firma Amrit Pharmaceuticals, Syria (2 Months per Year)
Departments (Tablets, Ampoules, Syrups, Capsules, Suppositories, Quality Control)

07/2007 - 08/2012 Faten Gharib Pharmacy, Pharmacy Intern (2 Months per Year)

EDUCATION

02/2015 Registered Pharmacist in Germany, Hannover, Germany

02/2013 Diploma in Pharmacy and Pharmaceutical Chemistry (Aleppo University, Syria), Registered Pharmacist (Syria)

06/2006 University Qualification Exam (Almotafawikin, Deirazzor, Syria)

PERSONAL SKILLS AND INTEREST

Languages German (Excellent Work Proficiency), English (Very Good Work Proficiency), Arabic (Mother tongue)

IT Skills Computer-Skills, Microsoft Office

Research Literature Research, Analysis, and Evaluation of Scientific Results, Quality Control, Aim Orientation, Scientific Publications and Conferences.